PHOTOCATALYZED DESTRUCTION OF CHLORINATED HYDROCARBONS

Thesis by

Scot Turnbull Martin

In Partial Fulfillment of the Requirements

for the Degree of

Doctor of Philosophy

California Institute of Technology

Pasadena, California

1996

(Submitted October 6, 1995)

Acknowledgment

I express my heartfelt thanks to the Caltech community that I have been a part of during the last four years.

My mentor, Michael Hoffmann, played the most crucial role. He provided unwavering support, encouragement, patience, and guidance.

Support from the groups of Geoff Blake, Mark Davis, Nate Lewis, James Morgan, and Dan Weitekamp is gratefully acknowledged.

Beth Carraway, Peter Green, Inez Hua, Amy Hoffman, Albert Lee, Patrick Lang, Tom Lloyd, Colin Morrison, David Park, Simo Pehkonen, Ron Siefert, Andreas Termin, Linda Weavers, Dean Willberg, and Tim Wu taught me numerous experimental techniques and proferred innumerable excellent scientific insights. I give special thanks to Wonyong Choi for years of cooperative efforts at unravelling the subtleties of photocatalysis, to Janet Kesselman for improving my arguments by incessant skepticism, and to Nicole Peill for friendship transcending our time at Caltech. Finally, Hartmut Herrmann has a unique place in helping me to mature as a scientist.

Without the following people who truly know their stuff, no one would ever finish a thesis: Rich Eastvedt, Joe Fontana, Carol Garland, Rayma Harrison, Susan Leising, Linda Scott, and Hai Vu.

I acknowledge the support of my close friends, including Tim Francis, Lyatt Jaegle, Michael MacDougal, Frank Pompillio, and Alex Sun. And my cat, Isabella, is a constant companion.

My parents have provided unconditional love and support from as far away as Indiana. I am indebted to their years of attention, effort, and sacrifice on my behalf.

One friend I did not mention above. I am taking the mantles of "doctor" and "husband" nearly coincidentally. To demonstrate her patience, empathy, and self-sacrifice, let us simply say that she has agreed to marry a man who aspires to be an assistant professor. For offering always encouragement, love, and faith, Rene Knowles is my deepest source of inspiration and motivation.

Abstract

Semiconductor photocatalysis with a primary focus on TiO_2 as a durable photocatalyst has been applied as a method for water and air purification. In this thesis, the basic electronic and chemical processes underlying the quantum efficiencies of the TiO_2/UV process are investigated.

Time-resolved microwave conductivity experiments provide the recombination lifetimes and interfacial charge transfer rate constants of eight different TiO_2 catalysts. Their quantum efficiencies towards the photooxidation of chlorinated hydrocarbons vary from 0.04 to 0.44%. A direct correlation between (1) the quantum efficiencies and (2) the recombination lifetimes and the interfacial charge transfer rate constants is observed.

The charge-carrier recombination rate in size-quantized particles (1-4 nm) is increased due to the mixing of states that relaxes the selections rules of an indirect bandgap semiconductor.

The effects of protonation (i.e., pH 7-12) of amphoteric ZnO surface states on cross-sections for electron capture at the surface are studied by time-resolved radio frequency conductivity. Electrostatic repulsion due to a negatively-charged ZnO-surface leads to decreasing surface recombination rates with increasing pH.

Vanadium doped into TiO_2 affects the quantum efficiency. Depending on the preparation method, vanadium plays three distinct roles. First, vanadium is present as surficial $>VO_2^+$ and promotes charge-carrier recombination through electron-trapping followed by hole elimination. Second, V(IV) impurities in surficial V_2O_5 islands result in enhanced charge-carrier recombination through hole-trapping followed by electron elimination. Third, V(IV) is substitutional in the TiO_2 lattice in the form of a solid solution, $V_xTi_{1-x}O_2$. The V(IV) centers trap both electrons and holes and thus yield enhanced charge-carrier recombination.

The addition of inorganic oxidants such as HSO_5^-, ClO_3^-, IO_4^-, and BrO_3^- increases the quantum efficiency. BrO_3^- acts by scavenging conduction-band electrons and reducing charge-carrier recombination. When ClO_3^- is present, however, competitive adsorption for the TiO_2 surface occurs among 4-CP, ClO_3^-, and O_2, and the heterogeneous photodegradation of 4-chlorophenol follows three parallel pathways. ClO_3^- favors a reaction pathway involving the thermal oxidation of the reactive intermediates.

Table of Contents

Acknowledgment iii

Abstract v

List of Tables ix

List of Figures xii

Chapter 1 Introduction and Overview A-1

Chapter 2 Time-Resolved Microwave Conductivity (TRMC): TiO_2 Photoreactivity and Size-Quantizaton B-1

Chapter 3 Time-Resolved Microwave Conductivity (TRMC): Quantum-Sized TiO_2 and the Effect of Adsorbates and Light Intensity on Charge-Carrier Dynamics C-1

Chapter 4 Time-Resolved Radio-Frequency Conductivity (TRRFC) Studies of Charge-Carrier Dynamics in Aqueous Semiconductor Suspensions D-1

Chapter 5 Photochemical Mechanism of Size-Quantized Vanadium-Doped TiO_2 Particles E-1

Chapter 6 Chemical Mechanism of Inorganic Oxidants in the TiO_2/UV Process: Increased Rates of Degradation of Chlorinated Hydrocarbons F-1

Chapter 7 Conclusions G-1

List of Tables

Chapter 2

Table 1 TRMC results and photoreactivity data of commercial samples of TiO_2. B-26

Table 2 Quantum efficiencies of Q-TiO_2 and P25-A towards photomineralization of chlorinated compounds. B-27

Table 3 TRMC results for Q-TiO_2, Fe(III)-doped Q-TiO_2, P25-A (No NO_3^-), and P25-A (NO_3^-). B-28

Chapter 3

Table 1 Relative initial carrier concentrations and conductivity decay half-lives C-25

Table 2 Injection level cross-over thresholds and response factors C-26

Chapter 5

Table 1 Quantum efficiencies for the degradation of 4-chlorophenol. (Irradiation conditions reported in Figure 1.) E-32

Table 2 Intermediates formed during the photo-degradation of 4-chlorophenol in the presence of TiO_2. (HQ = hydroquinone, BQ = 1,4-benzoquinone, and CC = 4-chlorocatechol.) E-33

Table 3: Physical characterization of TiO_2 particles. E-34

Table 4 Vanadium speciation in doped TiO_2. E-35

Table 5 g-Factors and hyperfine splitting constants (G) derived for vanadium-doped TiO_2 spectra (cf. Figure 6). E-36

Table 6 g-Factors and hyperfine splitting constants (G) reported for various paramagnetic species. E-37

Chapter 6

Table 1 Apparent quantum efficiencies ($\Phi \times 10^2$) for the photooxidation of 4-CP by the TiO_2/UV process in the presence of several oxidants (0.1 M $NaClO_3$, 0.1 M $KBrO_3$, 18 mM KIO_4, 0.1 M $NaClO_2$, and 1 atm O_2). Conditions: I = 2.1 mEin min^{-1}, $\lambda > 340$ nm, deoxygenated, $[TiO_2]$ = 1 g/L, pH unadjusted, T = 25 °C, $[4\text{-CP}]_0$ = 100 μM. F-26

Table 2 Chemical reactions and kinetic equations of the proposed mechanism for the TiO_2/UV photooxidation of 4-CP in the presence of O_2 and ClO_3^-. F-27

List of Figures

Chapter 1

Figure 1 Primary steps in the photoelectrochemical mechanism. (1) Formation of charge-carriers by a photon. (2) Charge-carrier recombination to liberate heat. (3) Initiation of an oxidative pathway by a valence-band hole. (4) Initiation of a reductive pathway by a conduction-band electron. (5) Further thermal (e.g., hydrolysis or reaction with active oxygen species) and photocatalytic reactions to yield mineralization products. (6) Trapping of a conduction-band electron in a dangling surficial bond to yield Ti(III). (7) Trapping of a valence-band hole at a surficial titanol group. A-13

Chapter 2

Figure 1 Transmission electron micrograph of quantum-sized TiO_2. B-29

Figure 2 Schematic diagram of the apparatus for TRMC measurements. B-30

Figure 3 Sample holder for powdered semiconductor. B-31

Figure 4 Degradation rate of chloroform as a function of concentration. ▲ P25-A. ■ Q-TiO_2. ● Fe(III) doped (1%) Q-TiO_2. Conditions: pH = 2.8 (HNO_3), [TiO_2] = 0.5 g/L, I = 110 μM min^{-1} ($\lambda = 320 \pm 5$ nm), air equilibrated. B-32

Figure 5 Double log plot of time-resolved microwave conductivity decay of several powdered semiconductors supported in transdecalin. ▲ ZnO. ◆ CdS. ■ P25-A. ● Al_2O_3. B-33

Figure 6 Degradation rate of chloroform as a function of light intensity. Conditions: pH = 11 (NaOH), 0.5 g/L P25-A, $320 < \lambda < 380$ nm, air equilibrated. B-34

Figure 7 Effect of the incident laser pulse energy on the initial (● 100 ns) conductivity of P25-A prepared in HNO_3 and transdecalin. B-35

Figure 8 Representative conductivity decays of Sachtleben and Degussa TiO_2 powders. (a) P13, P25-B, P18, and P17, 2 μs/div. (b) Exponential fit of conductivity decay for P13, k = 0.056 ms^{-1}, 10 ms/div. B-36

Figure 9 (a) Contour plot of quantum efficiency as a function of recombination lifetime (cf. explanation in main text) and interfacial electron-transfer rate constant. (b) Linear transformation of contour plot. B-37

Figure 10 Conductivity decays of P25-A (F), Q-TiO_2 (H), and Fe(III)-doped Q-TiO_2 (B). Samples prepared by rotary evaporation from HNO_3 (pH 1.5) and supported in transdecalin except for P25-A-No NO_3^- (J), which was prepared without HNO_3. (a) 200 ns/div timebase. (b) 10 ms/div timebase. B-38

Chapter 3

Figure 1 EPR spectra obtained at 77 K for sol-gel preparations of size-quantized TiO_2 in (1) HNO_3, (2) HCl, and (3) $HClO_4$. C-27

Figure 2 Effect of HNO_3, $HClO_4$, and HCl on the conductivity decays of Degussa P25 supported in transdecalin. (a) 200 ns/div timebase. (b) 2 μs/div timebase. (c) 200 μs/div timebase. (d) 10 ms/div timebase. C-28

Figure 3 Effect of HNO_3, $HClO_4$, and HCl on the conductivity decays of Q-TiO_2 supported in transdecalin. (a) 200 ns/div timebase. (b) 2 μs/div timebase. (c) 200 μs/div timebase. (d) 10 ms/div timebase. C-29

Figure 4 Effect of transdecalin, isopropanol, tetranitromethane, and methyl viologen on the conductivity decays of Degussa P25. (a) 200 ns/div timebase. (b) 2 μs/div timebase. (c) 200 μs/div timebase. (d) 10 ms/div timebase. C-30

Figure 5 Effect of transdecalin, isopropanol, and methyl viologen (supported in transdecalin) on the conductivity decays of Q-TiO_2 prepared in HNO_3. (a) 200 ns/div timebase. (b) 2 μs/div timebase. (c) 200 μs/div timebase. (d) 10 ms/div timebase. C-31

Figure 6 Effect of the incident laser pulse energy (100% = 4.9 mJ/pulse) on the conductivity decays of Degussa P25 supported in transdecalin on the 2 μs/div timebase. C-32

Figure 7 Effect of the incident laser pulse energy on the initial (● 100 ns) and the residual (■ 15 μs) conductivity of Degussa P25 prepared in $NaClO_4$ and transdecalin. C-33

Figure 8 Effect of the incident laser pulse energy on the initial (● 100 ns) and the residual (■ 15 μs) conductivity of Q-TiO_2 prepared in $NaClO_4$ and transdecalin. C-34

Figure 9 Effect of the incident laser pulse energy on the initial (● 100 ns) and the residual (■ 15 μs) conductivity of Degussa P25 prepared in HNO_3 and transdecalin. C-35

Chapter 4

Figure 1 Schematic representation of time-resolved radio-frequency conductivity (TRRFC) apparatus. D-19

Figure 2 a, top: Q-well calculated from eq 1 for the circuit shown in the inset. $R_1 = R_2 = 2\ \Omega$, $L = 240$ nH, $C = 4.125$ pF. b, bottom: Change of Q-well due to variation of L and the resulting time depending TRRFC signal (inset). D-20

Figure 3 Time-resolution and sensitivity of the TRRFC experiment (1 g/L ZnO aqueous suspensions) for pH = 7.0, 9.5, and 12.0. 200 ns/div timebase. Overlay of original traces. D-21

Figure 4 Effect of pH on charge carrier recombination dynamics in 1 g/L ZnO aqueous suspensions. (a, top) 2 µs/div timebase. (b, middle) 200 µs/div timebase. (c, bottom) 10 ms/div timebase, normalized traces (see text). D-22

Figure 5 TRRFC signal from 1 g/l ZnO in isopropanol in comparison to the aqueous suspension at unadjusted pH, i.e., pH = 8.5. D-23

Chapter 5

Figure 1 (a) Disappearance of 4-chlorophenol (E) and the appearance of hydroquinone (G) and benzoquinone (A) as a function of irradiation time in the presence of undoped TiO_2 calcined at 400 °C. (b) No light. (c) No TiO_2. ($I = 200\ \mu M\ min^{-1}$, pH = 3.9, O_2 saturated, $[TiO_2] = 1.0$ g/L, $\lambda = 324 \pm 5$ nm.) E-38

Figure 2 Transmission electron micrographs of vanadium-doped TiO$_2$ calcined at 25 °C (a, b) and 800 °C (c). E-39

Figure 3 Electron diffraction patterns of vanadium-doped TiO$_2$ calcined at 25 °C. E-42

Figure 4 UV/Vis reflection spectra of undoped TiO$_2$ calcined at 25 °C (E), 200 °C (G), 400 °C (A), 600 °C (Ü), and 800 °C (Ç). E-43

Figure 5 UV/Vis reflection spectra of vanadium-doped TiO$_2$ calcined at 25 °C (E), 200 °C (G), 400 °C (A), 600 °C (Ü), and 800 °C (Ç). E-44

Figure 6 EPR spectra recorded at 77 K of vanadium-doped TiO$_2$. (a) g-Factor and hyperfine splitting constant assignments for sample heat-treated at 800 °C. (b) Effect of calcination temperature at 25 °C (E), 200 °C (G), 400 °C (A), 600 °C (Ü), and 800 °C (Ç). The signal intensities are shown as $I = (\text{gain})^{-1} \times 10^4$. E-45

Figure 7 EPR difference spectra due to CW irradiation of vanadium-doped TiO$_2$ calcined at 25 °C (E), 400 °C (A), and 800 °C (Ç) (77 K, 450 W Hg lamp, $310 < \lambda < 380$ nm using 7-60-1 Kopp bandpass filter). E-47

Figure 8 Time-resolved microwave conductivity of vanadium-doped

TiO_2 calcined at 25 °C (E), 400 °C (A), and 800 °C (Ç). E-48

Figure 9 Charge-carrier dynamics of vanadium-doped TiO_2. E-49

Chapter 6

Figure 1 (a) Initial quantum efficiencies for the photooxidation of 4-CP in deoxygenated (E) and oxygenated (G) TiO_2 slurries as a function of Log[ClO_3^-]. (b) Initial quantum efficiencies for the photooxidation of 4-CP (A) as a function of Log[BrO_3^-]. O_2 has no apparent effect. Conditions: See Table 1. F-29

Figure 2 Quantum efficiency for the disappearance of 4-CP in a slurry of $NaClO_3$, O_2, and TiO_2 as a function of incident light intensity. Conditions: See Table 1. F-30

Figure 3 Formation of I_3^- in suspensions of 1 mM I^-, 0.1 M ClO_3^-, O_2, and TiO_2 irradiated with ultraviolet light. Initial (i) and steady-state (ss) quantum-efficiencies are shown in the legend. Conditions: See Table 1. F-31

Figure 4 Reaction mechanism. F-32

Chapter 7

Figure 1 Kinetics of the primary steps in photoelectrochemical mechanism. Recombination is mediated primarily by >Ti(III) in the first 10 ns. Valence-band holes are sequestered as long-lived >TiOH$^{\bullet+}$ after 10 ns. >TiOH is reformed by recombination with conduction-band electrons or oxidation of the substrate on the time-scale of 100 ns. The arrow lengths are representative of the respective time scales. G-6

Figure 2 Secondary reactions with activated oxygen species in the photoelectrochemical mechanism. G-7

Chapter 1

Introduction and Overview

[The text of this chapter appeared as a part of Hoffmann, M.R., Martin, S.T., Choi, W., and Bahnemann, D.W., *Chemical Reviews*, **1995**, *95*, 69.]

General Background

The civilian, commercial and defense sectors of most advanced industrialized nations are faced with a tremendous set of environmental problems related to the remediation of hazardous wastes, contaminated groundwaters and the control of toxic air contaminants. For example, the slow pace of hazardous waste remediation at military installations around the world is causing a serious delay in conversion of many of these facilities to civilian uses. Over the last ten years problems related to hazardous waste remediation[1] have emerged as a high national and international priority .

Problems with hazardous wastes at military installations are related in part to the disposal of chemical wastes in lagoons, underground storage tanks and dump sites. As a consequence of these disposal practices, the surrounding soil and underlying groundwater aquifers have become contaminated with a variety of hazardous (i.e., toxic) chemicals. Typical wastes of concern include heavy metals, aviation fuel, military-vehicle fuel, solvents and degreasing agents and chemical byproducts from weapons manufacturing. The projected costs for cleanup at more than 1800 military installations in the U.S. have been put at $30 billion; the time required for cleanup has been estimated to be more than 10 years.

In the civilian sector, the elimination of toxic and hazardous chemical substances such as the halogenated hydrocarbons from waste effluents and previously contaminated sites has become a major concern. More than 540 million metric tons of hazardous solid and liquid waste are generated annually by more than 14,000 installations in the U. S. A significant fraction of these wastes are disposed on the land each year. Some of these wastes eventually contaminate ground and surface waters.

Groundwater contamination is likely to be the primary source of human contact with toxic chemicals emanating from more than 70% of the hazardous waste sites in the U.S. General classes of compounds of concern include: solvents, volatile organics, chlorinated volatile organics, dioxins, dibenzofurans, pesticides, PCB's, chlorophenols, asbestos, heavy metals and arsenic compounds. Some specific compounds of interest are: 4-chlorophenol, pentachlorophenol, trichloroethylene (TCE), polychloroethylene (PCE), CCl_4, $HCCl_3$, CH_2Cl_2, ethylenedibromide, vinyl chloride, ethylene dichloride, methyl chloroform, p-chlorobenzene, and hexachlorocyclopentadiene. The occurrence of TCE, PCE, CFC-113 (i.e., Freon-113) and other grease-cutting agents in soils and groundwaters is widespread.

In order to address this signicant problem, extensive research is underway to develop advanced analytical, biochemical and physicochemical methods for the characterization and elimination of hazardous chemical compounds from air, soil and water. Advanced physicochemical processes such as semiconductor photocatalysis are intended to be both supplementary and complementary to some of the more conventional approaches to the destruction or transformation of hazardous chemical wastes such as high-temperature incineration, amended activated sludge digestion, anaerobic digestion and conventional physicochemical treatment.[1-5]

Semiconductor Photocatalysis

Over the last ten years the scientific and engineering interest in the application of semiconductor photocatalysis has grown exponentially. In the areas of water, air and wastewater treatment alone, the rate of publication exceeds 200 papers per year averaged over the last ten years.[6] Given the tremendous level of interest in semiconductor photochemistry and photophysics over the last 15 years, a number of review articles have appeared. For additional background information and reviews of the relevant literature, we refer the reader to recent reviews provided by Ollis and El-Akabi,[6] Blake,[7] Mills et al.,[8] Kamat,[9] Fox and Dulay,[10] Bahnemann,[11] Pichat,[12] Aithal,[13] Lewis,[14] and Bahnemann et al..[15] Earlier overviews are available in the works of Fox,[16] Ollis et al.,[17] Pelizzetti and Serpone,[18] Grätzel,[19] Matthews,[20] Schiavello,[21-22] Serpone,[23] Serpone and Pelizzetti,[24] Anpo,[25] Bahnemann et al.,[26] and Henglein.[27]

Semiconductor photocatalysis with a primary focus on TiO_2 as a durable photocatalyst has been applied to a variety of problems of environmental interest in addition to water and air purification. It has been shown to be useful for the destruction of microganisms such as bacteria[28] and viruses,[29] for the inactivation of cancer cells,[30-31] for odor control,[32] for the photosplitting of water to produce hydrogen gas,[33-38] for the fixation of nitrogen,[39-42] and for the clean-up of oil spills.[43-45]

Semiconductors (e.g., TiO_2, ZnO, Fe_2O_3, CdS and ZnS) can act as sensitizers for light-induced redox processes due to their electronic structure, that is characterized by a filled valence band and an empty conduction band.[46] When a photon with an energy of hν matches or exceeds the bandgap-energy, E_g, of the semiconductor, an electron, e_{cb}^-, is promoted from the valence band, VB, into the conduction band, CB, leaving a hole, h_{vb}^+, behind (see Figure 1). Excited-state conduction-band electrons and valence-band holes can recombine and dissipate the input energy as heat, get trapped in metastable surface states, or react with electron donors and electron acceptors adsorbed on the semiconductor surface or within the surrounding electrical double layer of the charged particles.

In the absence of suitable electron and hole scavengers, the stored energy is dissipated within a few nanoseconds by recombination.[47] If a suitable scavenger or surface defect state is available to trap the electron or hole, recombination is prevented and subsequent redox reactions may occur. The valence band holes are powerful oxidants (+1.0 to +3.5 V vs NHE depending on the semiconductor and pH), while the conduction band electrons are good reductants (+0.5 to -1.5 V vs NHE).[19] Most organic photodegradation reactions utilize the oxidizing power of the holes either directly or indirectly; however, to prevent a buildup of charge one must also provide a reducible species to react with the electrons. In contrast, on bulk semiconductor electrodes only one species, either the hole or electron, is available for reaction due to band bending.[48] However, in very small semiconductor particle suspensions both species are present on the surface. Therefore, careful consideration of both the oxidative and the reductive paths is required.

The application of illuminated semiconductors for the remediation of contaminants has been used successfully for a wide variety of compounds[49-56] such as alkanes, aliphatic alcohols, aliphatic carboxylic acids, alkenes, phenols, aromatic carboxylic acids, dyes, PCB's, simple aromatics, halogenated alkanes and alkenes, surfactants, and pesticides as well as for the reductive deposition of heavy metals (e.g., Pt^{4+}, Au^{4+}, Rh^{3+}, Cr(VI)) from aqueous solution to surfaces.[17,57-59] In many cases, complete mineralization of organic compounds has been reported.

A general stoichiometry for the heterogeneously-photocatalyzed oxidation of a generic chlorinated hydrocarbon to complete mineralization can be written as follows:

$$C_xH_yCl_z + \left(x + \frac{y-z}{4}\right)O_2 \xrightarrow{hv,\ TiO_2} x\,CO_2 + z\,H^+ + z\,Cl^- + \left(\frac{y-z}{2}\right)H_2O \quad (1)$$

Semiconductor photocatalysis appears to be a promising technology that has a number of applications in environmental systems such as air purification, water disinfection, hazardous waste remediation and water purification. In addition, the basic research that underlies the application of this technology is forging a new understanding of the complex heterogeneous photochemistry of metal oxide systems in multiphasic environments.

Thesis work

The basic electronic and chemical processes underlying the quantum efficiencies of the TiO_2/UV process are investigated in this thesis. In pilot-scale studies of the

TiO_2/UV process, the catalyst chosen universally has been Degussa P25. This catalyst is inexpensive and highly active relative to other commonly available TiO_2 catalysts. P25 was formulated for the paint industry, and its high photoreactivity has been unwelcome in that context due to the photooxidation and subsequent discoloration of the chemical binding agents in the paint. In fact, efforts have been made to reduce the photoreactivity of P25. It is thus reasonable to believe that a full understanding of the TiO_2 catalyst should yield a substantial improvement in photoreactivity. To that end, the following chapters detail what has been learned about the TiO_2/UV process through this thesis work.

The second and third chapters describe TRMC measurements of the recombination lifetimes and interfacial charge transfer rate constants of eight TiO_2 catalysts prepared by different methods. The quantum efficiencies towards the photooxidation of chlorinated hydrocarbons vary from 0.04 to 0.44% for these TiO_2 catalysts. A direct correlation between (1) the quantum efficiencies and (2) the recombination lifetimes and the interfacial charge transfer rate constants is observed. In addition, ultrasmall TiO_2 particles (1-4 nm radius) are synthesized. The charge-carrier recombination rate in size-quantized TiO_2 is increased due to the mixing of states that relaxes the selection rules of an indirect bandgap semiconductor.

In the fourth chapter, a radio frequency conductivity experiment (TRRFC) is described that allows for the time-dependent study of the charge-carrier dynamics in semiconductor particles suspended in opaque aqueous slurries. Previously, charge-carrier dynamics have been studied for transparent colloidal TiO_2 (optical methods) or nonaqueous pastes (TRMC). In those measurements, the system studied has not been identical to the conditions of the TiO_2/UV process (e.g., opaque aqueous dispersions). It has thus been questionable to apply the results obtained for charge-carrier dynamics to our understanding of TiO_2/UV photoreactivity. The results reported in chapters two and three demonstrate that, in fact, colloidal TiO_2 and Degussa P25 have different charge-carriers dynamics and TiO_2/UV quantum efficiencies. The TRRFC measurements thus provide an improved experimental approach because the charge-carrier dynamics are studied under experimental conditions that are identical to typical steady-state photolysis TiO_2/UV conditions. The fourth chapter details a TRRFC study on the effect of protonation (i.e., changes in pH) of amphoteric ZnO surface states on charge-carrier dynamics. The cross-sections for carrier capture at the surface are successfully interpreted based upon an electrostatic model.

The fifth chapter addresses the photoelectrochemical mechanism by which transition metal ions doped into TiO_2 affect the quantum efficiency of the TiO_2/UV process. A single dopant (vanadium) is selected for a detailed investigation. Depending on the preparation method of the vanadium-doped TiO_2, three distinct roles are found for vanadium. In the first case, vanadium is present as surficial $>VO_2^+$ and promotes charge-carrier recombination through electron-trapping followed by hole elimination. In the second case, V(IV) impurities in surficial V_2O_5 islands result in enhanced charge-carrier recombination through hole-trapping followed by electron elimination. In the last case, V(IV) is substitutional in the TiO_2 lattice in the form of a solid solution, $V_xTi_{1-x}O_2$. The V(IV) centers trap both electrons and holes and thus yield enhanced charge-carrier recombination.

In the sixth chapter, the addition of inorganic oxidants such as HSO_5^-, ClO_3^-, IO_4^-, and BrO_3^- is found to increase the rate of degradation in the TiO_2/UV process. However, although several authors have speculated on the mechanism for increased quantum efficiencies, no mechanistic studies have previously been carried out. The sixth chapter details the mechanism by which the oxidants serve as efficient electron acceptors. BrO_3^- increases photoreactivity by scavenging conduction-band electrons and reducing charge-carrier recombination. The mechanism of ClO_3^-, however, is different. To account for the kinetic observations with ClO_3^-, it is proposed that competitive adsorption occurs among 4-CP, ClO_3^-, and O_2, and that the heterogeneous photodegradation of 4-

chlorophenol follows three parallel pathways. Each pathway is initiated photochemically and then proceeds via several thermal oxidation steps before the formation of a stable intermediate. When ClO_3^- is employed as an electron acceptor, a reaction pathway involving the thermal oxidation of the reactive intermediates is favored.

The seventh chapter discusses the implications of this thesis and suggests future research directions.

References

(1) Rife, R.; Thomas, T. W.; Norberg, D. W.; Fournier, R. L.; Rinker, F. G.; Bonomo, M. S. *Environ. Prog.* **1989**, *8*, 167-173.

(2) Pojasek, R. B. *Toxic and Hazardous Waste Disposal*; Ann Arbor Science: Ann Arbor, MI, 1979.

(3) Kim, B. J.; Gee, C. S.; Bandy, J. T.; Huang, C. S. *J. Water Pollution Control Fed.* **1991**, *63*, 501-509.

(4) Freeman, H. M. *INCINERATING HAZARDOUS WASTES*; Technomic Publishing Co.: Lancaster, PA, 1988.

(5) De Renzo, D. J. *Biodegradation Techniques for Industrial Organic Wastes*; Noyes Data Corporation: Park Ridge, NJ, 1980.

(6) *Photocatalytic Purification and Treatment of Water and Air*; Ollis, D. F.; Al-Ekabi, H., Ed.; Elsevier: Amsterdam, 1993.

(7)

(8) Mills, A.; Davies, R. H.; Worsley, D. *Chem. Soc. Rev.* **1993**, *22*, 417-425.

(9) Kamat, P. V. *Chem. Rev.* **1993**, *93*, 267-300.

(10) Fox, M. A.; Dulay, M. T. *Chem. Rev.* **1993**, *93*, 341-357.

(11) Bahnemann, D. W. *Israel J. Chem.* **1993**, *33*, 115-136.

(12) Pichat, P. *Catalysis Today* **1994**, *19*, 313-333.

(13) Aithal, U. S.; Aminabhavi, T. M.; Shukla, S. S. *J. Hazard. Mat.* **1993**, *33*, 369-400.

(14) Lewis, L. N. *Chem. Rev.* **1993**, *93*, 2693.

(15) Bahnemann, D.; Cunningham, J.; Fox, M. A.; Pelizzetti, E.; Serpone, N. In *Aquatic and Surface Photochemistry:*, G. R. Helz, R. G. Zepp and D. G. Crosby, Ed.; Lewis Publishers: Boca Raton, FL, 1994, p. 261-316.

(16) Fox, M. A. *Photochem. Photobiol.* **1990**, *52*, 617.

(17) Ollis, D. F.; Pelizzetti, E.; Serpone, N. *Environ. Sci. Technol.* **1991**, *25*, 1523-1529.

(18) Pelizzetti, E.; Serpone, N., Eds. *Homogeneous and Heterogeneous Photocatalysis*; D. Reidel Publishing Company: Dordrecht, 1986.

(19) Grätzel, M. *Heterogeneous Photochemical Electron Transfer*; CRC Press: Boca Raton, FL, 1989.

(20) Matthews, R. W. *Pure Appl. Chem.* **1992**, *64*, 1285-1290.

(21) Schiavello, M., Ed. *Photocatalysis and Environment: Trends and Applications*; Kluwer Academica Publishers: Dordrecht, 1988.

(22) Schiavello, M., Ed. *Photoelectrochemistry, Photocatalysis and Photoreactors*; D. Reidel Publishing Company: Dordrecht, 1985.

(23) Serpone, N.; Lawless, D.; Terzian, R.; Meisel, D. In *Electrochemistry in Colloids and Dispersions:*, R. A. Mackay and J. Texter, Ed.; VCH Publishers, Inc.: New York, 1992, p. 399-416.

(24) Serpone, N.; Pelizzetti, E., Eds. *Photocatalysis: Fundamentals and Applications*; John Wiley & Sons: New York, 1989.

(25) Anpo, M. In*Research on Chemical Intermediates:*, Ed.; Elsevier Science Publishers B.V.: Amsterdam, 1989, p. 67.

(26) Bahnemann, D. W.; Bockelmann, D.; Goslich, R. In *Solar Energy Materials:*, Ed.; Elsevier Science Publishers B.V.: North-Holland, 1991, p. 564-583.

(27) Henglein, A. *Chem. Rev.* **1989**, *89*, 1861.

(28) Ireland, J. C.; Klostermann, P.; Rice, E. W.; Clark, R. M. *Appl. Environ. Microbiol.* **1993**, *59*, 1668-1670.

(29) Sjogren, J. C.; Sierka, R. A. *Appl. Environ. Microbiol.* **1994**, *60*, 344-347.

(30) Cai, R. X.; Kubota, Y.; Shuin, T.; Sakai, H.; Hashimoto, K.; Fujishima, A. *Cancer Res.* **1992**, *52*, 2346-2348.

(31) Cai, R.; Hashimoto, K.; Kubota, Y.; Fujishima, A. *Chem. Lett.* **1992**, 427-430.

(32) Suzuki, K. In *Photocatalytic Purification and Treatment of Water and Air:*, D. F. Ollis and H. Al-Ekabi, Ed.; Elsevier: Amsterdam, 1993, p.

(33) Karakitsou, K. E.; Verykios, X. E. *J. Phys. Chem.* **1993**, *97*, 1184-1189.

(34) Grätzel, M. *Acc. Chem. Res.* **1981**, *14*, 376.

(35) Kalyanasundaram, K.; Borgarello, E.; Duonghong, D.; Grätzel, M. *Angew. Chem. Int. Ed. Engl.* **1981**, *20*, 987.

(36) Duonghong, D.; Borgarello, E.; Grätzel, M. *J. Am. Chem. Soc.* **1981**, *103*, 4685.

(37) Borgarello, E.; Kiwi, J.; Pelizzetti, E.; Visca, M.; Grätzel, M. *Nature* **1981**, *289*, 158.

(38) Wold, A. *Chem. Materials* **1993**, *5*, 280-283.

(39) Khan, M.; Rao, N. N. *J. Photochem. Photobiol. A Chem.* **1991**, *56*, 101-111.

(40) Schiavello, M. *Electrochim. Acta* **1993**, *38*, 11-14.

(41) Khan, M.; Chatterjee, D.; Krishnaratnam, M.; Bala, M. *J. Mol. Catalysis* **1992**, *72*, 13-18.

(42) Khan, M.; Chatterjee, D.; Bala, M. *J. Photochem. Photobiol. A Chem.* **1992**, *67*, 349-352.

(43) Gerischer, H.; Heller, A. *J. Electrochem. Soc.* **1992**, *139*, 113-118.

(44) Jackson, N. B.; Wang, C. M.; Luo, Z.; Schwitzgebel, J.; Ekerdt, J. G.; Brock, J. R.; Heller, A. *J. Electrochem. Soc.* **1991**, *138*, 3660-3664.

(45) Nair, M.; Luo, Z. H.; Heller, A. *Ind. Eng. Chem. Res.* **1993**, *32*, 2318-2323.

(46) Boer, K. W. *Survey of Semiconductor Physics*; Van Nostrand Reinhold: New York, 1990.

(47) Rothenberger, G.; Moser, J.; Grätzel, M.; Serpone, N.; Sharma, D. K. *J. Am. Chem. Soc.* **1985**, *107*, 8054.

(48) Memming, R. In *Topics in Current Chemistry:*, E. Steckham, Ed.; Springer-Verlag: Berlin, 1988, p. 79-113.

(49) Mills, G.; Hoffmann, M. R. *Environ. Sci. Technol.* **1993**, *27*, 1681-1689.

(50) Kormann, C.; Bahnemann, D. W.; Hoffmann, M. R. *Environ. Sci. Tech.* **1991**, *25*, 494-500.

(51) Carraway, E. R.; Hoffman, A. J.; Hoffmann, M. R. *Environ. Sci.Technol.* **1994**, *28*, 786-793.

(52) Chemeseddine, A.; Boehm, H. P. *J. Mol. Catalysis* **1990**, *60*, 295-311.

(53) D'Oliveira, J. C.; Minero, C.; Pelizzetti, E.; Pichat, P. *J. Photochem. Photobiol. A: Chem.* **1993**, *72*, 261-267.

(54) D'Oliveira, J. C.; Al-Sayyed, G.; Pichat, P. *Environ. Sci. Technol.* **1990**, *24*, 990-996.

(55) Hidaka, H.; Zhao, J.; Pelizzetti, E.; Serpone, N. *J. Phys. Chem.* **1992**, *96*, 2226-2230.

(56) Pelizzetti, E.; Minero, C.; Piccinini, P.; Vincenti, M. *Coord. Chem. Rev.* **1993**, *125*, 183-193.

(57) Albert, M.; Gao, Y. M.; Toft, D.; Dwight, K.; Wold, A. *Materials Res. Bull.* **1992**, *27*, 961-966.

(58) Inel, Y.; Ertek, D. *J. Chem. Soc. Faraday Trans.* **1993**, *89*, 129-133.

(59) Borgarello, E.; Serpone, N.; Emo, G.; Harris, R.; Pelizzetti, E.; Minero, C. *Inorg. Chem.* **1986**, *25*, 4499-4503.

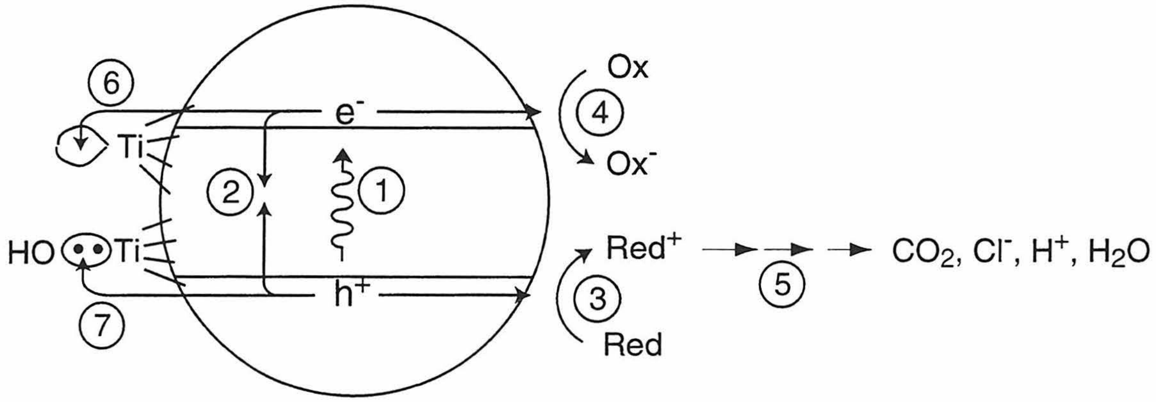

Figure 1: Primary steps in the photoelectrochemical mechanism. (1) Formation of charge-carriers by a photon. (2) Charge-carrier recombination to liberate heat. (3) Initiation of an oxidative pathway by a valence-band hole. (4) Initiation of a reductive pathway by a conduction-band electron. (5) Further thermal (e.g., hydrolysis or reaction with active oxygen species) and photocatalytic reactions to yield mineralization products. (6) Trapping of a conduction-band electron in a dangling surficial bond to yield Ti(III). (7) Trapping of a valence-band hole at a surficial titanol group.

Chapter 2

Time-Resolved Microwave Conductivity (TRMC): TiO_2 Photoreactivity and Size-Quantization

[The text of this chapter appeared in Martin, S.T., Herrmann, H., Choi, W., and Hoffmann, M.R. *Royal Society of Chemistry, Faraday Transactions*, **1994**, *90*, 3315.]

Abstract

Charge-carrier recombination dynamics after laser excitation are investigated by time-resolved microwave conductivity (TRMC) measurements of quantum-sized ("Q-") TiO_2, Fe(III)-doped Q-TiO_2, ZnO, and CdS, and several commerical bulk-sized TiO_2 samples. After pulsed laser excitation of charge-carriers, holes that escape recombination react with sorbed transdecalin within nanoseconds while the measured conductivity signal is due to conduction-band electrons remaining in the semiconductor lattice. The charge-carrier recombination lifetime and the interfacial electron-transfer rate constant that are derived from the TRMC measurements correlate with the CW photo-oxidation quantum efficiencies obtained for aqueous chloroform in the presence of TiO_2. The quantum efficiencies are 0.4% for Q-TiO_2, 1.6% for Degussa P25, and 2.0% for Fe(III)-doped Q-TiO_2. The lower quantum efficiencies for Q-TiO_2 are consistent with the relative interfacial electron-transfer rates observed by TRMC for Q-TiO_2 and Degussa P25. The increased quantum efficiencies of Fe(III)-doped Q-TiO_2 and the observed TRMC decays are consistent with a mechanism involving fast trapping of valence-band holes as Fe(IV) and inhibition of charge-carrier recombination.

Introduction

When the crystallite dimension of a semiconductor particle falls below a critical radius of approximately 10 nm, the charge-carriers appear to behave quantum-mechanically as a simple particle in a box.[1-6] As a result of this confinement, the bandgap increases and the band edges shift to yield larger redox potentials. The solvent reorganization free energy for charge transfer to a substrate, however, remains unchanged. The increased driving force and the unchanged solvent reorganization free energy in size-quantized systems are expected to increase the rate constant of charge transfer in the normal Marcus region.[7-9] Thus, the use of size-quantized semiconductor TiO_2 particles may result in increased photoefficiencies for systems in which the rate-limiting step is charge transfer.[10,11] One such system is the oxidation of many common organic pollutants in the presence of TiO_2 irradiated with bandgap illumination.[12-15]

The use of size-quantized semiconductors to increase photoefficiencies is supported by several studies.[10,16-19] However, in other work, size-quantized semiconductors have been found to be less photoactive than their bulk-phase counterparts.[11,20] In the latter cases, surface speciation and surface defect density appear to control photoreactivity.[21-23] The positive effects of increased overpotentials (i.e., difference between $E_{v.b.}$ and E_{redox}) on quantum yields can be offset by unfavorable surface speciation and surface defects due to the preparation method of size-quantized semiconductor particles.

In the present study, the photodegradation of several chlorinated compounds in the presence of Q-TiO_2 are used as control reactions to study the size-quantization effect on photoreactivity. The stoichiometry of the reactions is as follows:

$$C_xH_yCl_z + \left(x + \frac{y-z}{4}\right)O_2 \xrightarrow[h\nu,\, TiO_2]{} x\,CO_2 + z\,H^+ + z\,Cl^- + \left(\frac{y-z}{2}\right)H_2O \qquad (1)$$

The photodegradations of chloroform[24], pentachlorophenol[25,26], and 4-chlorophenol[27-31] with Degussa P25 (i.e., a bulk-phase TiO_2 consisting of 80% anatase and 20% rutile) have been studied previously. P25 is a commerical form of TiO_2 that generally has a higher photoreactivity than other available forms of TiO_2.

The variable photoefficiencies of the different forms of TiO_2 are related to their fundamental charge-carrier dynamics. In order to verify this relationship, we investigate the charge-carrier dynamics of Q-TiO_2 and P25 by time-resolved microwave conductivity (TRMC) measurements.[32-38] In a typical TRMC experiment, separated charge-carriers, which are generated by a laser pulse, lead to a perturbation of the initial microwave absorbance.[33,39] The temporal decay of the conductivity signal (i.e., microwave absorbance) reflects the lifetime of the photogenerated carriers. The technique has only recently been expanded to semiconductor particles,[34-38,40,41] for which conventional techniques (e.g., photoconductivity) are often not possible due to the necessity of electrode contacts. Efforts have been made here to provide experimental details of the TRMC technique, including the development of a novel sample holder that is usable in conjunction with conventional lasers.

Experimental Section

Preparation. Q-TiO_2 was prepared by the controlled hydrolysis of titanium (IV) tetraisopropoxide.[42] 5 ml $Ti(OCH(CH_3)_2)_4$ (Aldrich, 97%) dissolved in 100 ml isopropanol was added dropwise (90-120 min.) under vigorous stirring to 900 ml doubly-distilled water (2°C) adjusted to pH 1.5 with HNO_3. The transparent colloid can be stored for over one year in a cold room (4°C) without coagulation. To obtain a powdered sample, 150 ml of the colloidal solution was evaporated (35°C) using a Rotavapor (model R110). The resulting film was dried with a N_2 stream to yield a white powder. Iron(III)-doped Q-TiO_2 was prepared by a similar procedure in the presence of $Fe(NO_3)_3$ to give an atomic doping level of 1%. Full incorporation of Fe(III) into the lattice has been shown by other workers.[43,44]

The bulk-phase semiconductors used were ZnO (Baker), α-Fe_2O_3 (Hematite, Fisher), CdS (Alfa), and TiO_2 (Degussa P25 and Sachtleben Chemie P7, P13, P17, P18, P21, and P24). We used two separate batches of Degussa P25, which were obtained in 1988 (P25-A) and 1993 (P25-B).

Characterization. Particle sizes were determined by a Philips EM 430 transmission electron microscope (TEM) at 300 kV. Samples for TEM were prepared by placing a drop onto a copper mesh substrate covered with a carbon film, followed by removal of the excess liquid with a piece of thin filter paper and drying 30 seconds under a tungsten lamp. A representative transmission electron micrograph is shown in Figure 1. The sizes of the Q-particles ranged from 2 to 4 nm with a lattice spacing of 3.6 ± 0.1 Å. This spacing was in good agreement with the anatase (101) phase lattice spacing of 3.51 Å.[45] X-ray diffraction (XRD) analysis was carried out with powdered samples on a Scintag PAD5 model DMC-008 using 35 kV, 20 mA Cu-K_α (1.54 Å) radiation. The diffraction pattern of the Q-sized TiO_2 was also characteristic of anatase. The observed line broadening due to the presence of small crystallites was analyzed by the Scherrer equation[46] and showed that the particles were 3-4 nm in diameter.

Degussa P25 has been characterized previously.[47,48] Thirty nanometer crystallites composed of 80% anatase and 20% rutile aggregrate to form particles with an average diameter of 1 μm. For the TRMC experiments, P25 (1.44 g/L) was suspended in HNO_3 (pH 1.5) and rotary evaporated to a dry powder. The characterization of the TiO_2 samples obtained from Sachtleben Chemie is shown in Table 1.[49]

Irradiation. Steady-state photolyses were carried out in a slurry reactor to determine the initial rate constants for the degradation of chloroform (Baker), dichloroacetic acid (Spectrum Chemical Manufacturing, Inc.), carbon tetrachloride (Baker), pentachlorophenol (Aldrich), and 4-chlorophenol (Aldrich). Irradiations were performed with a 1000 W Xe arc lamp (Spindler and Hoyer). The infrared component of the incident light was removed by a 10-cm water filter. Depending upon the experiment, wavelengths were selected with an interference filter (Oriel, $\lambda = 320 \pm 5$ nm), a longpass filter (Oriel, $\lambda > 320$ nm), or a bandpass filter (Corning 7-60-1, $320 < \lambda < 380$ nm). Light intensity was adjusted with neutral density filters. The chemical actinometer Aberchrome 540 ((E)-α-(2,5-dimethyl-3-furyl)ethylidene)-3-isopropylidenesuccinic anhydride) was used to determine the incident light intensity, which was found to vary between 100 and 200 μM min^{-1} with the interference filter in place and to be 1000 μM min^{-1} with the longpass filter.[50] Aqueous suspensions (35 mL) of the chlorinated compounds and TiO_2 (1.0 g/L) were prepared, and the pH was adjusted by the addition of HNO_3. Initial degradation rates were determined by the total Cl^- release after one hour of illumination in the case of $HCCl_3$ (63 mM), DCA (4.8 mM), and CCl_4 (5.1 mM) and by HPLC (Hewlett Packard Series II 1090 Liquid Chromatograph) analysis for PCP (60 μM) and 4-CP (100 μM). Chloride concentrations were determined with an Orion chloride selective electrode (model no. 9617B).

TRMC Measurements. A schematic diagram of the microwave conductivity apparatus is shown in Figure 2. A Gunn diode microwave source (100 mW, 38.3 GHz, MACOM, Inc.), a PIN diode microwave detector, a Comlinear model CLC206AI amplifier, a TEK 2440 digitizing oscilloscope, and an HP 432A power meter were coupled into the TRMC unit. The source, detector, and amplifier were enclosed in aluminum Faraday cages. The waveguide system was R-band WR-28 (0.711 x 0.356 cm). A Lambda Physik excimer laser (LPX 120) was used for a 308 nm, 50 ns pulse excitation source. Layered metal mesh interposed between the laser and the sample was used to control incident light intensity, which was 4.5 mJ per pulse unless otherwise stated. In a typical experiment, between 32 and 256 conductivity decays were averaged to improve the signal-to-noise ratio. The digitized data were transferred to a computer for storage and data analysis. The data were collected on four time scales (200 ns/div, 2 μs/div, 200 μs/div, and 10 ms/div). The transients were reproducible within 5% error.

The sample holder, which was designed especially for this series of experiments, is shown in Figure 3. The top plate (i.e., short) has seven slits cut orthogonal to the propagating microwave mode so that laser light can enter the waveguide while the microwaves are reflected back into the waveguide. The sample was prepared as a thick paste supported in transdecalin (Aldrich). The paste was molded into a teflon holder with an illuminated surface area of 13.9 mm^2. The teflon holder was fit into the waveguide at a distance of 1.65 mm from the short. The holder was positioned by the use of an aluminum block inserted from the rear of the waveguide upon which the holder was pressed.

The principles of the TRMC experiment have been discussed previously.[32,33,51] Microwaves from the source pass through the sample and impact on the PIN diode detector, which then transforms the incident microwave power into a voltage for input to the oscilloscope. The absorbed microwave power is directly proportional to the conductivity of the sample, σ, for low conductivity samples.[32] The proportionality constant, A, is specific to the geometry of the apparatus and the sample, and it is determined by calibration. The change in absorbed microwave power, ΔP, due to a change in conductivity, $\Delta\sigma$, caused by carrier excitation is given by eq 2 where P is the initial microwave power level.

$$\frac{\Delta P(t)}{P} = A\,\Delta\sigma(t) \tag{2}$$

The microwave power is transformed into a voltage, V, by the PIN diode detector as $P = V^n$. For perturbations below 3%, the response is linear, as shown in eq 3.[32]

$$\frac{\Delta P}{P} = n\left(\frac{\Delta V}{V}\right) \tag{3}$$

The proportionality constant, n, is typically between 1 and 2 and is found by calibration. Substitution of eq 2 into eq 3 results in eq 4.

$$\Delta V(t) = \left(\frac{VA}{n}\right)\Delta\sigma(t) \tag{4}$$

The temporal behavior of the voltage observed at the digitizer and the conductivity of the sample are thus proportional.

Principles of TRMC

When free charge-carriers couple to the electric field of the microwaves, absorption occurs.[39] The strength of the interaction is expressed in terms of mobilities. The mobilities of a free electron in He gas (1 m^2/Vs), of free carriers in Si (0.2), of a hopping electron in an organic compound (10^{-3} to 10^{-4}), of ions in solution (10^{-7} to 10^{-8}), and of dipole moments (10^{-9} to 10^{-12}) reflect the relative coupling efficiencies at microwave frequencies.[33] The interpretation of TRMC measurements of polar molecules in nonpolar solvents and of free carriers in silicon are generally understood[32,33,51-53]; however, the interpretation of the conductivity decays of semiconductor particles with low carrier mobilities ($<10^{-4}$ m^2/Vs) has not been addressed previously. In high-mobility semiconductors such as GaAs (8900 m^2/Vs), Si (1950), ZnO (380), or CdS (390), the microwave absorption can be attributed to free carriers.[32,54] Furthermore, for these semiconductors with the exception of ZnO, the electron mobility is several times larger than the hole mobility so that the observed conductivity decay is attributable entirely to free electrons. For low mobility semiconductors such as TiO_2 (10^{-4} to 10^{-5} m^2/Vs)[55] and α-Fe_2O_3 (10^{-5})[56], the microwave absorbance may not be due exclusively to free carriers. The mobility of a shallow trap may be similar to that of a hopping electron in an organic compound (10^{-3} to 10^{-4} m^2/Vs); therefore, in these cases free and shallowly-trapped carriers may simultaneously contribute to the conductivity decay of TiO_2. Examples of shallowly-trapped carriers in TiO_2 at 25° C include small polarons[57] and electrons on Ti(III) sites[40].

Results

Initial degradation rates of chloroform as a function of the concentration of chloroform and the type of TiO_2 are illustrated in Figure 4. At the solubility limit for aqueous chloroform (63 mM), the quantum yield for chloride release is 0.4% for Q-TiO_2 and 1.6% for P25-A. Doping of the Q-TiO_2 with Fe(III) at 1.0 atom percent level shows an increase in the quantum yield to 2.0%. Initial degradation quantum efficiencies of chloroform, dichloroacetic acid (DCA), carbon tetrachloride, pentachlorophenol (PCP), and 4-chlorophenol (4-CP) are shown in Table 2 for Q-TiO_2 and P25-A. The quantum efficiencies obtained with Q-TiO_2 are less than those obtained with P25-A.

The observed microwave conductivity decays of ZnO, CdS, P25, and Al_2O_3 are shown in Figure 5. Since the signal strengths and timescales of decay vary over several orders of magnitude, the data are represented in log-log form. Alumina (α-Al_2O_3), which has a bandgap of 9.5 eV, serves as a blank for the apparatus and indicates the minimum detection limit.[35] For direct comparison, NaCl shows a similar decay profile. The relative rates of decay can be characterized by the half-life signal decay. For ZnO, the first half-life is 6.6 μs and the second is 164 μs. For CdS, the first half-life is 60 ns, the second is 770 ns, and the third is 9.2 μs. For P25-A, the first half-life is 1.1 μs and the second is 1.7 ms. Several investigators have reported that the half-lives for conductivity decay in CdS and TiO_2 increase as the decay time increases; our observations are consistent with these previous reports.[34,40,41]

For example, Schindler and Kunst reported a $\tau_{1/2}$ for P25 of 2.0 μs for the conductivity obseved at 100 ns.[40] This value agrees reasonably with our value of 1.1 μs for P25-A.

The initial degradation rates of chloroform as a function of light intensity are shown in Figure 6. Two linear regions are observed, and the cross-over occurs at 150 μM min^{-1}. The quantum efficiencies vary from 2.5% for I = 50 μM min^{-1} to 0.3% for I = 1490 μM min^{-1}. In Figure 7, the time-resolved conductivities at 100 ns of P25-A prepared in HNO_3 and transdecalin are plotted as a function of the incident laser pulse energy. Two linear regions are identified with an apparent cross-over at a pulse energy of 6 mJ.

Representative conductivity decays for TRMC measurements of P7, P13, P17, P18, P21, P24, and P25-B are shown in Figure 8. For most samples, the interfacial electron-transfer rate constants reported in Tables I & III are calculated by single exponential fits of the conductivity data. However, in the case of P17 and P24, the signal-to-noise ratio is too low to facilitate an exponential fit of the data. Discrepancies between similar samples in Table 1 & III are due to differences in the pre-amplifier, the incident pulse energy (2.5 mJ in Table 1), CW illumination intensity, and batches of P25.

A contour plot of the quantum efficiencies reported in Table 1 as a function of the recombination lifetime and the interfacial electron-transfer rate constant is shown in Figure 9a. The arrows on the data points for P17 and P24 indicate the interfacial electron-transfer rate constant is unknown. The charge-carrier recombination lifetimes (*vide infra*) are the charge-carrier concentrations (@100 ns) reported in Tables I & III. The contours drawn fit the function $C = x \bullet y$. A plot of C versus the product of x and y results in a straight line, as shown in Figure 9b where C is the quantum efficiency and $x \bullet y$ is the contour value, i.e., the product of the recombination lifetime and the interfacial electron-transfer rate constant, k. The data points for P17 and P24 are calculated using k = 0.15 ms^{-1} and the extrema of the arrows are calculated for k = 0.03 ms^{-1} and k = 0.30 ms^{-1}. Figure 9b demonstrates more clearly than Figure 9a the correlations observed between photoreactivity and charge-carrier dynamics.

To investigate the effect of HNO_3, P25-A was prepared by rotary evaporation from an acidic slurry (HNO_3, pH 1.5) and was then supported in a transdecalin paste for the conductivity measurements. In a separate preparation, P25-A was directly prepared as a paste in transdecalin. The conductivity decays are shown in Figures 10. It is apparent that the temporal behavior of the coated and uncoated samples is similar. In addition, the conductivity decays of Q-TiO_2 and Fe(III)-doped Q-TiO_2 are overlayed in Figure 10. The TRMC measurements for these samples are summarized in Table 3.

Discussion

In previous papers, we proposed that the larger overpotentials in Q-TiO_2 versus bulk-phase TiO_2 should lead to higher quantum yields.[10,11,58] However, the data in Figure 4 clearly shows that Q-TiO_2 is less photoreactive than P25-A. In similar experiments carried out with substrates representing a variety of postulated mechanistic pathways, including direct hole attack on $HCCl_3$ and DCA[24], hydroxyl radical attack of 4-CP and PCP[27-31,59], and electron transfer to CCl_4[10,11,42,60], the quantum efficiencies (cf. Table 1) obtained for Q-TiO_2 appear to be consistently lower than those obtained for bulk-phase P25. These data suggest several possibilities. On one hand, the lower photoreactivty of Q-TiO_2 may be due to an increased rate of charge-carrier recombination. On the other hand, there may be substantial differences in the interfacial charge-transfer rates between Q-TiO_2 and P25-A.

The differences between Q-TiO_2 and P25-A are at least partially understood by considering the preparation methods that may result in more defect sites (trapping sites) and faster recombination rates in Q-TiO_2. P25-A TiO_2 is prepared in a high temperature flame reactor and is thus expected to have fewer defects[47,48] whereas Q-TiO_2 is prepared by sol-gel techniques at much lower temperatures. Different surface morphologies (e.g., hydroxylation density) may also be expected, and the interfacial charge-transfer rates may be controlled by the relative formation of surface complexes on Q-TiO_2 as compared to P25-A.

The relationship between the charge-carrier recombination rate and quantum efficiency can be expressed as follows:

$$\phi_{transfer} = \frac{rate_{transfer}}{rate_{transfer} + rate_{recombination}} \tag{5}$$

If the charge-carrier recombination rate in Q-TiO_2 increases due to defects, then the quantum efficiency of interfacial charge transfer decreases and Q-TiO_2 should be less photoreactive than P25.

The observed conductivity decays in our TRMC experiments should yield the recombination rates of photogenerated free charge-carriers. However, the TRMC response is influenced by other deactivation pathways such as interfacial charge transfer to adsorbed species. In these cases, the conductivity decays may be due to both recombination and charge transfer, and the data must be deconvoluted.[34-38,40,41] In the absence of recombination or charge-carrier localization during the laser pulse, the conductivity measured after the laser pulse should be proportional to the number of free charge-carriers:

$$\Delta\sigma = qN\left(\mu_{e^-} + \mu_{h^+}\right) \tag{6}$$

where N is the number of absorbed photons (if equal reflectivities and short penetration depths are assumed among the samples). The data of Figure 5 are consistent with the prediction of eq 6 that the strength of the conductivity signal increases with the mobility of the charge-carriers ($\sum\mu_{ZnO} = 380\ \mathrm{cm}^2/\mathrm{V\,s}$[54], $\sum\mu_{CdS} = 300$[34], and $\sum\mu_{TiO_2} = 1$[35]). From eq 4 we see that

$$\Delta V = \left(qNVA/n\right)\left(\mu_{e^-} + \mu_{h^+}\right). \tag{7}$$

Eq 7 predicts a linear correlation between the post-pulse conductivity, ΔV, and the sum of the mobilities with a corresponding slope of (q N V/n)A. Using this relationship, our specific apparatus constant, A, can be evaluated. A linear fit applied to the data in Figure 5 yields a slope of 0.28 mV/($\mathrm{cm}^2\ \mathrm{V}^{-1}\ \mathrm{s}^{-1}$), $r^2 = 0.81$, and $A = 1.1 \times 10^3\ \mathrm{S}^{-1}$. Since $r^2 < 1$, there is a high probability that localization (i.e., recombination or interfacial charge transfer) has taken place during the laser pulse. Thus, we consider the above A value to be a lower estimate.

Photoelectrochemical Mechanisms. We propose the following four processes for charge-carrier recombination:[59,61-63]

Charge-Carrier Generation

$$TiO_2 + h\nu \xrightarrow{k_8} e^-_{c.b.} + h^+_{v.b.} \tag{8}$$

Direct and Indirect Charge-Carrier Trapping

$$e^-_{c.b.} + T_{e^-} \xrightarrow{k_9} e^-_T \tag{9}$$

$$h^+_{v.b.} + T_{h^+} \xrightarrow{k_{10}} h^+_T \tag{10}$$

Charge-Carrier Recombination

$$e^-_{c.b.} + h^+_{v.b.} \xrightarrow{k_{11}} TiO_2 \tag{11}$$

$$e^-_{c.b.} + h^+_T \xrightarrow{k_{12}} TiO_2 + T_{h^+} \tag{12}$$

$$h^+_{v.b.} + e^-_T \xrightarrow{k_{13}} TiO_2 + T_{e^-} \tag{13}$$

Interfacial Charge Transfer

$$e^-_{c.b.} + O \xrightarrow{k_{14}} O^- \tag{14}$$

$$e^-_T + O \xrightarrow{k_{15}} O^- + T_{e^-} \tag{15}$$

$$h^+_{v.b.} + R \xrightarrow{k_{16}} R^+ \tag{16}$$

$$h^+_T + R \xrightarrow{k_{17}} R^+ + T_{h^+} \tag{17}$$

where e^-_T is a trapped electron, h^+_T is a trapped hole, T_{e^-} is an empty electron trap, T_{h^+} is an empty hole trap, O is an electron acceptor (oxidant), and R is a an electron donor (reductant). At present, we believe that the the electron is trapped in a surficial Ti(III) site[42,64,65] while the hole is trapped in a surficial hydroxyl group.[42,66,67]

Based on this mechanism we can write an equation for the change in microwave conductivity as follows:

$$\frac{d\sigma}{dt} = \mu_{e^-_{c.b.}} \frac{d[e^-_{c.b.}]}{dt} + \mu_{e^-_T} \frac{d[e^-_T]}{dt} + \mu_{h^+_{v.b.}} \frac{d[h^+_{v.b.}]}{dt} + \mu_{h^+_T} \frac{d[h^+_T]}{dt} \qquad (18)$$

For ZnO, $\mu_{e^-_T} \frac{d[e^-_T]}{dt}$ and $\mu_{h^+_T} \frac{d[h^+_T]}{dt}$ can be omitted from eq 18 due to the high mobility of the free charge-carriers. However, in the case of TiO_2, these terms must be included since shallowly-trapped and free electrons have comparable mobilities. Even though the observed microwave conductivity signal is due to a mixture of species and mobilities, we believe that the observed conductivity as shown in Figures 8 and 10 can be assigned primarily to electrons (i.e., $\mu_{e^-_{c.b.}} \frac{d[e^-_{c.b.}]}{dt}$ and $\mu_{e^-_T} \frac{d[e^-_T]}{dt}$).

In order to explain the timescales for the microwave conductivity decays shown in Figures 8 and 10, a mechanism that includes interfacial charge transfer must be invoked because recombination is complete in ~100 ns in the absence of interfacial charge transfer.[62,68] In order for the kinetics of the charge transfer to compete with recombination processes internal to the TiO_2 particle, interfacial charge transfer of at least one carrier should occur within several nanseconds.[68] Therefore, only one charge-carrier type (i.e, holes or electrons) should be present in the particle after 100 ns. Because hole transfer often takes place within nanoseconds while electron transfer takes place over the timescale of nanoseconds to milliseconds,[42,64,69] we conclude that electrons give rise to the measured TRMC conductivty.

The overall quantum efficiency for interfacial charge transfer is determined by two critical processes: the competition between carrier recombination and trapping (ps to ns) followed by the competition between carrier recombination and interfacial charge transfer (μs to ms). The measurement of the conductivity at 100 ns contains information on fast recombination while the measurement at longer timescales yields information on interfacial charge transfer. The falloff in the remaining charge-carriers at 100 ns with increasing injection level is shown in Figure 7. The apparent discontinuity at 6 mJ suggests that a higher-order channel is opened with fewer residual charge-carriers at 100 ns. These results are consistent with the inverse relationship observed between quantum efficiency for $CHCl_3$ oxidation and light intensity shown in Figure 6.[16,24] Based on these results, we believe that the recombination lifetime of charge-carriers is inversely proportional to the conductivity at 100 ns.

An increase in either the recombination lifetime of charge-carriers or the interfacial electron-transfer rate constant is expected to result in higher quantum efficiencies for CW photolyses. The samples P7-P25 are observed to follow this relationship in Figure 9a. The linear transformation of the contour plot in Figure 9b makes the correlation more apparent. Figure 9a suggests P21 owes its high photoreactivity to a fast interfacial electron-transfer rate constant whereas P25 has a high photoreactivity due to slow recombination. Bickley et al. have suggested that anatase/rutile structure of P25 promotes charge-pair separation and inhibits recombination.[47] The different recombination lifetimes and interfacial electron-transfer rate constants may be due to the different preparation methods of the samples that result in different crystal defect structures and surface morphologies.

A conduction band electron is thermodynamically capable of reducing H^+, NO_3^-, O_2, and oxidized transdecalin radicals (T^+) while a valence band hole is sufficiently powerful to oxidize transdecalin. The signal strength observed in Figure 10a for P25-A in the presence of HNO_3 is reduced relative to the uncoated P25-A. This relative change may be due to a fast reduction of H^+ or NO_3^- in the first monolayer or to an inhibition of hole transfer which results in greater charge-carrier recombination. However, the time-dependence of the conductivity decay appears to be unchanged in the presence of HNO_3. In contrast, the fast time-scale recombination observed for Q-TiO_2 and P25-A (NO_3^-) appears to be similar as shown in Table 3. This observation suggests that a similar number of defects are present in each material. In general, the time-dependent changes summarized in Figure 10 indicate that electrons undergo interfacial charge transfer more slowly for Q-TiO_2 ($k = 0.052\ ms^{-1}$) than for P25-A ($k = 0.065\ ms^{-1}$). This result is consistent with the observed lower steady-state quantum yields (Table 1).

Fe(III)-Doped TiO_2. EPR and transient absorption studies have shown that Fe(III) doping in colloidal TiO_2 acts by trapping holes as Fe(IV) within several nanoseconds of excitation and that slow recombination takes place by tunneling from electrons trapped at surface Ti(III) sites to holes trapped at bulk-phase Fe(IV) sites.[43,70] The Fe(III) dopant thus acts to inhibit charge-carrier recombination. These processes can be written in terms of reactions 19 and 20, respectively:

$$Fe(III) + h^+ \xrightarrow{k_{19}} Fe(IV) \tag{19}$$

$$Fe(IV) + Ti(III) \xrightarrow{k_{20}} TiO_2\text{-}Fe(III) \tag{20}$$

The oxidation of the sorbed electron donor is written as:

$$Fe(IV) + R \xrightarrow{k_{21}} TiO_2\text{-}Fe(III) + R^+ \tag{21}$$

A flat microwave signal in Figures 10 is consistent with the inhibition of carrier recombination within the iron-doped sample. However, the conductivity signal at 100 ns is weaker for the Fe(III)-doped sample than for the undoped sample. The mobility of the electrons in Fe(III)-doped Q-TiO_2 may be significantly reduced because Fe(III) is present at a concentration of 2.9 x 10^{20} cm^{-3}. For example, the mobility of an electron in silicon drops from 1100 cm^2/ V s to 100 cm^2/ V s in a similarly doped lattice.[71] The net effect is a lower initial microwave conductivity for Fe(III)-doped Q-TiO_2.

In summary, we believe the hole, which is trapped at a Fe(IV) site, is transferred to an adsorbed substrate on a submillisecond time scale while the interfacial electron transfer occurs on the millisecond scale (eqs 14 and 15). As a result, we predict higher steady-state quantum efficiencies for Fe(III)-doped Q-TiO_2. This prediction is supported by results shown in Figure 4.

Conclusions

After pulse laser excitation of charge-carriers, holes which escape band-gap recombination are transferred to the sorbed electron-donor transdecalin within nanoseconds. The TRMC conductivity signals are due to electrons remaining in the semiconductor lattice after hole transfer. The resultant interfacial electron transfer takes place over milliseconds and appears to be faster for P25 than for Q-TiO_2. The slower electron transfer rates observed for Q-TiO_2 are consistent with the lower steady-state quantum yields. Iron(III)-

doped into the Q-TiO_2 matrix serves to trap holes as Fe(IV) and thus reduces charge-carrier recombination, which in turn results in increased quantum efficiencies. The correlations observed between quantum efficiencies and charge-carrier dynamics emphasize the importance of the interfacial charge transfer rate constant and the charge-carrier recombination lifetime as contributing factors to TiO_2 photoreactivity.

Acknowledgment. We are indebted to Prof. Nathan S. Lewis for the loan of microwave components, to Prof. Geoffrey A. Blake for the use of the excimer laser, and to Dr. Detlef W. Bahnemann for providing the Sachtleben Chemie samples. We are grateful to ARPA and ONR {NAV 5 HFMN N0001492J1901} for financial support. S. Martin is supported by a National Defense Science and Engineering Graduate Fellowship. H. Hermann wishes to thank NATO/DAAD for financing a research visit at the California Institute of Technology. Nicole Peill, Dr. Amy Hoffman, and Dr. Andreas Termin provided valuable support and stimulating discussion.

References

(1) Brus, L. *Appl. Phys. A.* **1991**, *53*, 465.

(2) Weller, H. *Adv. Mater.* **1993**, *5*, 88.

(3) Grätzel, M. *Nature* **1991**, *349*, 740.

(4) Weller, H. *Angew. Chem.* **1993**, *32*, 41.

(5) Henglein, A. *T. Curr. Chem.* **1988**, *143*, 113.

(6) Kamat, P. V. *Chem. Rev.* **1993**, *93*, 267.

(7) Marcus, R. A.; Sutin, N. *Biochimica et Biophysica Acta* **1985**, *811*, 265.

(8) Marcus, R. A. *J. Phys. Chem.* **1990**, *94*, 1050.

(9) Lewis, N. S. *Annu. Rev. Phys.* **1991**, *42*, 543.

(10) Hoffman, A. J.; Mills, G.; Yee, H.; Hoffmann, M. R. *J. Phys. Chem.* **1992**, *96*, 5546.

(11) Hoffman, A. J.; Yee, H.; Mills, G.; Hoffmann, M. R. *J. Phys. Chem.* **1992**, *96*, 5540.

(12) Schiavello, M., Ed. *Photocatalysis and Environment: Trends and Applications*; Kluwer Academica Publishers: Dordrecht, 1988.

(13) Pelizzetti, E.; Serpone, N., Eds. *Homogeneous and Heterogeneous Photocatalysis*; D. Reidel Publishing Company: Dordrecht, 1986.

(14) Schiavello, M., Ed. *Photoelectrochemistry, Photocatalysis and Photoreactors*; D. Reidel Publishing Company: Dordrecht, 1985.

(15) Serpone, N.; Pelizzetti, E., Eds. *Photocatalysis: Fundamentals and Applications*; John Wiley & Sons: New York, 1989.

(16) Hoffman, A. J.; Carraway, E. R.; Hoffmann, M. R. *Environ. Sci. Technol.* **1994**, *28*, 776.

(17) Anpo, M.; Shima, T.; Kodama, S.; Kubokawa, Y. *J. Phys. Chem.* **1987**, *91*, 4305.

(18) Nedeljkovic, J. M.; Nenadovic, M. T.; Micic, O. I.; Nozik, A. J. *J. Phys. Chem.* **1986**, *90*, 12.

(19) Nosaka, Y.; Ohta, N.; Miyama, H. *J. Phys. Chem.* **1990**, *94*, 3752.

(20) Giuseppe, P.; Langford, C. H.; Vichova, J.; Vleck, A. *J. Photochem. Photobiol. A: Chem.* **1993**, *75*, 67.

(21) Lee, W.; Gao, Y.-M.; Dwight, K.; Wold, A. *Mat. Res. Bull.* **1992**, *27*, 685.

(22) Nishimoto, S.; Ohtani, B.; Kajiwara, H.; Kagiya, T. *J. Chem. Soc., Faraday Trans. 1* **1985**, *81*, 61.

(23) Faust, B. C.; Hoffmann, M. R.; Bahnemann, D. W. *J. Phys. Chem.* **1989**, *93*, 6371.

(24) Kormann, C.; Bahnemann, D. W.; Hoffmann, M. R. *Environ. Sci. Technol.* **1991**, *25*, 494.

(25) Mills, G.; Hoffmann, M. R. *Environ. Sci. Tech.* **1993**, *27*, 1681.

(26) Barbeni, M.; Pramauro, E.; Pelizzetti, E. *Chemosphere* **1985**, *14*, 195.

(27) Al-Ekabi, H.; Serpone, N.; Pelizzetti, E.; Minero, C. *Langmuir* **1989**, *5*, 250.

(28) Al-Sayyed, G.; D'Oliveira, J. C.; Pichat, P. *J. Photochem. Photobiol. A: Chem.* **1991**, *58*, 99.

(29) Barbeni, M.; Pramauro, E.; Pelizzetti, E.; Brogarello, E.; Grätzel, M.; Serpone, N. *Nouv. J. Chemie* **1984**, *8*, 547.

(30) Durand, A. P. Y.; Brattan, D.; Brown, R. G. *Chemosphere* **1992**, *25*, 783.

(31) Mills, A.; Morris, S.; Davies, R. *J. Photochem. Photobiol. A: Chem.* **1993**, *70*, 183.

(32) Kunst, M.; Beck, G. *J. Appl. Phys.* **1986**, *60*, 3558.

(33) Warman, J. M.; de Haas, M. P. In *Pulse Radiolysis*; Y. Tabata, Ed.; CRC Press: Boca Raton, 1991; chp. 6.

(34) Warman, J. M.; de Haas, M. P.; van Hovell tot Westerflier, S. W. F. M.; Binsma, J. J. M.; Kolar, Z. I. *J. Phys. Chem.* **1989**, *93*, 5895.

(35) Warman, J. M.; de Haas, M. P.; Pichat, P.; Koster, T. P. M.; van der Zouwen-Assink, E. A.; Mackor, A.; Cooper, R. *Radiat. Phys. Chem.* **1991**, *37*, 433.

(36) Fessenden, R. W.; Kamat, P. V. *Chem. Phys. Lett.* **1986**, *123*, 233.

(37) Warman, J. M.; de Haas, M. P.; Grätzel, M.; Infelta, P. P. *Nature* **1984**, *310*, 306.

(38) Warman, J. M.; de Haas, M. P.; Pichat, P.; Serpone, N. *J. Phys. Chem.* **1991**, *95*, 8858.

(39) Ramo, S.; Whinnery, J. R.; van Duzer, T. *Fields and Waves in Communication Electronics*; John Wiley & Sons: New York, 1984.

(40) Schindler, K. M.; Kunst, M. *J. Phys. Chem.* **1990**, *94*, 8222.

(41) Warman, J. M.; de Haas, M. P.; Wentinck, H. M. *Radiat. Phys. Chem.* **1989**, *34*, 581.

(42) Bahnemann, D.; Henglein, A.; Lilie, J.; Spanhel, L. *J. Phys. Chem.* **1984**, *88*, 709.

(43) Moser, J.; Grätzel, M.; Gallay, R. *Helvetica Chimica Acta* **1987**, *70*, 1596.

(44) Bahnemann, D. W. *Isr. J. Chem.* **1993**, *33*, 115.

(45) *Powder Diffraction File, Sets 21-22*; JCPDS: Swarthmore, 1980; Vol. PD1S-22iRB, pp 21-1272.

(46) Cullity, B. D. *Elements of X-Ray Diffraction;* 2nd ed.; Addison-Wesley: Reading, 1978, pp 102.

(47) Bickley, R. I.; Gonzalez-Carreno, T.; Lees, J. S.; Palmisano, L.; Tilley, R. J. D. *J. Solid State Chem.* **1991**, *92*, 178.

(48) "Degussa Technical Bulletin No. 56," 1990.

(49) Bahnemann, D. W. *Personal communication*

(50) Heller, H. G.; Langan, J. R. *J. Chem. Soc. Perkin Trans.* **1981**, *2*, 341.

(51) Infelta, P. P.; de Haas, M. P.; Warman, J. M. *Radiat. Phys. Chem.* **1977**, *10*, 353.

(52) Fessenden, R. W.; Carton, P. M.; Shimamori, H.; Scalano, J. C. *J. Phys. Chem.* **1982**, *86*, 3803.

(53) Kunst, M.; Sanders, A. *Semicond. Sci. Technol.* **1992**, *7*, 51.

(54) Sze, S. M. In *Physics of Semiconductor Devices* John Wiley: New York, 1981; .

(55) Finklea, H. O. In *Semiconductor Electrodes*; H. O. Finklea, Ed.; Elsevier: New York, 1988; ; pp 52.

(56) Anderman, M.; Kennedy, J. H. In *Semiconductor Electrodes*; H. O. Finklea, Ed.; Elsevier: New York, 1988; ; pp 153.

(57) Mott, N. F.; Davis, E. A. In *Electronic Processes in Non-Crystalline Materials* Clarendon Press: Oxford, 1971; ; pp 117ff.

(58) Bahnemann, D. W.; Kormann, C.; Hoffmann, M. R. *J. Phys. Chem.* **1987**, *91*, 3789.

(59) Serpone, N.; Lawless, D.; Terzian, R.; Meisel, D. In *Electrochemistry in Colloids and Dispersions*; R. A. Mackay and J. Texter, Ed.; VCH Publishers, Inc.: New York, 1992; ch. 30; Vol. ; pp 399-416.

(60) Prairie, M.; Evans, L. R.; Stange, B. M.; Martinez, S. L. *Environ. Sci. Technol.* **1993**, *27*, 1776.

(61) Turchi, C. S.; Ollis, D. F. *J. Catalysis* **1990**, *122*, 178.

(62) Rothenberger, G.; Moser, J.; Grätzel, M.; Serpone, N.; Sharma, D. K. *J. Am. Chem. Soc.* **1985**, *107*, 8054.

(63) Boxall, C.; Kelsall, G. H. *J. Chem. Soc. Faraday Trans.* **1991**, *87*, 3547.

(64) Kölle, U.; Moser, J.; Grätzel, M. *Inorg. Chem.* **1985**, *24*, 2253.

(65) Howe, R. F.; Grätzel, M. *J. Phys. Chem.* **1985**, *89*, 4495.

(66) Lawless, D.; Serpone, N.; Meisel, D. *J. Phys. Chem.* **1991**, *95*, 5166.

(67) Micic, O. I.; Zhang, Y.; Cromack, K. R.; Trifunac, A. D.; Thurnauer, M. C. *J. Phys. Chem.* **1993**, *97*, 7277.

(68) Henglein, A. *Ber. Bunsenges. Phys. Chem.* **1982**, *86*, 241.

(69) Bahnemann, D.; Henglein, A.; Spanhel, L. *Faraday Discuss. Chem. Soc.* **1984**, *78*, 151.

(70) Grätzel, M.; Howe, R. F. *J. Phys. Chem.* **1990**, *94*, 2566.

(71) Pierret, R. F. *Semiconductor Fundamentals;* Second ed.; Addison-Wesley Publishing Company: New York, 1989; Vol. I.

Sample	Surface Area ($m^2\ g^{-1}$)	Quantum† Efficiency	Relative Charge-Carrier Concentration (@100 ns) (mV)	Interfacial Electron Transfer Rate Constant (ms^{-1})
P7	85	0.25%	0.60	0.12
P13	90	0.24%	1.28	0.06
P17	380	0.07%	0.12	n/a
P18	230	0.26%	0.52	0.16
P21	280	0.44%	0.52	0.34
P24	30	0.04%	0.16	n/a
P25-B	50	0.39%	0.92	0.13

†$[HCCl_3] = 3.2$ mM, $[TiO_2] = 0.5\ g\ L^{-1}$, $I = 214\ \mu Ein\ min^{-1}$, $\lambda = 320 \pm 5$ nm, air equilibrated, pH 4-6

Table 1: TRMC results and photoreactivity data of commercial samples of TiO_2.

Substrate	Concentration	Measurement	Φ_{Q-TiO_2}	Φ_{P25-A}
Chloroform*	63 mM	[Cl⁻]	0.4%	1.6%
Dichloroacetic acid*	4.8 mM	[Cl⁻]	1.1%	23.9%
Carbon Tetrachloride*,†	5.1 mM	[Cl⁻]	0.4%	3.1%
Pentachlorophenol*	60 μM	[PCP]	0.3%	0.4%
4-Chlorophenol‡	100 μM	[4-CP]	0.4%	1.8%

*100 μEin l^{-1} min^{-1}, 310 nm < λ < 330 nm, pH 2.5-3 (HNO_3), 1 g/L TiO_2

†0.1 M MeOH

‡ 1000 μEin l^{-1} min^{-1}, λ > 320 nm, pH 3 (HNO_3), 1 g/L TiO_2

Table 2: Quantum efficiencies of Q-TiO_2 and P25-A towards photomineralization of chlorinated compounds.

Sample	Relative Charge-Carrier Concentration (@100 ns) (mV)	Interfacial Electron Transfer Rate Constant (ms^{-1})
Q-TiO_2	3.1	0.052
Fe(III)-doped Q-TiO_2	1.0	0.078
P25-A (No NO_3^-)	4.0	0.056
P25-A (NO_3^-)	2.9	0.065

Table 3: TRMC results for Q-TiO_2, Fe(III)-doped Q-TiO_2, P25-A (No NO_3^-), and P25-A (NO_3^-).

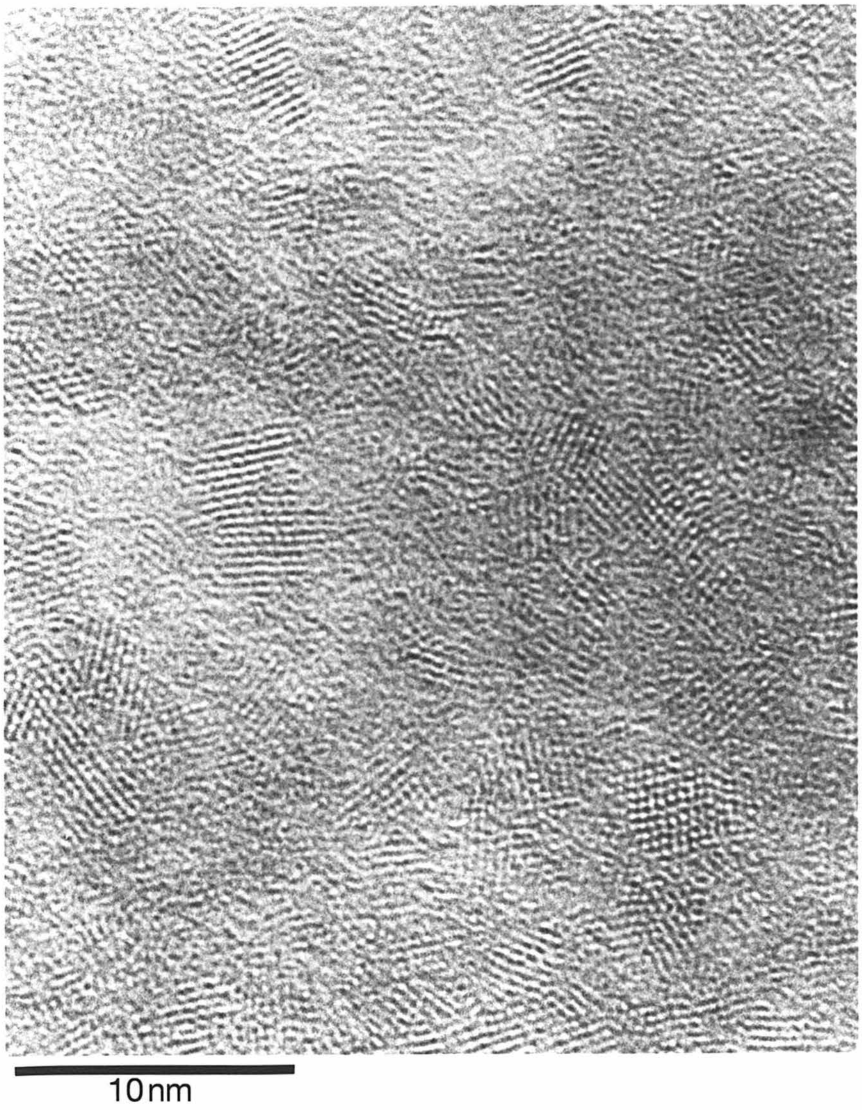

Figure 1: Transmission electron micrograph of quantum-sized TiO_2.

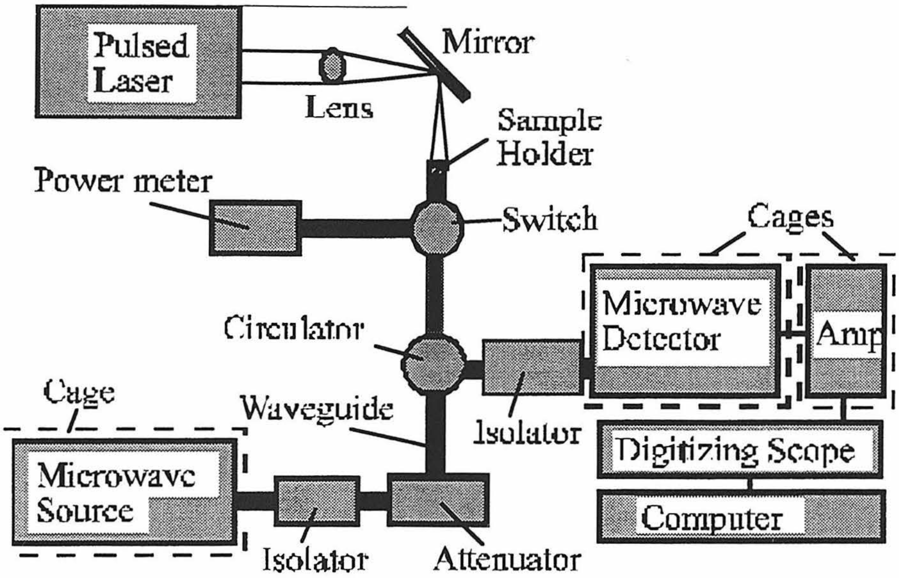

Figure 2: Schematic diagram of the apparatus for TRMC measurements.

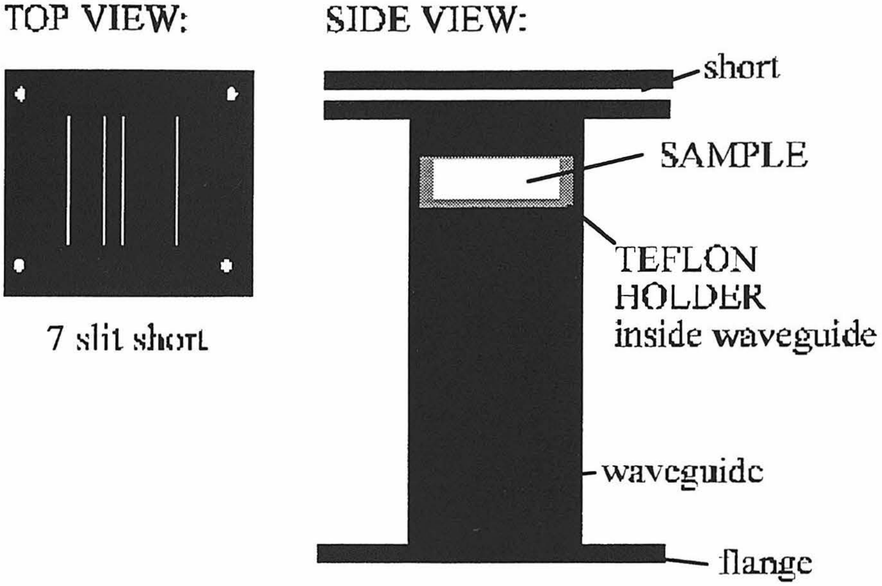

Figure 3: Sample holder for powdered semiconductor.

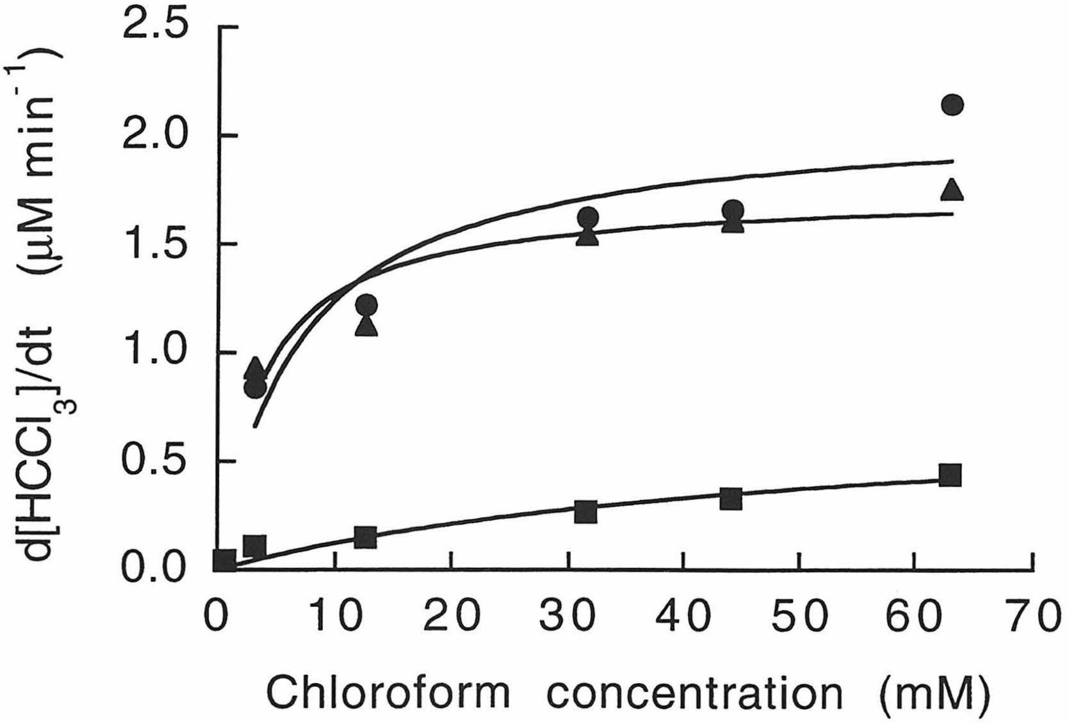

Figure 4: Degradation rate of chloroform as a function of concentration. ▲ P25-A. ■ Q-TiO$_2$. ● Fe(III) doped (1%) Q-TiO$_2$. Conditions: pH = 2.8 (HNO$_3$), [TiO$_2$] = 0.5 g/L, I = 110 µM min^{-1} (λ = 320 ± 5 nm), air equilibrated.

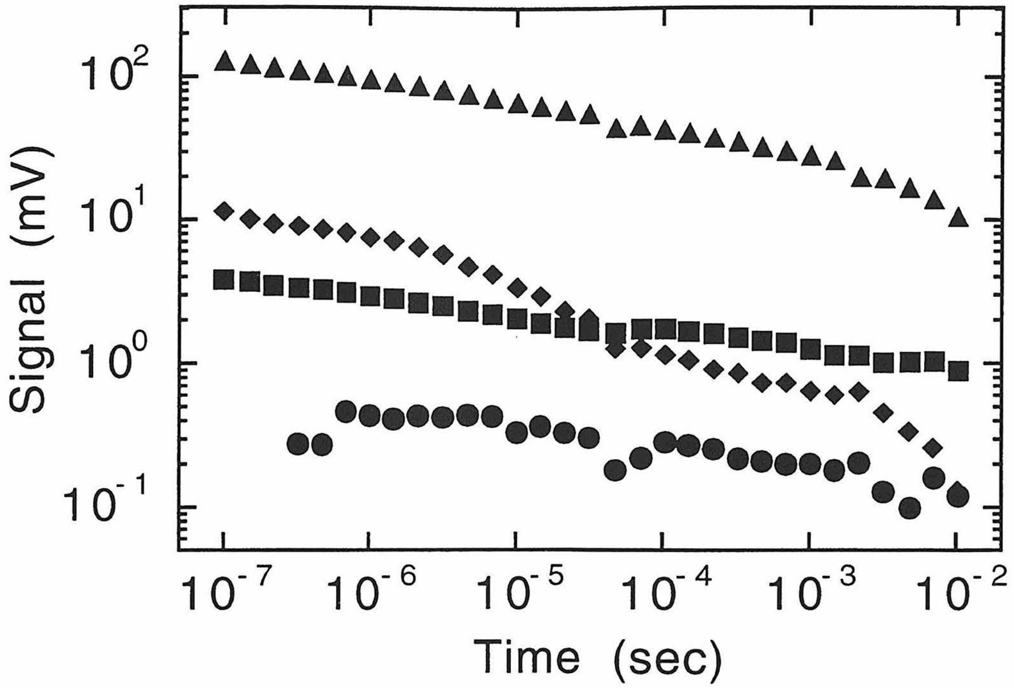

Figure 5: Double log plot of time-resolved microwave conductivity decay of several powdered semiconductors supported in transdecalin. ▲ ZnO. ◆ CdS. ■ P25-A. ● Al_2O_3.

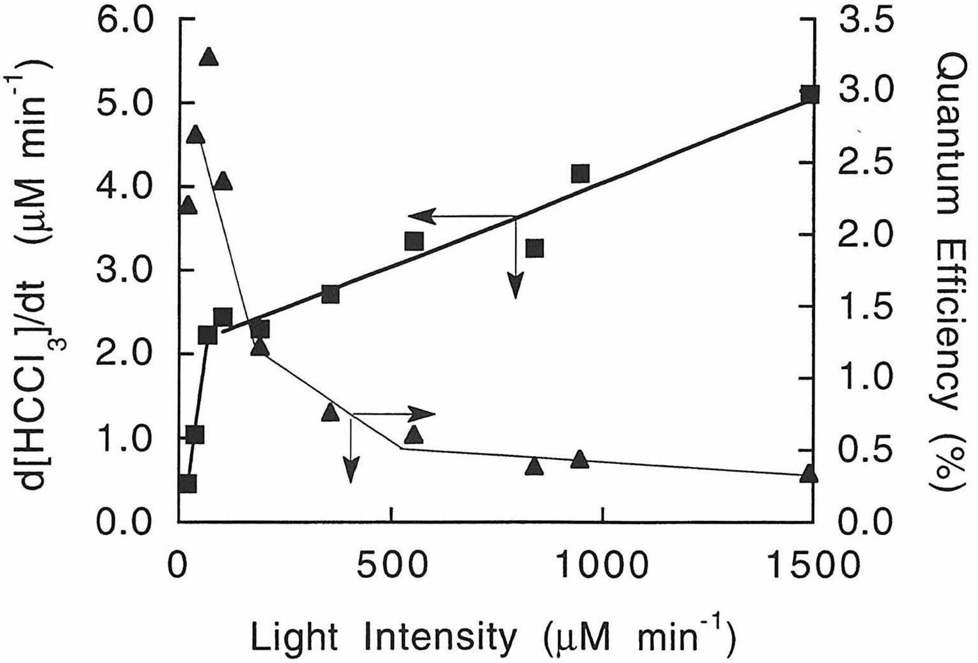

Figure 6: Degradation rate of chloroform as a function of light intensity. Conditions: pH = 11 (NaOH), 0.5 g/L P25-A, 320 < λ < 380 nm, air equilibrated.

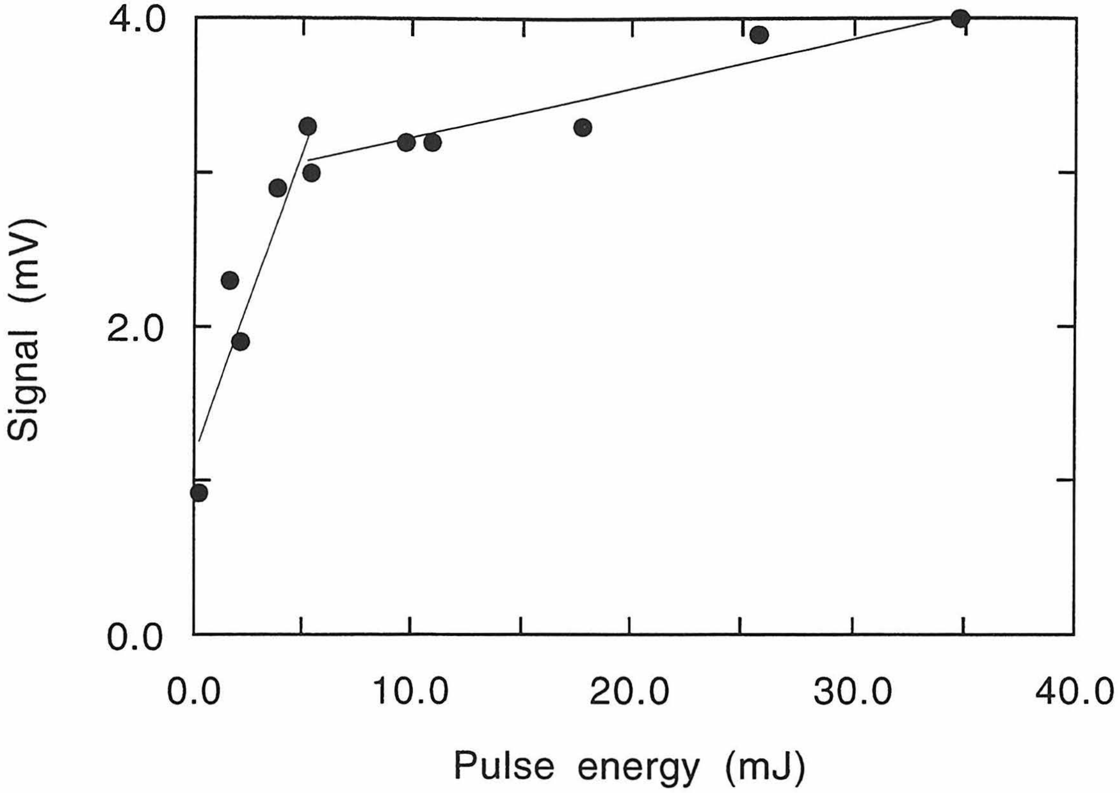

Figure 7: Effect of the incident laser pulse energy on the initial (● 100 ns) conductivity of P25-A prepared in HNO_3 and transdecalin.

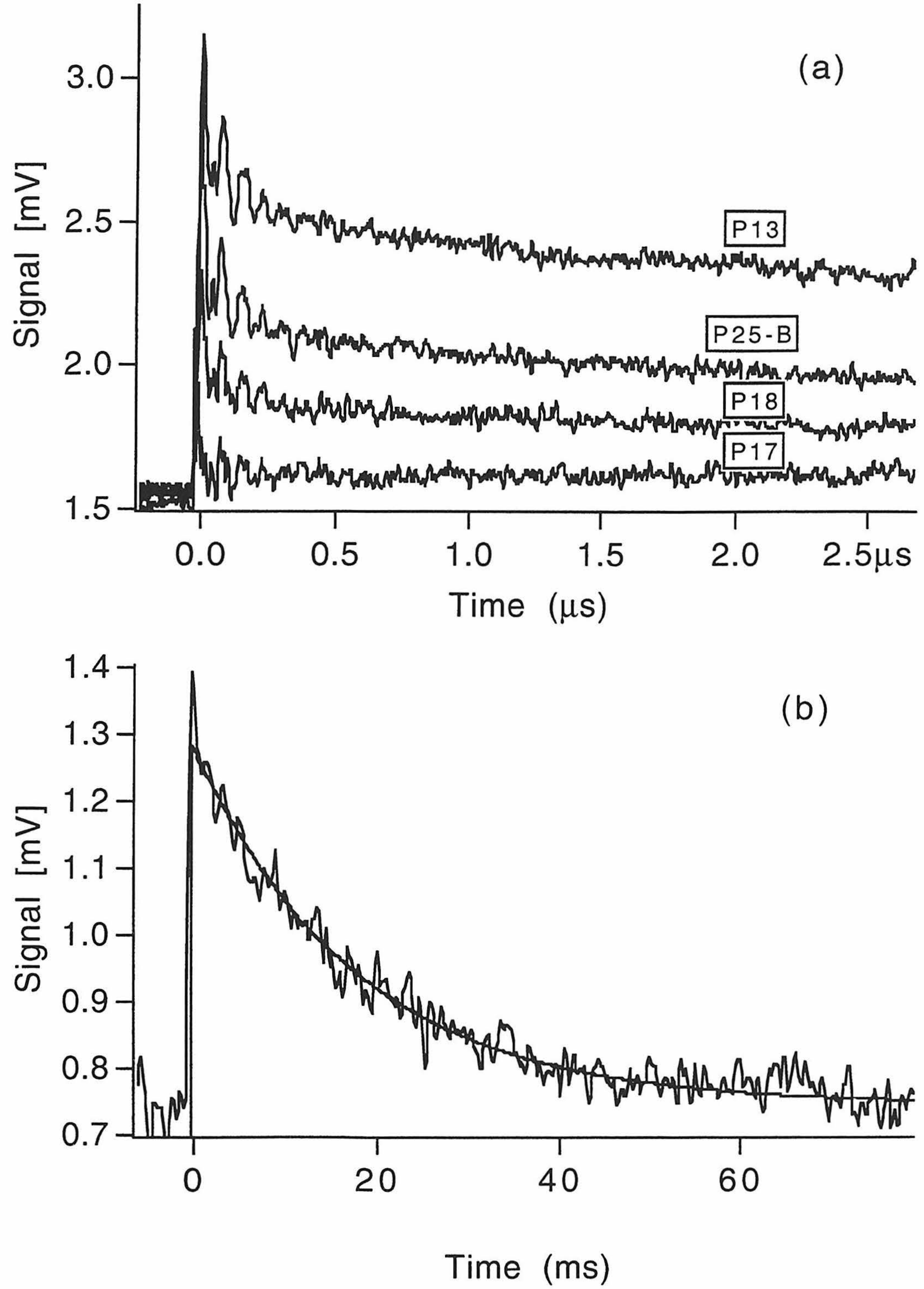

Figure 8: Representative conductivity decays of Sachtleben and Degussa TiO_2 powders. (a) P13, P25-B, P18, and P17, 2 μs/div. (b) Exponential fit of conductivity decay for P13, k = 0.056 ms^{-1}, 10 ms/div.

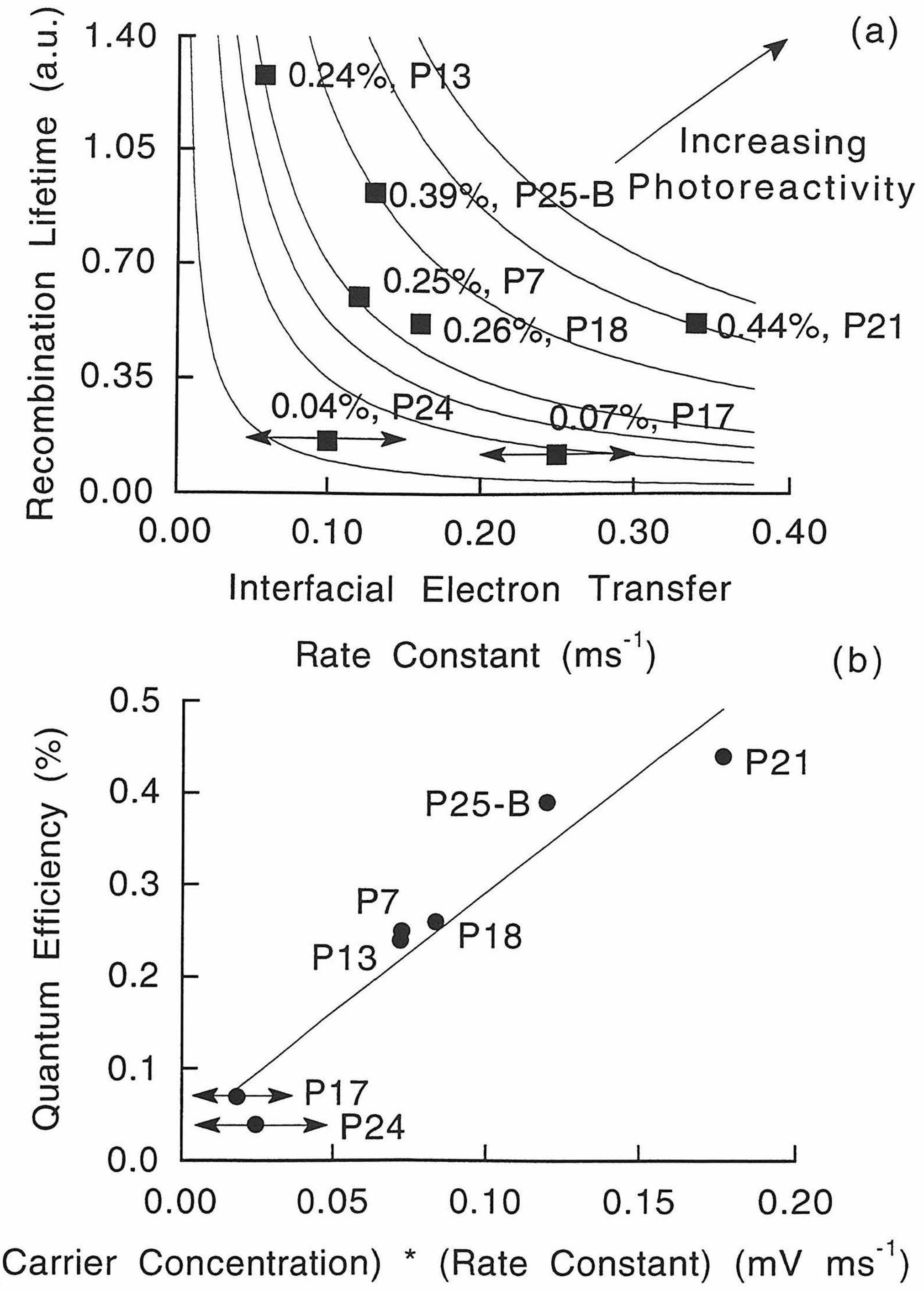

Figure 9: (a) Contour plot of quantum efficiency as a function of recombination lifetime (cf. explanation in main text) and interfacial electron-transfer rate constant. (b) Linear transformation of contour plot.

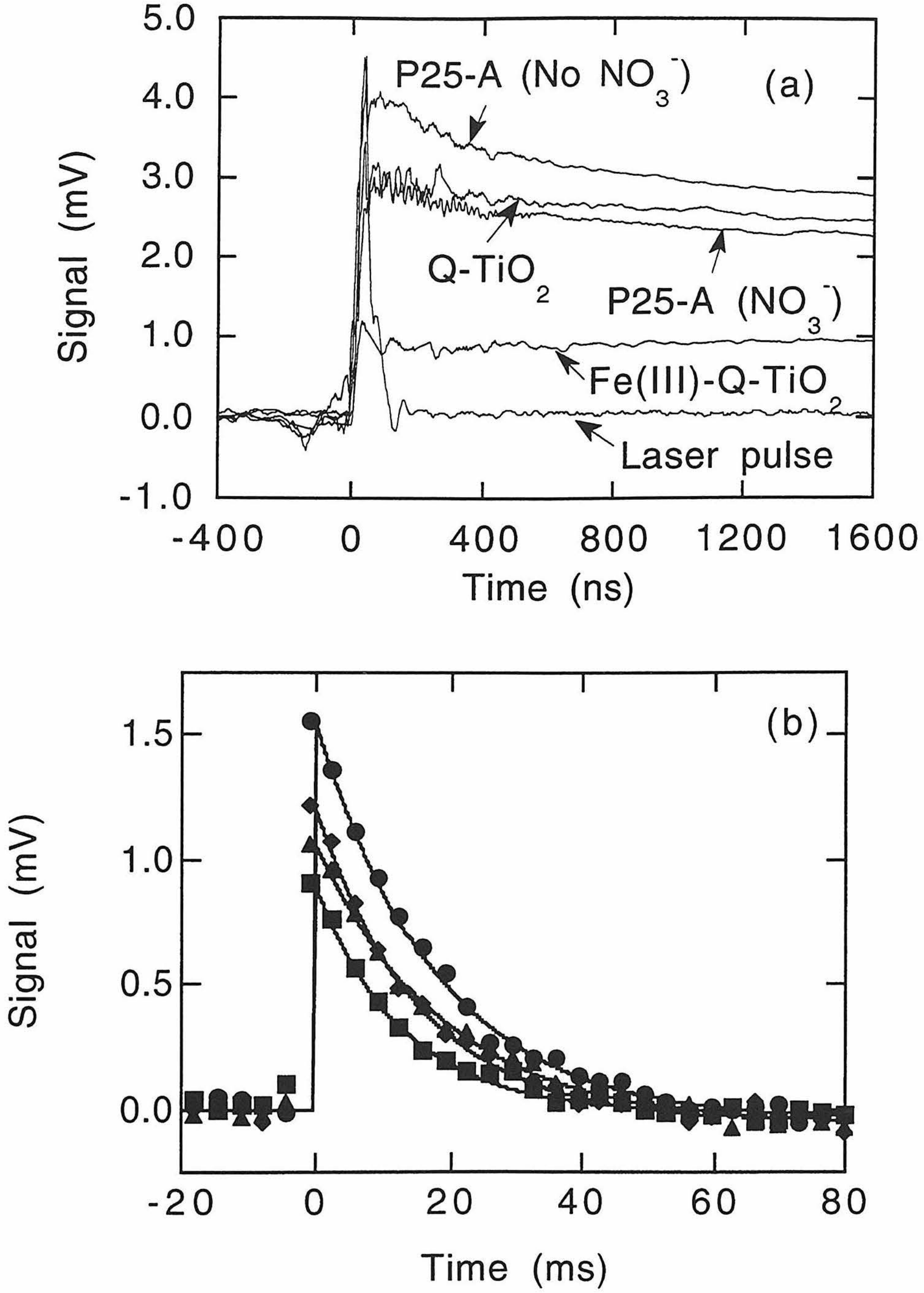

Figure 10: Conductivity decays of P25-A (F), Q-TiO_2 (H), and Fe(III)-doped Q-TiO_2 (B). Samples prepared by rotary evaporation from HNO_3 (pH 1.5) and supported in transdecalin except for P25-A-No NO_3^- (J), which was prepared without HNO_3. (a) 200 ns/div timebase. (b) 10 ms/div timebase.

Chapter 3

Time-Resolved Microwave Conductivity (TRMC): Quantum-Sized TiO_2 and the Effect of Adsorbates and Light Intensity on Charge-carrier Dynamics

[The text of this chapter appeared in Martin, S.T., Herrmann, H., and Hoffmann, M.R., *Royal Society of Chemistry, Faraday Transactions*, **1994**, *90*, 3323.]

Abstract

Charge-carrier recombination dynamics after a pulsed laser excitation are investigated by time-resolved microwave conductivity (TRMC) for quantum-sized ("Q-") TiO_2 and P25, a bulk-phase TiO_2. Adsorbed scavengers such as HNO_3, HCl, $HClO_4$, 2-propanol, *trans*-decahydronapthalene, tetranitromethane, and methyl viologen dichloride result in different charge-carrier recombination dynamics for Q-TiO_2 and P25. The differences include a current doubling with 2-propanol for which electron injection into Q-TiO_2 is much slower than into P25 and relaxation of the selection rules of an indirect-bandgap semiconductor due to size-quantization. However, the faster interfacial charge transfer predicted for Q-TiO_2 due to a 0.2 eV gain in redox overpotentials is not observed. The effect of light intensity is also investigated. Above a critical injection level, fast recombination channels are opened, which may be a major factor resulting in the dependence of the steady-state photolysis quantum yields on $I^{-1/2}$. The fast recombination channels are opened at lower injection levels for P25 than for Q-TiO_2, and a model incorporating the heterogeneity of surface-hole traps is presented.

Introduction

When the radius of a colloidal semiconductor particle falls below the exciton radius (1 to 10 nm), size-quantization effects appear.[1-6] Colloidal TiO_2 can be prepared in the size-quantized regime by sol-gel synthesis methods.[7-9] Over the last several years, we have been investigating the feasability of using size-quantized TiO_2 as a strategy to improve the quantum efficiencies of redox transformations.[10-14] In particular, ultra bandgap illumination ($\lambda < 388$ nm) of a suspension of TiO_2 particles results in the stoichiometric oxidation of many chlorinated hydrocarbons to CO_2 and HCl.[15-20] A generalized photoelectrochemical mechanism involving the major processes can be written as follows:[21-24]

photogeneration:

$$TiO_2 + h\nu \rightarrow e^- + h^+ \tag{1}$$

carrier trapping:

$$>Ti^{4+}-O^{2-}H + e^- \leftrightarrow >Ti^{3+}-O^{2-}H \tag{2}$$

$$>Ti^{4+}-O^{2-}H + h^+ \rightarrow >Ti^{4+}-O^{\cdot -}H \tag{3}$$

recombination:

$$e^- + >Ti^{4+}-O^{\cdot -}H \rightarrow >Ti^{4+}-O^{2-}H \tag{4}$$

substrate oxidation:

$$>Ti^{4+}-O^{\cdot -}H + R \rightarrow >Ti^{4+}-O^{2-}H + R^{\cdot +} \tag{5}$$

substrate hydroxylation:

$$>Ti^{4+}-O^{\cdot -}H + R \rightarrow >Ti^{4+} + {}^{\cdot +}RO^{2-}H \tag{6}$$

$$>Ti^{4+} + H^+O^{2-}H \rightarrow >Ti^{4+}-O^{2-}H + H^+ \tag{7}$$

electron deactivation:

$$>Ti^{3+}-O^{2-}H + O_2 \rightarrow >Ti^{4+}-O^{2-}H + O_2^{\cdot -} \tag{8}$$

$$O_2^{\cdot -} + H^+ \rightarrow HO_2^{\cdot} \tag{9}$$

Critical steps of the photoelectrochemical mechanism of eqs 1-9 have been investigated by the transient absorption spectra obtained following laser flash photolysis of transparent colloidal TiO_2.[24-31] Most investigators have assumed that conclusions reached regarding colloidal TiO_2 are applicable to larger bulk-phase TiO_2 particles. In the present study, the basis of this assumption is investigated by using time-resolved microwave conductivity (TRMC) measurements, which do not discriminate by crystallite size,[10,32-39] to compare the photoelectrochemical mechanisms of quantum-sized ("Q-") TiO_2 and bulk-phase TiO_2 (Degussa P25).[17-20,40-63] We have recently reported that the relative steady-state quantum efficiencies obtained with these two different forms of TiO_2 depend upon the specific reaction mechanisms involving the electron donors (e.g., direct hole transfer or hydroxyl radical attack).[10] Flash photolysis/TRMC experiments are used to compare the charge-carrier dynamics of Q-TiO_2 and P25 TiO_2 as functions of the acid used in the sol-gel synthesis, of the charge-carrier scavengers present at the particle interfaces, and of light intensity.

Experimental Section

Preparation and Characterization. Powders of Q-sized TiO_2 particles were synthesized by the controlled hydrolysis of titanium (IV) tetraisopropoxide in the presence of HCl, HNO_3, or $HClO_4$ according to procedures described previously.[7,10] The sol-gel suspension from $HClO_4$ was neutralized with NaOH to pH 3.0 in order to obtain a powder. A powder containing methyl viologen (MV) dichloride hydrate (Aldrich) was obtained by rotary evaporation of a resuspension of TiO_2-HNO_3 mixed with MV. Dry powders of P25 were obtained by the rotary evaporation of suspensions (1.44 g/L, pH 1.5) in HNO_3, HCl, $HClO_4$, or MV. P25 and Q-TiO_2 were supported with several drops of transdecalin except for the preparations containing isopropanol and tetranitromethane, which were prepared at the time of measurement by adding several drops to the powders.

The Q-TiO_2 particles were characterized as described previously.[10] HRTEM lattice spacing images and XRD Scherrer line broadening showed the size distribution of the particles was between 2 and 4 nm. The ED and XRD patterns of the TiO_2 particles were characteristic of anatase. A blue shift of the absorption onset to 345 nm (3.6 eV) was observed. The absorption coefficient at 308 nm was 2.9×10^4 cm^{-1}. Degussa P25 particles, which were composed of 30 nm crystallites consisting of 80% anatase and 20% rutile, aggregrated to form 1 µm particles.[41,42]

EPR Measurements. An E-line Century X-band Spectrometer (Varian, Palo Alto, CA) was used to record the first-derivative EPR spectra at 77 K. $CuSO_4$ was used as a calibration standard. The TiO_2 samples were prepared as gels (~10 g/L) for the EPR analysis.

TRMC Measurements. The TRMC apparatus is described in the previous paper in this series.[10] In a typical TRMC experiment separated charge-carriers, which are generated by a laser pulse, lead to a perturbation of the initial microwave absorbance. The temporal decay of the conductivity signal (i.e., microwave absorbance) reflects the lifetime of the photogenerated carriers and is given by the following equation

$$\frac{d\sigma}{dt} = \mu_{e^-_{c.b.}} \frac{d[e^-_{c.b.}]}{dt} + \mu_{e^-_T} \frac{d[e^-_T]}{dt} + \mu_{h^+_{v.b.}} \frac{d[h^+_{v.b.}]}{dt} + \mu_{h^+_T} \frac{d[h^+_T]}{dt} \qquad (10)$$

where σ is the conductivity, e_T^- is a trapped electron, h_T^+ is a trapped hole, $e_{c.b.}^-$ is a conduction-band electron, and $h_{v.b.}^+$ is a valence-band hole. The hole terms in eq 10 are negligible on the timescales of Figures 1-4 due to fast hole trapping at immobile surficial hydroxyl groups.[10] In this case, the conductivity is due to the two electron terms in eq 13, and the conductivity decay corresponds to the recombination (eq 4) or emission of electrons to substrate (eqs 11-14).

Interfacial electron transfer from the conduction-band:

substrate reduction: $e^- + Ox \rightarrow Ox^{\cdot -}$ (11)

short-circuit: $e^- + Red^{\cdot +} \rightarrow Red$ (12)

Interfacial electron transfer mediated by a surface trap:

substrate reduction: $>Ti^{3+}-O^{2-}H + Ox \rightarrow >Ti^{4+}-O^{2-}H + Ox^{\cdot -}$ (13)

short-circuit: $>Ti^{3+}-O^{2-}H + Red^{\cdot +} \rightarrow >Ti^{4+}-O^{2-}H + Red$ (14)

The recombination channel (eq 4) is exhausted for t » 10 ns because all of the holes have escaped the particle (eqs 5-6).[10] The conductivity decay is then due solely to interfacial electron transfer to the adsorbed substrate (eqs 11-14), and the microwave conductivity at 100 ns is due to the fraction of charge pairs that have not recombined (eq 4) or transferred immobile sites (eqs 3 & 5-14).[10]

Results

The EPR spectra of Q-TiO_2 prepared in HNO_3, $HClO_4$, or HCl are shown in Figure 1. The effects of adsorbed HNO_3, $HClO_4$, and HCl on the conductivity decays of P25 and Q-TiO_2 are shown in Figures 2 and 3 while the corresponding conductivity decays of P25 and Q-TiO_2 in the presence of transdecalin (T, *trans*-decahydronaphthalene), isopropanol (Isp), tetranitromethane (TM, $C(NO_3)_4$), and methyl viologen (MV^{2+}) are shown in Figures 4 and 5. The relative initial charge-carrier concentrations (Table 1), which are determined at 100 ns, are proportional to the conductivity signal strengths observed in Figures 2a-5a.

The time-resolved conductivity signals of P25 supported in transdecalin were found to be a function of the incident pulse energy, as shown in Figure 6. Similar results were obtained for different adsorbate systems (i.e., ClO_4^-, and Cl^- in transdecalin), as shown in Figures 7-9 in which the initial charge-carrier concentrations at 100 ns and 15 μs are plotted as functions of the laser pulse energy (i.e., the charge-carrier injection level). For P25 prepared in $NaClO_4$ and transdecalin (Figure 7) the carrier concentrations at 100 ns and 15 μs appear to have a lower rate of increase above 4 mJ for a similar increase in injection level. In the presence of $NaClO_4$ and transdecalin (Figure 8), the critical injection level for Q-TiO_2 shifts to ~10 mJ, and a second critical level at 25 mJ is also apparent. Samples of P25 prepared in HNO_3 and transdecalin (Figure 9) appear to have critical injection levels at 5 mJ and lower saturation levels than similar samples prepared in $NaClO_4$ (Figure 7).

Discussion

Charge-Carrier Recombination. The fate of the majority of photoexcited charge-carrier pairs in undoped ultrasmall particulate semiconductor particles is rapid recombination[20] since the instantaneous charge-carrier concentrations from the laser pulse are on the order of 10^{21} cm^{-3}. At these concentrations, the higher energy states of the energy-bands are populated and symmetry-allowed (i.e., direct) bandgap recombination in TiO_2 is facilitated. Fast recombination also occurs between free holes and trapped electrons (eq 4).[10,24] Both of these channels are exhausted within the time resolution of our experiment. When the residual carrier level concentration falls to 10^{18} cm^{-3}, the Fermi level is moved out of degeneracy, and the residual conductivity is picked up by our measurement system. A carrier concentration of ~10^{18} cm^{-3} should be representative of the steady-state concentrations of accumulated charge-carriers in CW photolysis experiments.[64]

Fast charge-pair recombination rates are further enhanced in size-quantized semiconductor particles due to the mixing of states that relaxes the selection rules for an indirect transition.[65-69] This latter effect of size-quantization is clearly illustrated in the data summarized in Table 1. For all sorbates (electron acceptors and electron donors) the concentration of charge-carriers is lower in Q-TiO_2 than in P25 after 100 ns. These experiments suggest that indirect-bandgap semiconductors in the Q-sized domain are less photoefficient redox catalysts due to inherently faster rates of charge-carrier recombination. This photophysical effect offsets the predicted gains associated with higher thermodynamic driving forces for interfacial electron-transfer.

Surface Structures. The EPR spectra shown in Figure 1 suggest the formation of radical species on the surface of the TiO_2 particles. The species may include >Ti(III)-Cl, >Ti(III)-ONO_2, >Ti(IV)-Cl·, and >Ti(IV)-ONO_2·. However, the radicals present in the sample constitute only 1% of the atoms, as indicated by a comparison of the integrated intensity of the EPR signals to the $CuSO_4$ standard. The observed radicals suggest that the acid anions interact with the surface of the particle and that the bulk of the anions speciate as >Ti(IV)-Cl, >Ti(IV)-ONO_2, and >Ti(IV)-$OClO_3$.

Fluctuating-Energy Level Model. The observed differences as a function of added acids (Figures 2 and 3) suggest that photogenerated charge-carriers undergo interfacial charge transfer to the acid anions on the surface of the TiO_2 particles. The kinetics of the interfacial charge transfer can be understood in terms of the fluctuating-energy model proposed by Gerischer[70]. The one-electron oxidation potentials of the acid adsorbates under standard conditions are as follows:[71]

$$Cl^- \leftrightarrow Cl^\cdot + e^-, \qquad E^\circ = -2.6\ V \tag{15}$$

$$NO_3^- \leftrightarrow NO_3^\cdot + e^-, \qquad E^\circ = -2.3\ V \tag{16}$$

$$OH^- \leftrightarrow {}^\cdot OH + e^-, \qquad E^\circ = -1.9\ V \tag{17}$$

Although the one-electron oxidation potential for perchlorate is not known, we assume that the value lies between 2.0 and 3.0 eV based upon comparison with eqs 15 and 16. The oxidation potential of the surface-bound hydroxide anion (i.e., eq 3) can be estimated also from eq 17; it has been reported to be -1.5 V.[21] Thus, the oxidation of the adsorbed acids can take place only from direct valence-band hole transfer since the $E^0_{rxn}(^{\cdot}OH/\text{acid anion})$ value < 0 (i.e., $\Delta G^0 \gg 0$).

The corresponding two-electron reduction potentials for nitrate and perchlorate are as follows:[72]

$$NO_3^- + 2e^- + 3H^+ \leftrightarrow HNO_2 + H_2O, \qquad E° = +0.9\text{ V} \quad (18)$$

$$ClO_4^- + 2e^- + 2H^+ \leftrightarrow ClO_3^- + H_2O, \qquad E° = +1.2\text{ V} \quad (19)$$

Within ±0.2 V, a conduction-band electron has a reduction potential of -0.3 V (eqs 11 & 12) and a valence-band hole has a reduction potential of 2.9 V (eq 3) at pH 0. In these calculations, we used the constraints that the conduction-band edge for TiO_2 is 0.1 to 0.2 V negative of the flatband potential and that the bandgap of anatase is 3.2 eV. The flatband potential has been determined to be -0.1 V[27] and -0.2 V[73] vs. NHE at pH 0 for colloidal TiO_2. The size-quantization effects in Q-TiO_2 increase the bandgap by 0.4 eV.[9] This increase corresponds to a shift in the reduction potential of the conduction-band electron to -0.5 V and of the valence-band hole to +3.1 eV for Q-TiO_2 at pH 0. Since Degussa P25 is predominantly anatase[41], its band edges are at -0.3 V and 2.9 V at pH 0.

The apparent reduction potentials of trapped charge-carriers are difficult to estimate. In the case of a trapped electron, Ti(III) is 0.2 to 0.5 eV negative of the conduction-band edge at zero surface charge, $E°_{cb}$, of rutile.[74-76] Using $E°_{cb} = -0.3$ V vs. NHE and $pH_{zpc} = 5.8$[77], the reduction potential of a trapped electron (eqs 8, 13, & 14) is ~-0.25 V vs. NHE. Because the trapped electron is localized, the reduction potential is the same for both Q- and P25 TiO_2. The trap is 50 mV below E_{cb} of P25, in agreement with other suggestions[35], and is 250 mV below E_{cb} of Q-TiO_2. The reduction potential of a trapped hole (eqs 6 & 7) is +1.5 V, as discussed for eq 17.

The acid anions (Cl^-, NO_3^-, and ClO_4^-) are chemisorbed to the surface of TiO_2 by ligand substitution of surficial hydroxyl groups and by electrostatic attraction at $pH < 6.8$. The one-electron oxidation potentials (eqs 15-17) indicate that the acid anions at the TiO_2 surface are thermodynamically less capable of hole capture than surficial hydroxide but may still serve as good hole traps (eq 3) due to the high overlap between the energy levels of the acid anions and the valence-band hole for $0.5 < \lambda < 1.0$ eV where λ is the reorganization energy[77,78]. Although OH^- and Cl^- cannot be further reduced, NO_3^- and ClO_4^- undergo multi-electron reductions (eqs 18 & 19) and thus may serve as effective electron traps.

Inorganic Donors and Acceptors. Interfacial charge transfers to the acid anion adsorbates occur on the picosecond and short nanosecond timescales and compete with interfacial recombination processes. This effect is clearly seen in Table 1, in which the initial charge-carrier concentrations appear to be unique for each adsorbate. In the case of HCl, the chemisorbed Cl^- anion directly scavenges valence-band holes (eq 20) within 10 ns in direct competition with surficial ^-OH (eq 3):[26]

$$>Ti^{4+}-Cl^- \quad + \quad h^+ \rightarrow \; >Ti^{4+}-Cl^\cdot \tag{20}$$

After formation, the surficial chloride radical may open a second channel for charge-carrier recombination as follows:

$$e^- \quad + \quad >Ti^{4+}-Cl^\cdot \rightarrow \; >Ti^{4+}-Cl^- \tag{21}$$

The relatively low carrier concentrations observed at 100 ns indicate that the cross-section for electron capture by a surficial chloride radical (eq 21) is greater than that for a surficial hydroxyl group (eq 4). This observation could be explained, in part, by the relative differences in electronegativity for OH^- and Cl^-.

Since nitrate and perchlorate serve as both potential electron scavengers and hole scavengers, three scenarios are possible to explain their effects: (a) >Ti(IV)-ONO_2 and >Ti(IV)-$OClO_3$ could act as fast hole scavengers, (b) they could act primarily as fast electron scavengers, or (c) they could act equally with respect to the trapping of both charge types. In case (a), fast hole trapping exhausts the reservoir of electron accepting species and the conductivity signal is proportional to the concentration of electrons. Case (b) is the opposite of case (a) (i.e., the conductivity signal is due to free holes). In case (c), electrons and holes are equally separated on the surface of the semiconductor particle while the charge-carriers remaining within the particle recombine rapidly and thus no residual conductivity is observed at 100 ns. As shown in Figure 2, case (c) does not appear to occur. Thus, preferential trapping of one carrier type as in (a) or (b) appears to take place. Although processes (a) and (b) are not directly distinguishable in our experiment, we will attempt to show that interfacial electron transfer does not occur significantly within the time resolution of the experiment (*vide infra*). In this case, the conductivity signal should be due to electrons as in (a).

The relatively high electron charge-carrier concentrations shown in Figure 3a for P25 in the presence of $HClO_4$ suggest that the cross-sections for hole capture by >Ti(IV)-$OClO_3$ or >Ti(IV)-OH are comparable while >Ti(IV)-$OClO_3\cdot$ has a lower cross-section for electron-capture than >Ti(IV)-$OH\cdot$. In the case of Q-TiO_2, the electron concentration in the presence of $HClO_4$ shows that the cross-section for electron capture by >Ti(IV)-ClO_4· increases relative to P25. The lower charge-carrier concentrations observed in the presence of HCl for P25 as compared to Q-TiO_2 indicates that valence-band hole-capture rates of >Ti(IV)-Cl (eq 20) are greater for P25 than for Q-TiO_2. In this case, more carriers are short-circuited by conduction-band electron transfer to >Ti(IV)-Cl· (eq 21) for P25 than for Q-TiO_2, and thus the residual charge-carrier concentration at 100 ns is greater for Q-TiO_2 than for P25 (Table 1).

Organic Donors and Acceptors. Tetranitromethane (TNM, $C(NO_3)_4$) and methyl viologen (MV^{2+}) are known to readily serve as electron scavengers in TiO_2 systems[7,27,31] while transdecalin (T), a saturated bicyclic hydrocarbon, and isopropanol (ISP) serve as surface hole scavengers.[7,10,79] The measured charge-carrier concentrations at 100 ns in P25 are comparable in the presence of MV^{2+}, TNM, ISP, and T. If fast interfacial electron transfer were taking place to TM and MV^{2+}, then the carrier concentrations at 100 ns would be expected to be reduced. The first half-lives for the charge-carriers in the presence of MV^{2+}, TNM, ISP, and T are 95 ns, 230 ns, 3.5 μs, and 7.9 μs, respectively. Thus, we conclude that even in the presence of fast electron acceptors, interfacial electron transfer takes place primarily at timescales ≥ 100 ns.

In the presence of electron acceptors (TNM and MV^{2+}), the conductivity decays flatten during the microsecond timescale, as shown in Figures 4b-c and 5b-c; this effect suggests that electron transfer does not take place during this timescale. Electron transfer to TNM and MV^{2+} takes place during the first 500 ns, as shown in Figures 4a and 5a. After that time, the surficial substrate is exhausted and further electrons do not escape the particle until fresh substrate diffuses to the surface, as shown in Figures 4d and 5d.[10]

The increasing charge-carrier concentrations seen in Figures 5a and 5b suggest that back electron injection from isopropanol into Q-TiO_2 takes place. The current-doubling effect occurs when a one-electron oxidant such as isopropanol produces a radical that can inject an electron into the conduction-band of TiO_2 as follows:[7]

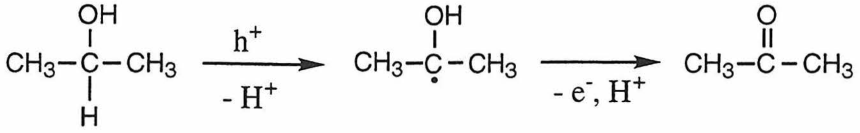

$$CH_3-\overset{OH}{\underset{H}{C}}-CH_3 \xrightarrow[-H^+]{h^+} CH_3-\overset{OH}{\underset{\bullet}{C}}-CH_3 \xrightarrow[-e^-,\,H^+]{} CH_3-\overset{O}{\overset{\|}{C}}-CH_3 \qquad (22)$$

This effect is absent in Figures 4a and 4b for P25. However, the highest initial conductivity signal for P25 is observed when isopropanol is the electron donor, which supports the argument that back electron injection takes place much more quickly than in Q-TiO_2. A slower rate for Q-TiO_2 may be due to the 0.2 eV shift to the negative of the conduction-band edge of Q-TiO_2, which should slow electron injection. Slower electron injection rates into Q-TiO_2 may also arise from a drop in the electron-transfer probability due to a higher surface density of hydroxyl groups that sterically hinder surficial Ti(IV), which is the likely site for electron injection into the conduction-band. The sol-gel preparation method is expected to result in higher surface densities of hydroxyl groups for Q-TiO_2 than for P25, which is prepared by flame hydrolysis.

Light Intensity Effects. The observed decay rates from 100 ns to 35 μs (Figure 6) follow apparent first-order kinetics; this observation implies that the charge-carriers act independently of one another at $t \leq 35$ μs. However, the charge-carrier concentrations at 100 ns are not directly proportional to the initial charge-carrier injection levels because fast recombination is a second-order process. The observed carrier concentrations at 100 ns give us a measure of the extent of charge-carrier recombination at t ≤ 100 ns.

The charge-carrier injection level can be determined from the number of photons injected into the penetration depth of Q-TiO_2 at 308 nm:

$$I(\mathrm{cm}^{-3}) = 2.3 \times 10^{17} \frac{I(\mathrm{mJ})\ \alpha(\mathrm{cm}^{-1})}{h\nu(\mathrm{eV})\ A(\mathrm{mm}^{2})} \tag{23}$$

where $I(\mathrm{cm}^{-3})$ is the injection level, I(mJ) is the pulse energy, α is the absorption coefficient, A is the cross-sectional area, and $h\nu$ is the photon energy. In our flash-photolysis system, a 4.5 mJ pulse results in $\sim 10^{21}$ carriers/cm^3.

The slopes of the lines in Figures 7-9 can be defined as *response factors*. The "response factor" is the relative change in the carrier concentration at a time, t, produced by a change in the injection level. In the absence of higher order (i.e., fast) recombination processes, the response factor should be high while the response factor is zero at *saturation*. The injection level at which the response factor changes is defined as *cross-over threshold*. These thresholds (Table 2) are the injection levels at which new higher order deactivation channels are opened and they appear as discontinuities in the lines in Figures 7-9.

The response factors in Table 2 decrease as the injection level increases, which indicates that higher injection levels result in larger quantum yields for fast recombination. In a typical CW experiment, higher light intensities are expected to raise the quantum yields for fast recombination and, thus, to reduce the net quantum yields for substrate oxidation and reduction. This conclusion provides evidence for our hypothesis that the quantum efficiencies for oxidation and reduction in CW photolysis falls as the square-root of absorbed light intensity ($\Phi \propto I^{-1/2}$) due to rapid recombination at higher light intensities.[53]

The apparent discontinuities at the cross-over thresholds in Figures 7-9 may be explained in terms of a mechanism involving two chemically distinct hole trapping sites, S_1 and S_2, in TiO_2 that have hole-trapping cross-sections labelled σ_1 and σ_2.[21] S_1 is most likely $OH_s^\cdot$ formed on a surficial Ti(IV) site and S_2 is $OH_s^\cdot$ formed on a surficial μ-O site. We propose that $\sigma_1 \gg \sigma_2$ due to a potentially unfavorable charge balance on μ-O. The concentrations of S_1 and S_2 following an injection level of $[S_0]$ are subject to the following constraints:

$$[S_1](0) = \begin{cases} [S_0], \ [S_0] < S_1 \\ S_1, \ [S_0] \geq S_1 \end{cases} \qquad [S_2](0) = \begin{cases} 0, \ [S_0] \leq S_1 \\ [S_0] - S_1, \ [S_0] > S_1 \end{cases} \tag{24}$$

where $[S_1]$ and $[S_2]$ are the concentration of occupied hole traps. At the time of injection, $[S_1](0) + [S_2](0) = [S_0]$. Due to stoichiometric annihilation, $[C](t) = [S_1](t) + [S_2](t)$ for $t \ll \tau_{\text{i.h.t.}}$ where $\tau_{\text{i.h.t.}}$ is the time for interfacial hole transfer and $[C](t)$ is the concentration of electrons.

The time-dependent decay of $[S_1]$ and $[S_2]$ may be modeled as follows:

$$[C](t) = [S_1](0) \exp(-k_1 t) + [S_2](0) \exp(-k_2 t) \tag{25}$$

$$[C](100 \text{ ns}) = m_1 [S_1](0) + m_2 [S_2](0) \tag{26}$$

where $k_{1,2}$ are the cross-sections for charge-carrier recombination (eq 4) and the response factors, $m_{1,2}$, are $\exp(-k_{1,2}(100 \text{ ns}))$. A plot of the conductivity signal [C](100 ns) versus the injection level, $[S_0]$, under the conditions set out in eq 24 results in two straight lines with a discontinuity at the cross-over threshold where $[S_0] = S_1$.

The higher surface area and surface hydroxylation of Q-TiO_2 results in a cross-over thresholds at injection level 5-10 times higher than P25, as shown in Table 1. The effect of HNO_3 and $HClO_4$ on the surface states of Degussa P25 is shown by the difference in cross-over thresholds and response factors. Saturation of the response factor for HNO_3 indicates that k_2 is fast. Q-TiO_2 has a second cross-over threshold, which indicates a third possible site for trapped holes.

Conclusions. We have shown that the charge-carrier dynamics of Q-TiO_2 and P25 respond differently with respect to added electron donors and acceptors and to absorbed light intensity. These effects suggest significant differences in the photoelectrochemical mechanisms for Q-TiO_2 and P25. Anions such as Cl^- affect the charge-carrier recombination processes by introducing surface states through specific adsorption as follows:

$$>\text{Ti-OH} + Cl^- + H^+ \rightarrow >\text{Ti}-Cl + H_2O \qquad (27)$$

Hence, the photoreactivity of Q-TiO_2 could be enhanced by deactivation of fast surficial recombination processes.

Wide bandgap quantum-sized semiconductors such as ZnO and TiO_2 should be moving further into the Marcus inverted region[80,81] with respect to the net driving force for oxidation. However, when quantum efficiencies are limited by the rate of reduction, size-quantization has been shown to yield high quantum yields for H_2O_2 production on ZnO[11] or alkene reduction on

TiO_2[82]. In the case of pollutant oxidation on TiO_2, quantum efficiencies may be limited primarily by the effective rate of interfacial reduction.[83,84] However, the mixing of states in the size-quantization regime appears to enhance direct electron-hole pair recombination in indirect-bandgap semiconductors (i.e., TiO_2). In the size-quantization regime of TiO_2, faster electron-hole pair recombination may offset the increased driving force for interfacial reduction.

Acknowledgment. We are indebted to Prof. Nathan S. Lewis for the loan of microwave components and to Prof. Geoffrey A. Blake for the use of the excimer laser. We are grateful to ARPA and ONR {NAV 5 HFMN N0001492J1901} for financial support. S. Martin is supported by a National Defense Science and Engineering Graduate Fellowship. H. Hermann wishes to thank NATO/DAAD for financing a research visit at the California Institute of Technology. Wonyong Choi, Dr. Amy Hoffman, Nicole Peill, and Dr. Andreas Termin provided valuable support and stimulating discussion.

References

(1) Bahnemann, D. W. *Isr. J. Chem.* **1993**, *33*, 115.

(2) Bawendi, M. G.; Steigerwald, M. L.; Brus, L. E. *Annu. Rev. Phys. Chem.* **1990**, *41*, 477.

(3) Brus, L. *Appl. Phys. A.* **1991**, *53*, 465.

(4) Henglein, A. T. *Curr. Chem.* **1988**, *143*, 113.

(5) Henglein, A. *Chem. Rev.* **1989**, *89*, 1861.

(6) Steigerwald, M. L.; Brus, L. E. *Annu. Rev. Mater. Sci.* **1989**, *19*, 471.

(7) Bahnemann, D.; Henglein, A.; Lilie, J.; Spanhel, L. *J. Phys. Chem.* **1984**, *88*, 709.

(8) Livage, J.; Henry, M.; Sanchez, C. *Prog. Solid. St. Chem.* **1988**, *18*, 259.

(9) Kormann, C.; Bahnemann, D. W.; Hoffmann, M. R. *J.Phys.Chem.* **1988**, *92*, 5196.

(10) Martin, S. T.; Herrmann, H.; Choi, W.; Hoffmann, M. R. *Trans. Far. Soc.* **1994**, *submitted*,

(11) Hoffman, A. J.; Carraway, E. R.; Hoffmann, M. R. *Environ. Sci. Technol.* **1994**, *28*, 776.

(12) Hoffman, A. J.; Mills, G.; Yee, H.; Hoffmann, M. R. *J. Phys. Chem.* **1992**, *96*, 5546.

(13) Hoffman, A. J.; Yee, H.; Mills, G.; Hoffmann, M. R. *J. Phys. Chem.* **1992**, *96*, 5540.

(14) Carraway, E. R.; Hoffman, A. J.; Hoffmann, M. R. *Environ. Sci. Technol.* **1994**, *28*, 786.

(15) Bahnemann, D. W.; Bockelmann, D.; Goslich, R. In *Solar Energy Materials* Elsevier Science Publishers B.V.: North-Holland, 1991; ; pp 564.

(16) Fox, M. A.; Dulay, M. T. *Chem. Rev.* **1993**, *93*, 341.

(17) Pelizzetti, E.; Serpone, N., Eds. *Homogeneous and Heterogeneous Photocatalysis*; D. Reidel Publishing Company: Dordrecht, 1986.

(18) Schiavello, M., Ed. *Photoelectrochemistry, Photocatalysis and Photoreactors*; D. Reidel Publishing Company: Dordrecht, 1985.

(19) Schiavello, M., Ed. *Photocatalysis and Environment: Trends and Applications*; Kluwer Academica Publishers: Dordrecht, 1988.

(20) Serpone, N.; Pelizzetti, E., Eds. *Photocatalysis: Fundamentals and Applications*; John Wiley & Sons: New York, 1989.

(21) Serpone, N.; Lawless, D.; Terzian, R.; Meisel, D. In *Electrochemistry in Colloids and Dispersions*; R. A. Mackay and J. Texter, Ed.; VCH Publishers, Inc.: New York, 1992; ch. 30; Vol. ; pp 399-416.

(22) Turchi, C. S.; Ollis, D. F. *J. Catalysis* **1990**, *122*, 178.

(23) Boxall, C.; Kelsall, G. H. *J. Chem. Soc. Faraday Trans.* **1991**, *87*, 3547.

(24) Rothenberger, G.; Moser, J.; Grätzel, M.; Serpone, N.; Sharma, D. K. *J. Am. Chem. Soc.* **1985**, *107*, 8054.

(25) Duonghong, D.; Borgarello, E.; Grätzel, M. *J. Am. Chem. Soc.* **1981**, *103*, 4685.

(26) Moser, J.; Grätzel, M. *Helv. Chim. Acta.* **1982**, *65*, 1436.

(27) Duonghong, D.; Ramsden, J.; Grätzel, M. *J. Am. Chem. Soc.* **1982**, *104*, 2977.

(28) Fox, M. A.; Lindig, B.; Chen, C. C. *J. Am. Chem. Soc.* **1982**, *104*, 5828.

(29) Moser, J.; Grätzel, M.; Sharma, D. K.; Serpone, N. *Helv. Chim. Acta.* **1985**, *68*, 1686.

(30) Moser, J.; Grätzel, M.; Gallay, R. *Helvetica Chimica Acta* **1987**, *70*, 1596.

(31) Draper, R. B.; Fox, M. A. *Langmuir* **1990**, *6*, 1396.

(32) Warman, J. M.; de Haas, M. P.; Pichat, P.; Koster, T. P. M.; van der Zouwen-Assink, E. A.; Mackor, A.; Cooper, R. *Radiat. Phys. Chem.* **1991**, *37*, 433.

(33) Warman, J. M.; de Haas, M. P.; Pichat, P.; Serpone, N. *J. Phys. Chem.* **1991**, *95*, 8858.

(34) Warman, J. M.; de Haas, M. P.; Grätzel, M.; Infelta, P. P. *Nature* **1984**, *310*, 306.

(35) Schindler, K. M.; Kunst, M. *J. Phys. Chem.* **1990**, *94*, 8222.

(36) Fessenden, R. W.; Kamat, P. V. *Chem. Phys. Lett.* **1986**, *123*, 233.

(37) Warman, J. M.; de Haas, M. P. In *Pulse Radiolysis*; Y. Tabata, Ed.; CRC Press: Boca Raton, 1991; chp. 6.

(38) Kunst, M.; Beck, G. *J. Appl. Phys.* **1986**, *60*, 3558.

(39) Infelta, P. P.; de Haas, M. P.; Warman, J. M. *Radiat. Phys. Chem.* **1977**, *10*, 353.

(40) Lepore, G.; Langford, C. H.; Víchová, J.; Vlcek, A. *J. Photochem. Photobiol. A.: Chem.* **1993**, *75*, 67.

(41) Bickley, R. I.; Gonzalez-Carreno, T.; Lees, J. S.; Palmisano, L.; Tilley, R. J. D. *J. Solid State Chem.* **1991**, *92*, 178.

(42) "Degussa Technical Bulletin No. 56," 1990.

(43) Pruden, A. L.; Ollis, D. F. *J. Catalysis* **1983**, *82*, 404.

(44) Hsiao, C. Y.; Lee, C. L.; Ollis, D. F. *J. Catalysis* **1983**, *82*, 418.

(45) Barbeni, M.; Pramauro, E.; Pelizzetti, E.; Brogarello, E.; Grätzel, M.; Serpone, N. *Nouv. J. Chemie* **1984**, *8*, 547.

(46) Ollis, D. F.; Hsiao, C. Y.; Budiman, L.; Lee, C. L. *J. Catalysis* **1984**, *88*, 89.

(47) Barbeni, M.; Pramauro, E.; Pelizzetti, E. *Chemosphere* **1985**, *14*, 195.

(48) Barbeni, M.; Pramauro, E.; Pelizzetti, E. *Chemosphere* **1986**, *15*, 1913.

(49) Matthews, R. W. *Aust. J. Chem.* **1987**, *40*, 667.

(50) Matthews, R. W. *J. Catalysis* **1988**, *111*, 264.

(51) Al-Ekabi, H.; Serpone, N.; Pelizzetti, E.; Minero, C. *Langmuir* **1989**, *5*, 250.

(52) Terzian, R.; Serpone, N.; Minero, C.; Pelizetti, E.; Hidaka, H. *J. Photochem. Photobiol. A.: Chem.* **1990**, *55*, 243.

(53) Kormann, C.; Bahnemann, D. W.; Hoffmann, M. R. *Environ. Sci. Technol.* **1991**, *25*, 494.

(54) Hidaka, H.; Nohara, K.; Zhao, J.; Serpone, N.; Pelizzetti, E. *J. Photochem. Photobiol. A: Chem.* **1992**, *64*, 247.

(55) Pramauro, E.; Vincenti, M.; Augugliaro, V.; Palmisano, L. *Environ. Sci. Technol.* **1993**, *27*, 1790.

(56) Mills, G.; Hoffmann, M. R. *Environ. Sci. Tech.* **1993**, *27*, 1681.

(57) D'Oliveira, J. C.; Al-Sayyed, G.; Pichat, P. *Environ. Sci. Technol.* **1990**, *24*, 990.

(58) Cunningham, J.; Srijaranai, S. *J. Photochem. Photobiol. A: Chem.* **1988**, *43*, 329.

(59) Al-Sayyed, G.; D'Oliveira, J. C.; Pichat, P. *J. Photochem. Photobiol. A: Chem.* **1991**, *58*, 99.

(60) Okamoto, K.; Yamamato, Y.; Tanaka, H.; Tanaka, M.; Itaya, A. *Bull. Chem. Soc. Jpn.* **1985**, *58*, 2015.

(61) Barbeni, M.; Morello, M.; Pramauro, E.; Pelizzetti, E. *Chemosphere* **1987**, *16*, 1165.

(62) Mills, A.; Morris, S.; Davies, R. *J. Photochem. Photobiol. A: Chem.* **1993**, *70*, 183.

(63) Durand, A. P. Y.; Brattan, D.; Brown, R. G. *Chemosphere* **1992**, *25*, 783.

(64) Boxall, C.; Kelsall, G. H. *J Chem. Soc. Faraday Trans.* **1991**, *87*, 3537.

(65) Johansson, K.; Cowdery, R.; O'Neil, M.; Rehm, J.; McLendon, G.; Marchetti, A.; Whitten, D. G. *Isr. J. Chem.* **1993**, *33*, 67.

(66) Rossetti, R.; Ellison, J. L.; Gibson, J. M.; Brus, L. E. *J. Chem. Phys.* **1984**, *80*, 4464.

(67) Rossetti, R.; Hull, R.; Gibson, J. M.; Brus, L. E. *J. Chem. Phys.* **1985**, *83*, 1406.

(68) Nosaka, Y.; Ohta, N.; Miyama, H. *J. Phys. Chem.* **1990**, *94*, 3752.

(69) Wilson, W. L.; Szajowski, P. F.; Brus, L. E. *Science* **1993**, *262*, 1242.

(70) Gerischer, H. In *Physical Chemistry: An Advanced Treatise*; H. Eyring, Ed.; Academic Press: London, 1970; ch. 5; Vol. IXA/Electrochemistry; pp 463.

(71) Wardman, P. *J. Phys. Chem. Ref. Data* **1989**, *18*, 1637.

(72) Bratsch, S. G. *J. Phys. Chem. Ref. Data* **1989**, *18*, 1.

(73) Redmond, G.; O'Keefe, A.; Burgess, C.; MacHale, C.; Fitzmaurice, D. *J. Phys. Chem.* **1993**, *97*, 11081.

(74) Mizushima, K.; Tanaka, M.; Iida, S. *J. Phys. Soc. Jpn.* **1972**, *32*, 1519.

(75) Mizushima, K.; Tanaka, M.; Asai, K.; Iida, K. *AIP conf. Proc.* **1973**, *18*, 1044.

(76) Mizushima, K.; Tanaka, M.; Asai, A.; Iida, S.; Goodenough, J. B. *J. Phys. Chem. Solids.* **1979**, *40*, 1129.

(77) Morrison, S. R. *Electrochemistry at Semiconductor and Oxidized Metal Electrodes*; Plenum Press: New York, 1980.

(78) Finklea, H. O. In *Semiconductor Electrodes*; H. O. Finklea, Ed.; Elsevier: New York, 1988; ; pp 52.

(79) Liu, A.; Sauer, M. C.; Trifunac, A. D. *J. Phys. Chem.* **1993**, *97*, 11265.

(80) Marcus, R. A.; Sutin, N. *Biochimica et Biophysica Acta* **1985**, *811*, 265.

(81) Marcus, R. A. *J. Phys. Chem.* **1990**, *94*, 1050.

(82) Anpo, M.; Shima, T.; Kodama, S.; Kubokawa, Y. *J. Phys. Chem.* **1987**, *91*, 4305.

(83) Gerischer, H.; Heller, A. *J. Phys. Chem.* **1991**, *95*, 5261.

(84) Gerischer, H.; Heller, A. *J. Electrochem. Soc.* **1992**, *139*, 113.

	Relative Initial Carrier Concentrations		Half-Lives					
Adsorbate	P25	Q-TiO$_2$	P25			Q-TiO$_2$		
HClO$_4$	11.2	2.1	750 ns	25 µs	1.6 ms	1.6 µs	800 µs	11 ms
HNO$_3$	3.6	3.0	8.0 µs	4.3 ms		2.8 ms	6.3 ms	
HCl	1.4	1.7	35 µs	8.7 ms		2.8 µs	110 µs	8.3 ms
Transdecalin	4.3	3.0	7.9 µs	5.9 ms		2.8 ms		
Isopropanol	6.8	1.1	3.5 µs	650 µs	8.7 ms	19 ms		
Tetranitromethane	4.3	n/a	230 ns	2.2 µs	51 µs	n/a		
Methyl viologen	5.0	0.9	95 ns	1.1 µs		13 ms		

Table 1: Relative initial carrier concentrations and conductivity decay half-lives

	Injection Level Cross-Over Threshold x 10^{-20} (cm^{-3})		Response Factor (a.u.) $= \left(\frac{\Delta\text{Carrier Concentration}}{\Delta\text{Injection Level}}\right)$	
System	100 ns	15 µs	100 ns	15 µs
P25 in $NaClO_4$ & Transdecalin	< 3.6	< 3.6	2.4	0.7
	> 3.6	> 3.6	0.6	0.2
Sol-Gel/Q-TiO_2 in $NaClO_4$ & Transdecalin	< 14	< 8.6	0.24	0.13
	< 25	< 25	0.12	0.05
	> 25	> 25	0.03	0.003
P25 in HNO_3 & Transdecalin	< 6.0	< 6.0	0.40	0.23
	> 6.0	> 6.0	0.03	0.01

Table 2: Injection level cross-over thresholds and response factors

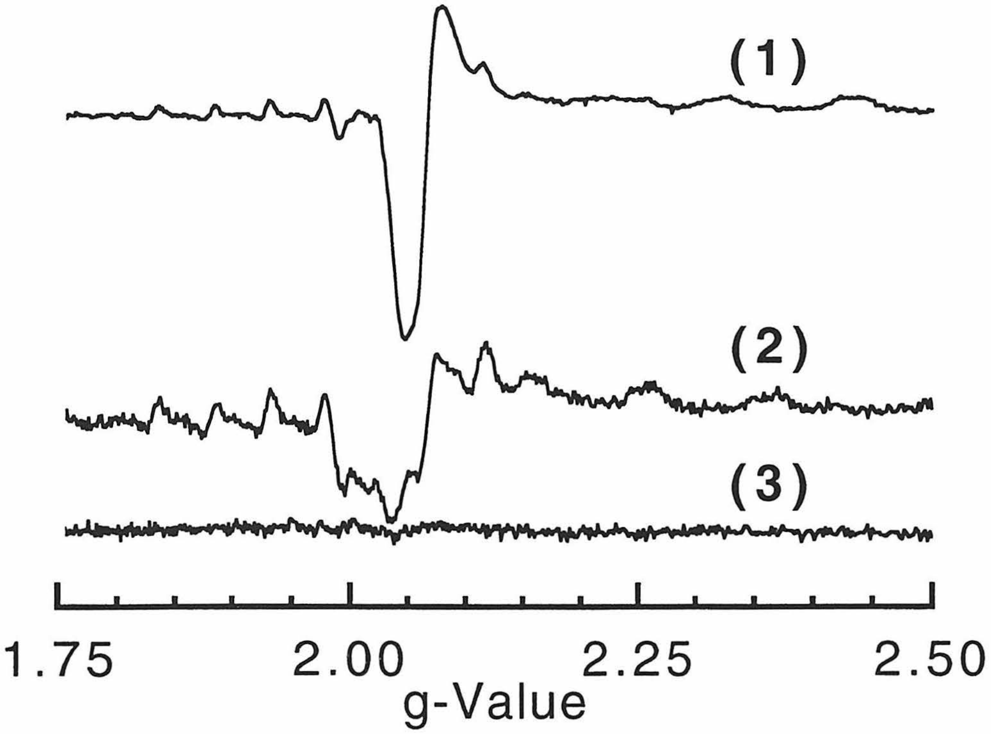

Figure 1: EPR spectra obtained at 77 K for sol-gel preparations of size-quantized TiO_2 in (1) HNO_3, (2) HCl, and (3) $HClO_4$.

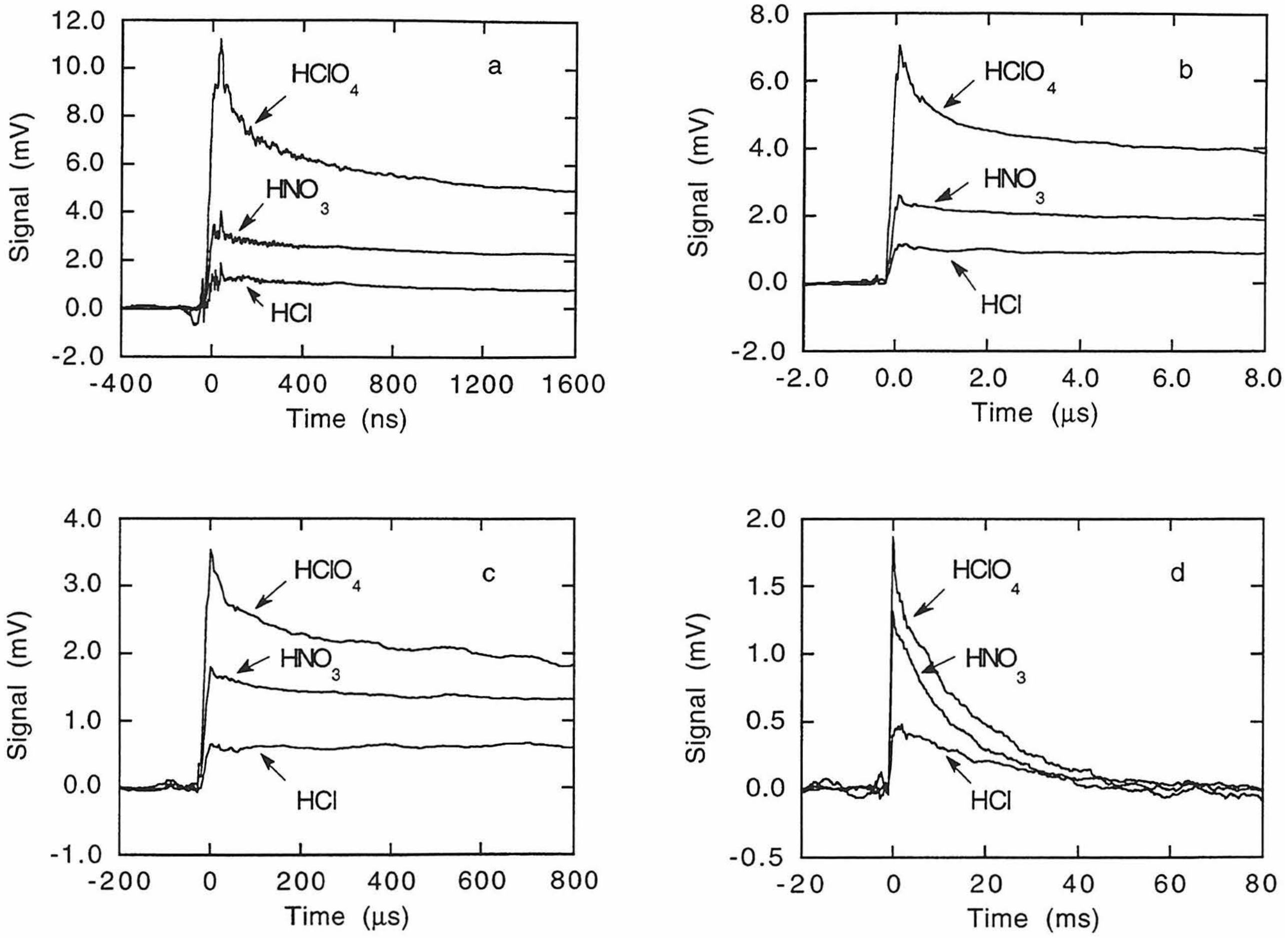

Figure 2: Effect of HNO_3, $HClO_4$, and HCl on the conductivity decays of Degussa P25 supported in transdecalin. (a) 200 ns/div timebase. (b) 2 μs/div timebase. (c) 200 μs/div timebase. (d) 10 ms/div timebase.

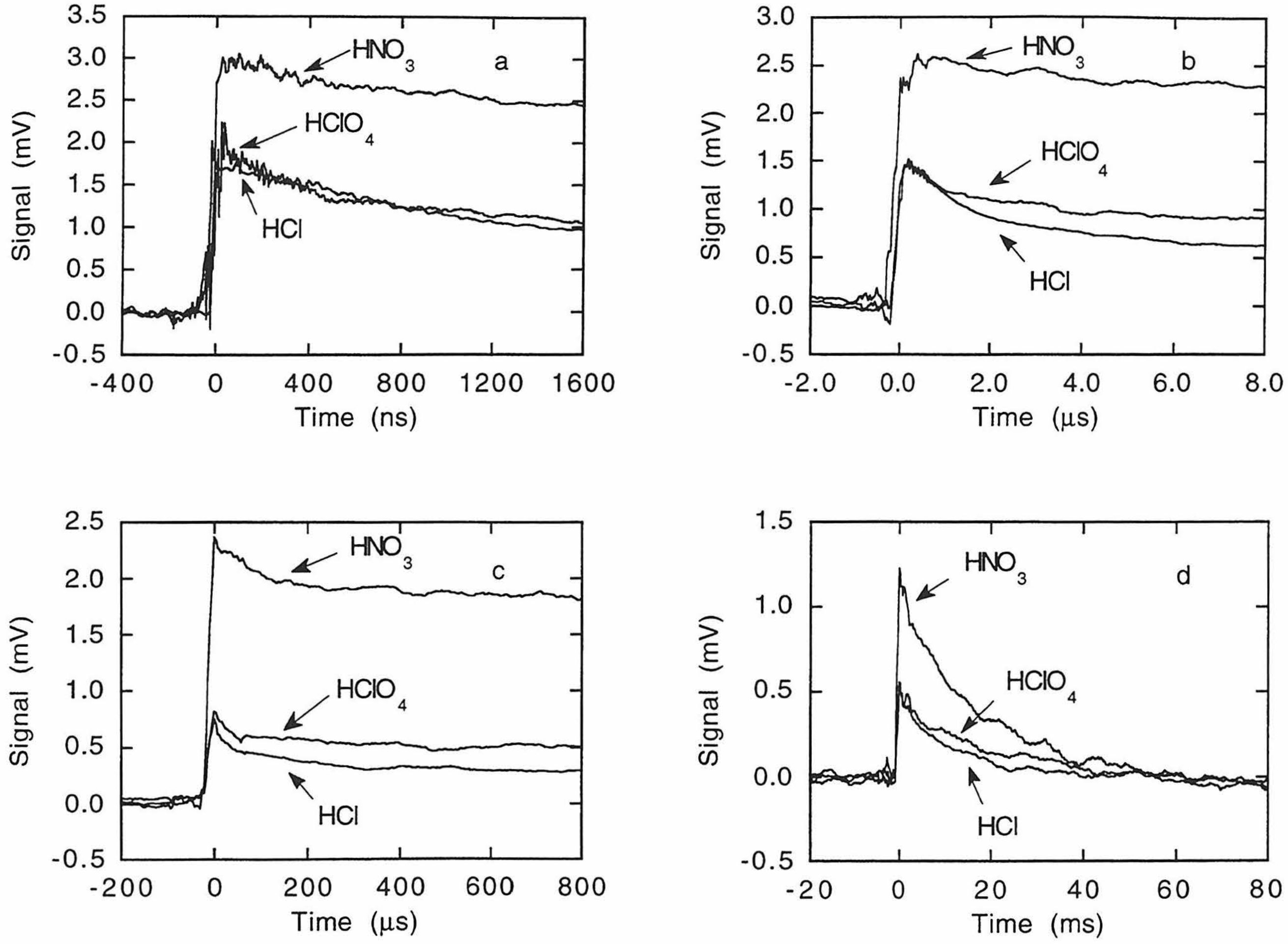

Figure 3: Effect of HNO_3, $HClO_4$, and HCl on the conductivity decays of Q-TiO_2 supported in transdecalin. (a) 200 ns/div timebase. (b) 2 μs/div timebase. (c) 200 μs/div timebase. (d) 10 ms/div timebase.

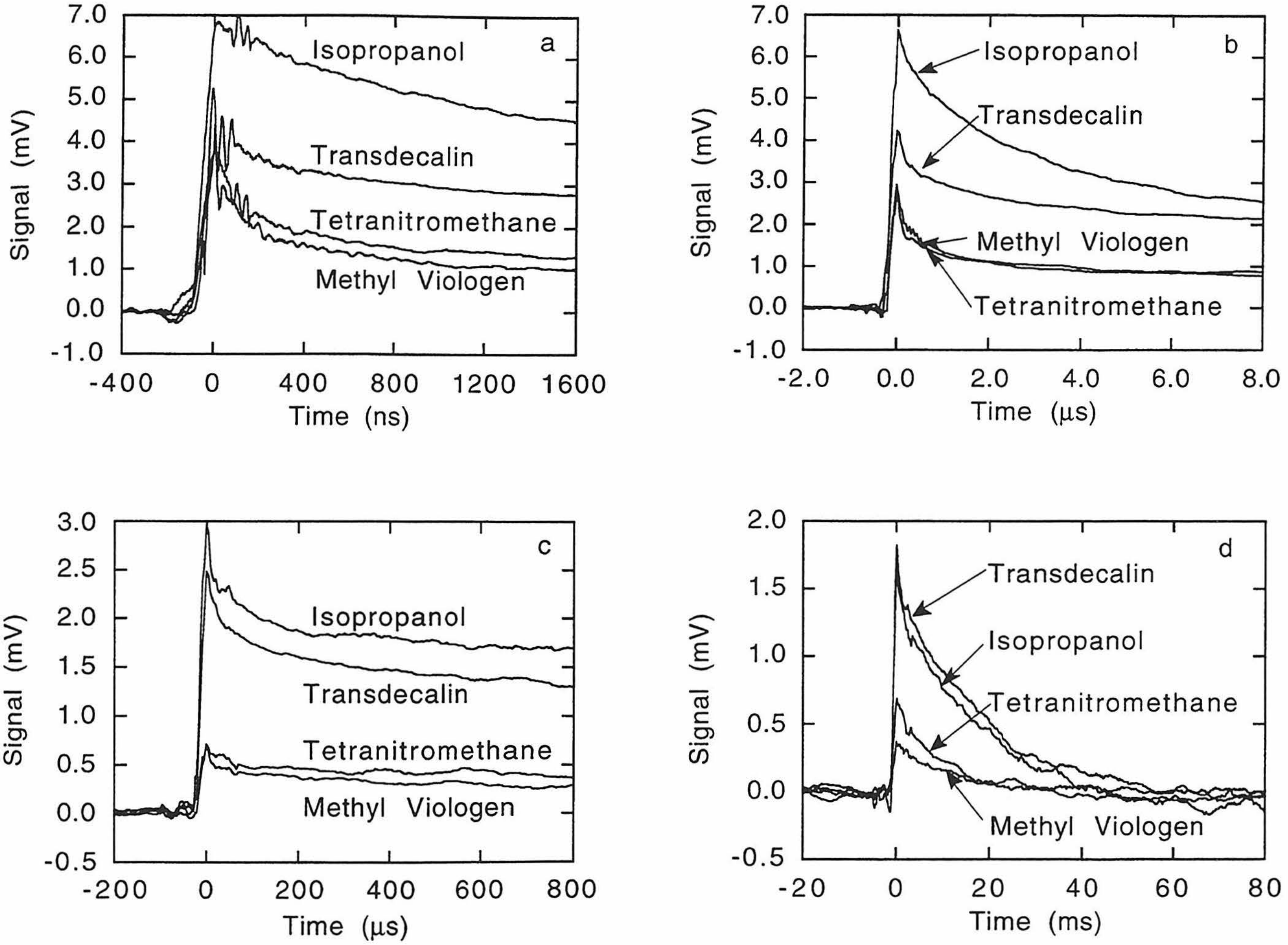

Figure 4: Effect of transdecalin, isopropanol, tetranitromethane, and methyl viologen on the conductivity decays of Degussa P25. (a) 200 ns/div timebase. (b) 2 μs/div timebase. (c) 200 μs/div timebase. (d) 10 ms/div timebase.

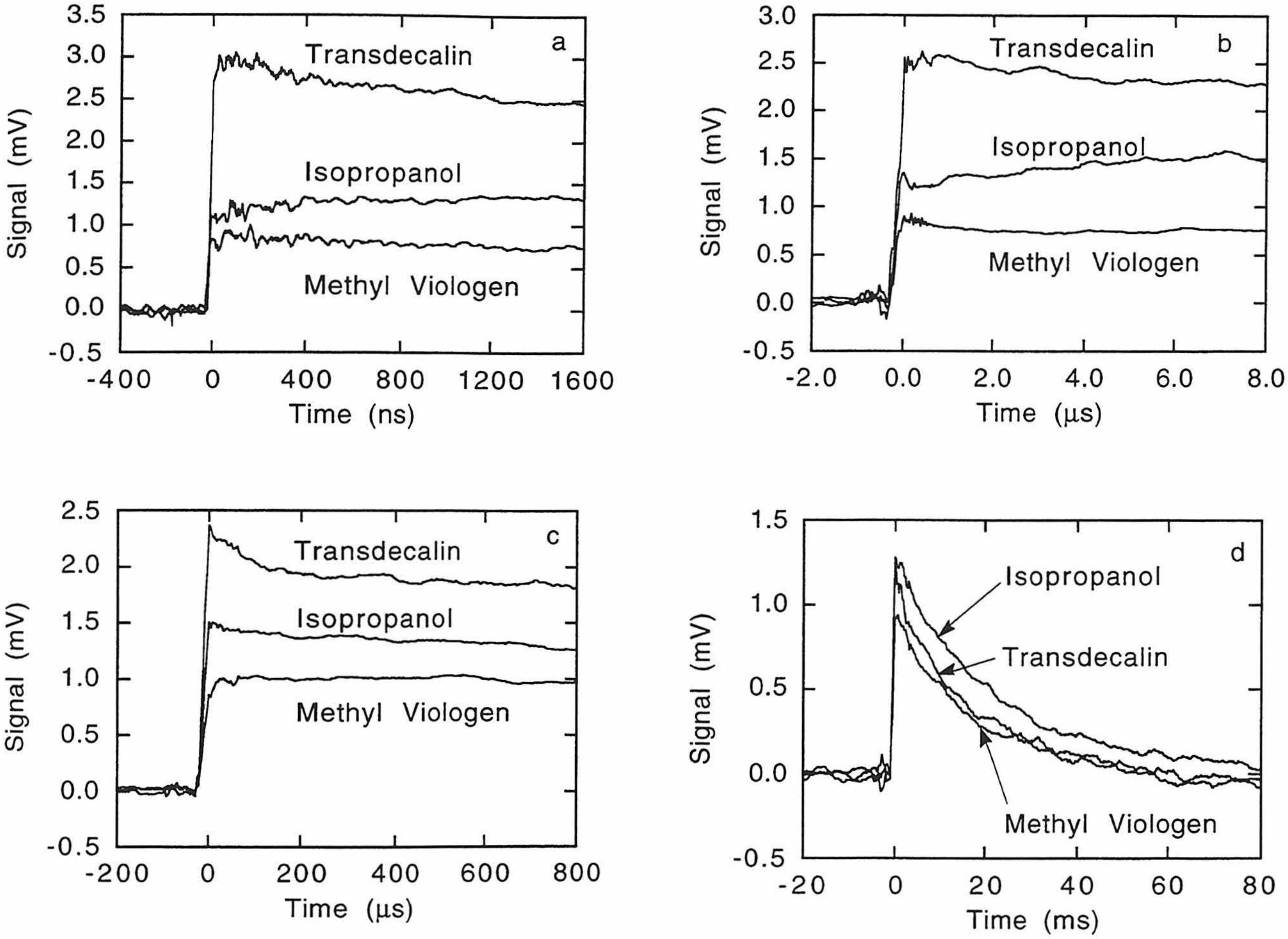

Figure 5: Effect of transdecalin, isopropanol, and methyl viologen (supported in transdecalin) on the conductivity decays of Q-TiO_2 prepared in HNO_3. (a) 200 ns/div timebase. (b) 2 μs/div timebase. (c) 200 μs/div timebase. (d) 10 ms/div timebase.

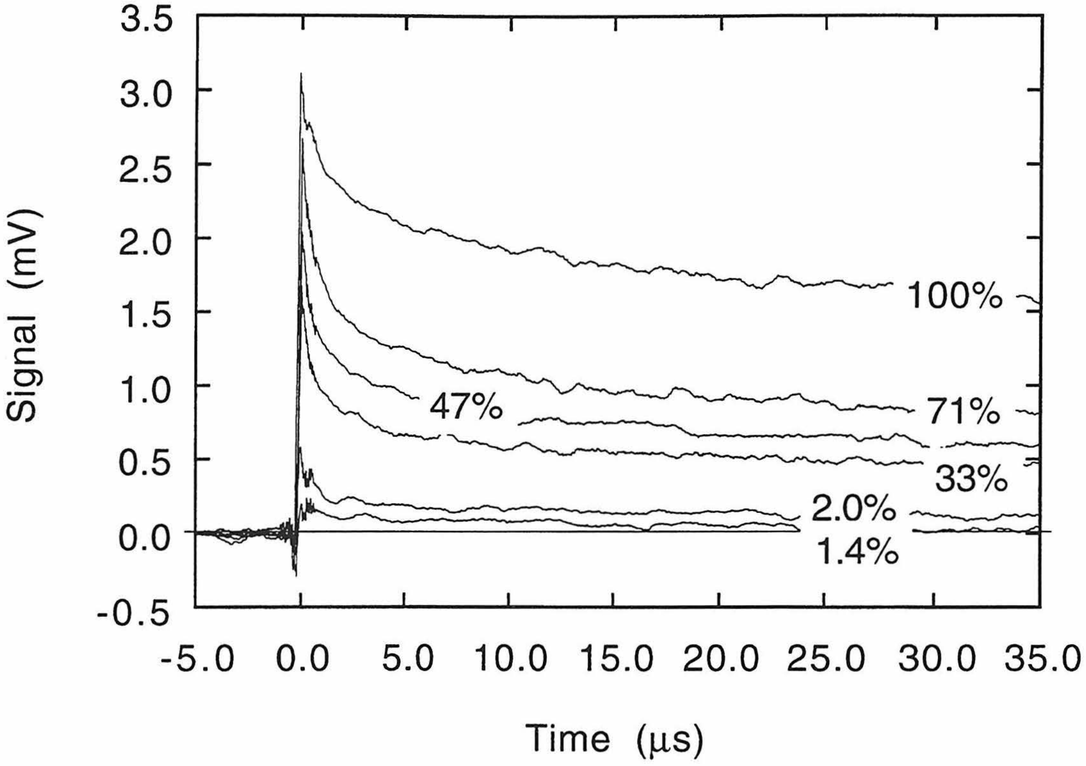

Figure 6: Effect of the incident laser pulse energy (100% = 4.9 mJ/pulse) on the conductivity decays of Degussa P25 supported in transdecalin on the 2 μs/div timebase.

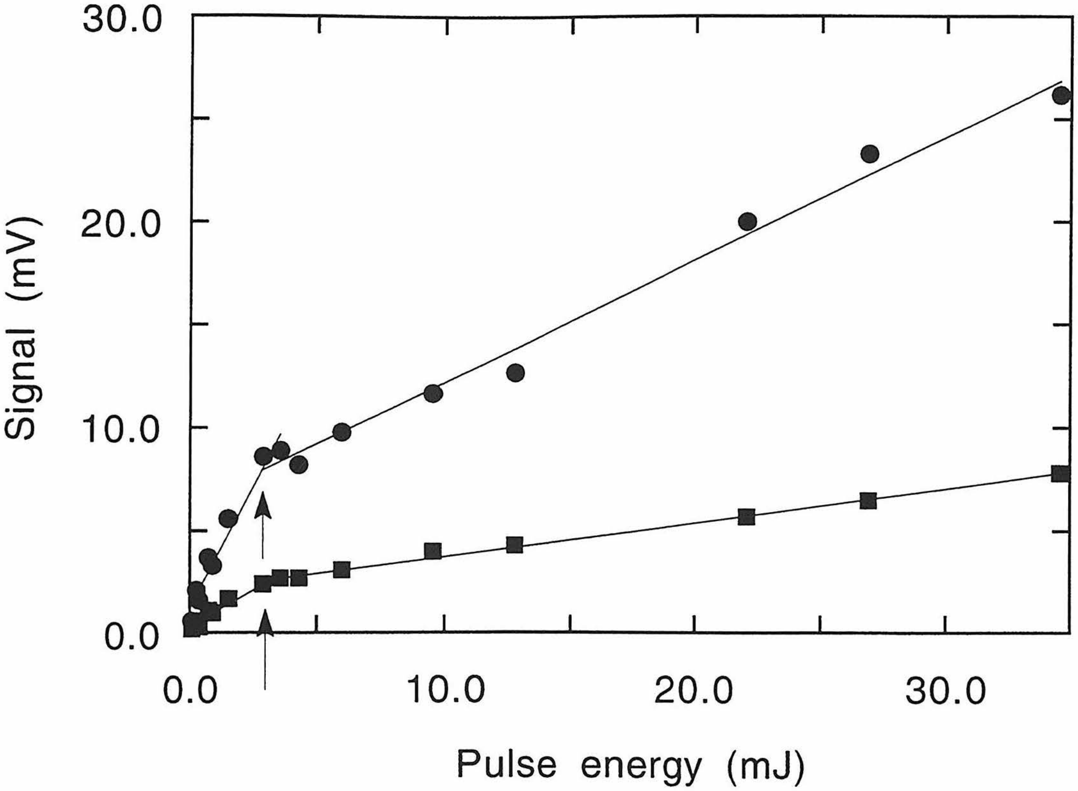

Figure 7: Effect of the incident laser pulse energy on the initial (● 100 ns) and the residual (■ 15 μs) conductivity of Degussa P25 prepared in $NaClO_4$ and transdecalin.

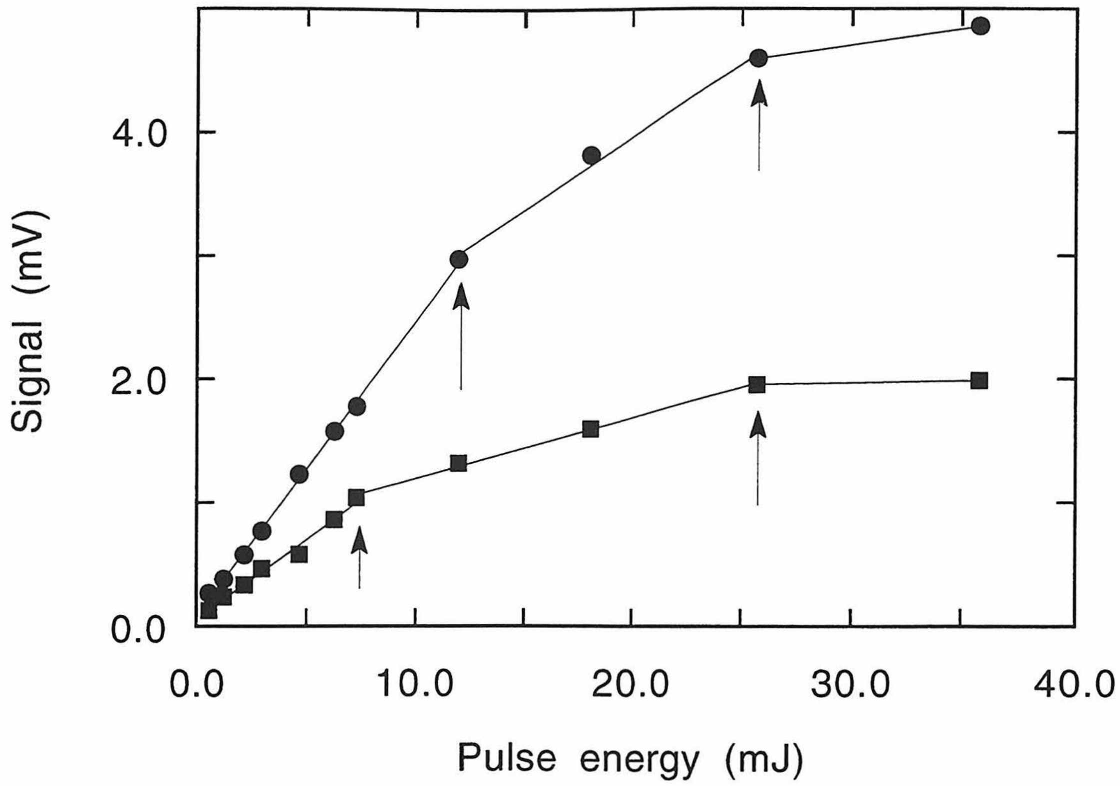

Figure 8: Effect of the incident laser pulse energy on the initial (● 100 ns) and the residual (■ 15 μs) conductivity of Q-TiO_2 prepared in $NaClO_4$ and transdecalin.

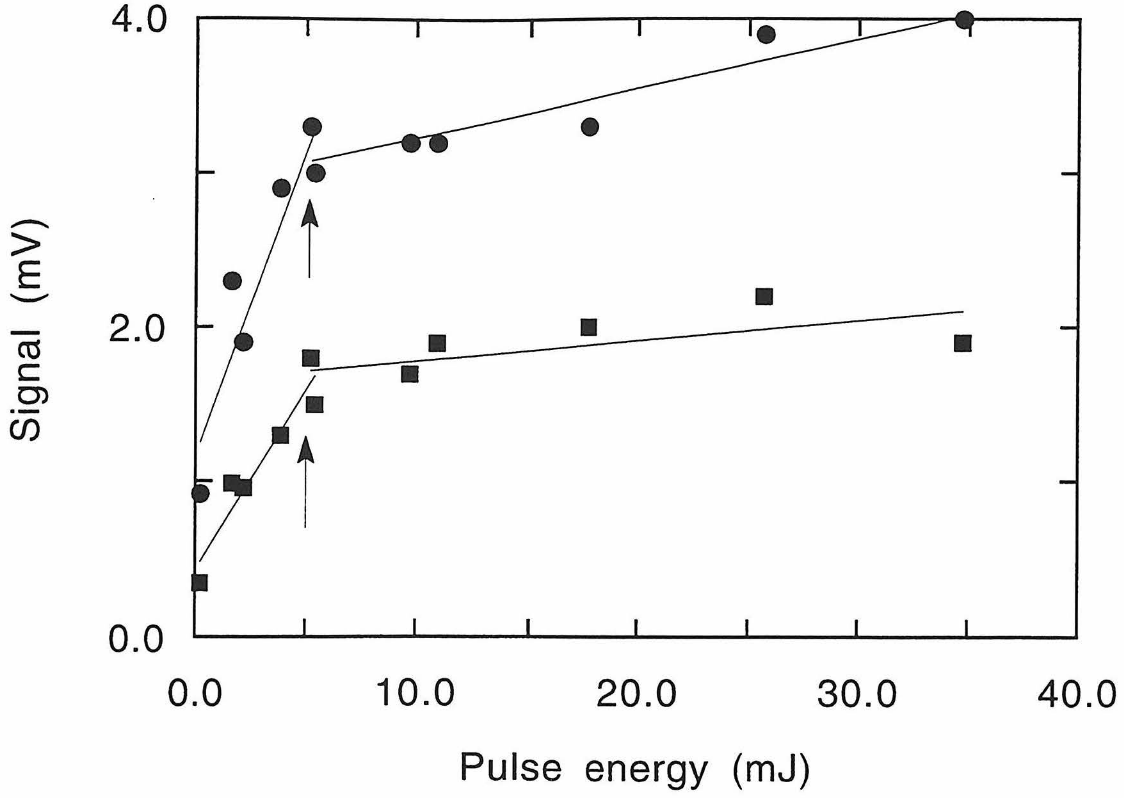

Figure 9: Effect of the incident laser pulse energy on the initial (● 100 ns) and the residual (■ 15 µs) conductivity of Degussa P25 prepared in HNO_3 and transdecalin.

Chapter 4

Time-resolved Radio-Frequency Conductivity (TRRFC) Studies of Charge-Carrier Dynamics in Aqueous Semiconductor Suspensions

[The text of this chapter has been submitted as Herrmann, H., Martin, S.T., and Hoffmann, M.R., *Journal of Physical Chemistry*, 1995.]

Abstract

The time-resolved radio-frequency conductivity (TRRFC) method provides a useful tool for *in-situ* measurements of charge carrier dynamics in aqueous suspensions of semiconductor particles. In this report, the effects of pH on surface states of ZnO and the effects of hole scavengers (isopropanol) are examined. The experimental results are interpreted in terms of surface mediated recombination processes, in which holes are trapped in a fast process by surficial sites on the ZnO. Recombination rates appear to be governed by the reaction rate of electrons with surface-trap sites. At higher pH (pH = 12) electrostatic repulsion due to a negatively-charged ZnO-surface leads to slower surface recombination rates compared to lower pH (i.e., pH = 7) conditions. Addition of a hole scavenger significantly decreases the absolute charge-carrier concentration as detected by TRRFC. This decrease is attributed to the loss of trapped surface holes or surface-bond OH due to oxidation of the hole scavenger. When isopropanol is used as a solvent, the holes react in a fast step with the solvent at the semiconductor interface within the time-resolution of the experiment. The observed TRRFC signal is then due to electrons which are thought to be predominantly transferred to dissolved oxygen (O_2) leading to the formation of hydroperoxyl radicals (HO_2) and subsequently hydrogen peroxide (H_2O_2).

Introduction

Semiconductor particles are used in a wide variety of gas and water treatment technologies.[1-4] In most of these applications, aqueous semiconductor suspensions are employed. However, the investigation of charge-carrier recombination dynamics has been limited to optical methods or time-resolved microwave conductivity (TRMC) techniques that are not easily applicable to aqueous suspensions.[5-9] Spectroscopic methods[10] are normally limited to the study of optically transparent colloidal systems[11] and cannot be applied to opaque disperse systems as often found in water treatment applications (ZnO, TiO_2-dispersions). Furthermore, the optical techniques currently available do not provide a direct time-resolved measure of conductivity due to the concentration and mobilitiy of holes and electrons generated after irradiation.

Time-resolved radio-frequency conductivity measurements (TRRFC) provide a convenient method for contactless probing of conductivity. TRRFC has been applied in the past for the study of charge carrier dynamics in semiconductors as used in solid-state electronic devices.[5,12-14] In contrast to previous studies we describe a radio frequency conductivity system that allows for the time-dependent study of charge-carrier dynamics in semiconductor particles suspended in water. Our apparatus is utilized to investigate (i) the effects of pH and (ii) the addition of a hole scavenger (isopropanol) on the charge-carrier concentrations within ZnO particles. We believe that this is the first application and report of time-resolved RF conductivity measurements of an aqueous microheterogeneous suspension.

Experimental Section

Measurement. A schematic of the TRRFC apparatus used in the present study is shown in Figure 1. An excimer laser (Lambda Physik LPX 110 iCC, $\lambda = 308$ nm, typical pulse energy of 75 mJ) irradiates the aqueous sample suspension contained in a NMR tube which is used as the sample cavity. The geometry of the tube allows 40% of the light emitted by the laser to hit the sample. The NMR-tube is centered in a 10-turn coil (length 1.4 cm, diameter 1/4" (0.635 cm), 20 gauge copper wire, inductance L = 240 nH). The frequency tuning capacitor ranges from 1-11 pF and the impedance matching capacitor ranges from 1-20 pF. The circuit has a Q-value of 40 at zero ionic strength, i.e., Millipore water, 18 MΩ. The entire unit is shielded in a massive aluminum Faraday cage housing and is connected to a radiofrequency bridge. A Wavetek RF generator (Mod. 2500-A) drives the bridge at 160 MHz and a maximum output power level of +13 dBm.

After samples are placed in the cavity, the RF bridge is tuned to maximize the inductive coupling of the RF bridge and the sample by matching the capacitors in the parallel-series tank circuit. At the resonant frequency only minimum RF power is reflected back to the directional coupler (Merrimac CR-20-500) in the RF circuit so that the detector, a double-balanced mixer (DBM, Mini-Circuits ZAY-2), produces minimum DC output. The amplitude of the DBM's DC voltage output is proportional to the power reflected from the tank circuit. It is monitored as a function of time by means of a Tektronics storage oscilloscope (Mod. 2440) and transferred to a computer. The input voltage to the tank circuit is 20 V and the maximum voltage perturbation during an experiment is 0.05%.

Dispersions of ZnO in water (1.0 g/l) were freshly prepared at pH values of 7.0, 9.5 and 12.0 by the addition of either $HClO_4$ or NaOH to the original dispersion of pH = 7.7. Lower pH's cannot be studied due to the dissolution of ZnO under acidic conditions.[2-3] pH was measured both before and after the experiments (Radiometer Copenhagen PHM 85). pH values were found to be constant within 0.1 pH units. Dispersions were vigorously shaken before each experiment to prevent settling. All chemicals used in the present study were of analytical grade and used without further purification. ZnO powder was obtained from Baker.

Theory. The DC voltage output of the DBM is sensitive to both the amplitude and the phase of the RF signal reflected back from the sample tank circuit. In principle, changes in both the real and imaginary components of the magnetic permeability ,μ, and dielectric constant, ε, of the sample circuit affect the reflected signal. The real components of the cited entities are affected by dispersive interaction, whereas the changes in the imaginary components of μ and ε are due to absorption. The sample circuit is represented by L and R_2 in the inset of Figure 2a. The microphysical phenomena of eddy currents and resistive heating change L and R_2, respectively. These various descriptions of the experiment are interconnected by the following relationships:

$$L = f(\mu',\varepsilon') \text{ --> Eddy currents} \tag{1}$$

$$R2 = f(\mu'',\varepsilon'') \text{ --> Resistive heating} \tag{2}$$

$$\mu = \mu' + i\,\mu'' \tag{3}$$

$$\varepsilon = \varepsilon' + \varepsilon'' \tag{4}$$

Further discussion of the experiment will be in terms of changes in L and R_2.

Eq 5, which describes the typical shape of a Q-well (Figure 2a), is derived for the circuit shown in the inset of Figure 2a.

$$\frac{V_{out}}{V_{in}} = \frac{\left[\alpha^2 R_1^2 \beta + \left(\alpha^2 R_2 (R_1 + R_2) + \beta\right)^2\right]^{1/2}}{\left(\alpha^2 (R_1 + R_2)^2 + \beta\right)}$$

$$\text{where } \alpha = \omega C \text{ and } \beta = \left(\omega^2 LC - 1\right)^2 \tag{5}$$

Time-dependent changes in the Q-well arising from $\Delta L(t)$ following the photogeneration and the subsequent reactions of the charge-carriers are shown in Figure 2b. The inset of Figure 2b shows the rise and subsequent decay of the voltage output of the double-balanced mixer.

The DBM DC voltage output is a function of both the amplitude of the RF signal reflected back from the serial tank circuit and the phase mismatch between the sample and reference signals as follows:[15]

$$V_{DBM} = C\, V_{Ref} V_{Out} \cos\delta \tag{6}$$

Because the phase is matched prior to laser irradiation, $\delta(0) = 0$, the change in voltage at the DBM as a function of time, $\Delta V_{DBM(t)}$, is written as follows:

$$\Delta V_{DBM}(t) = V_{DBM}(t) - V_{DBM}(0) = C\, V_{Ref}\left(V_{Out}(t)\cos\delta(t) - V_{Out}(0)\right) \tag{7}$$

using the approximation $\cos \delta \approx 1 - \frac{\delta^2}{2}$ for small δ, eq 7 can be re-written as eq 8:

$$\Delta V_{DBM}(t) = C\, V_{Ref}\left(V_{Out}(t) \left(1 - \frac{\delta^2(t)}{2} \right) - V_{Out}(0) \right) \tag{8}$$

Substitution using $\Delta V_{Out}(t) = V_{out}(t) - V_{Out}(0)$ leads to

$$\Delta V_{DBM}(t) = C\, V_{Ref}\left(-V_{Out}(0)\frac{\delta^2(t)}{2} - \Delta V_{Out}(t)\frac{\delta^2(t)}{2} + \Delta V_{Out}(t) \right) \tag{9}$$

Because the perturbations ΔV(t) and δ(t) are small, eq 9 simplifies to:

$$\Delta V_{DBM}(t) = C\, V_{Ref}\left(\Delta V_{Out}(t) - V_{Out}(0)\frac{\delta^2(t)}{2} \right) \tag{10}$$

We note that the phase mismatch yields a voltage decrease whereas the amplitude change yields a voltage increase. Hence, because a voltage increase is observed in our measurements (Figures 3-5), we conclude that the amplitude term dominates and we re-write eq 10 as follows:

$$\Delta V_{DBM}(t) = C\, V_{Ref} \Delta V_{Out}(t) \tag{11}$$

Eq 5 may be used to describe ΔV_{out} in terms of ΔL(t) and $\Delta R_2(t)$. The former term, ΔL(t) is believed to be the more important in the present experiment.

Eddy currents may be expressed as a change in the inductance of a unit volume in the center of a solenoid due to a change of the magnetic permeability of the sample:

$$\Delta L = \Delta\mu \frac{N}{2\sqrt{\left(r^2 + \frac{\lambda^2}{4}\right)}} \tag{12}$$

where L is the inductance [H], μ is the magnetic permeability [J $s^2 C^{-2} m^{-1}$], N is the number of turns of the solenoid of radius r [cm], and λ [cm] is the length of the coil.[17] Species with high mobilities within the sample (i.e., charge-carriers in the bulk semiconductor or ions in solution) will yield stronger eddy currents and hence larger changes in the inductance of the circuit. The TRRFC experiment is thus most sensitive to semiconductors with charge-carriers of high mobilities dispersed in solutions with a low ionic concentration. Ions in the sample solution produce eddy currents which shield the magnetic field and decrease the sensitivity of the apparatus for monitoring charge carrier concentrations by reducing the Q-value. The absolute value for the inductance of a solenoidal coil is calculated from eq 13 as follows:[18]

$$L = (N^2 r^2)/(23r + 25\lambda)\ [\mu H] \tag{13}$$

The resonance frequency f_0 of the tank circuit is given by

$$f_0 = 1/\ (2\pi(LC)^{1/2}) \tag{14}$$

where C is the capacity of the frequency tuning capacitor.[19]

The time resolution of the TRRFC experiment is limited by the quality (Q) factor of the coil as the response time of the circuit is given by:

$$\tau = Q/\pi f_0 = 2L/R \tag{15}$$

where the quality factor Q is given as

$$Q = \frac{1}{R}\sqrt{\frac{L}{C}} = 2\pi f_0 \frac{L}{R} = \frac{f_0}{\Delta f} \tag{16}$$

with R being the real intrinsic resistance of the tank circuit. According to eqs 15 and 16 bigger inductivities L (i.e., bigger coils) lead to an increased sensitivity of the experiment but also to an increase in response times. Various coils have been tested during the present investigations but best experimental results have been obtained using the coil with the dimensions given earlier.

In summary, the photo-induced generation of additional charge-carriers in the sample leads to the generation of eddy currents in the particles from the changing magnetic field in the coil due to the 160 MHz electric field. These currents set up counter magnetic fields which change the inductance of the coil and hence the resonance frequency of the circuit. As a result, RF power is reflected back from the sample circuit to the DBM and the DC output signal increases. As the charge carrier concentration within the sample decays as a function of time, the inductive mismatch between RF-bridge and sample decreases, the resonance frequency returns to its initial value, and the DBM produces a smaller DC voltage output. Linearity and sensitivity of the experiments are a function of the shape of the Q-well of the circuit. It is assumed for the present investigation that the changes in resonant frequency are small so that the DC output of the DBM is a direct measure for conductivity, i.e., charge carrier concentrations multiplied by their mobilities in the bulk semiconductor medium.

Results and Discussion

Effect of pH. TRRFC-traces for samples of 1 g/L ZnO suspended in water at pH = 7.0, 9.5 and 12.0 are shown in Figure 3 for the shortest timescale studied (i.e., up to t = 500 ns after the laser pulse). These unprocessed data show the biggest signals and the slowest time response for pH = 7.0 and the smallest signal with the fastest time response at pH = 12 with the data obtained at pH = 9.5 showing intermediate behaviour. This effect is caused by the relative shielding of the ions within the sample solution due to the adjustment of pH. At higher ionic concentration the quality factor of the inductive circuit gets smaller and hence causes faster response times and decreased sensitivity. The data shown in Figure 3 reflect the trends in time resolution, ion content and signal sensitivity as they are expected from the theory of eqs 10-15.

In Figure 4 the data for three longer timescales studied (i.e., 2 μs/div (top), 200 μs/div (middle) and 10 ms/div (bottom)) are shown. The data in Figure 4 have been normalized to identical maximum signal strengths in order to compensate for the effects of ion content of the samples as discussed above. To achieve normalization the signals taken at pH = 9.5 were multiplied by a factor of 1.41 and those taken at pH = 12.0 by a factor of 2.33. On the shortest timescale (Figure 4a, top) the decay kinetics for charge carrier recombination are identical within experimental error for all three pH values studied.

At the next longer timescales (Figures 4b, middle, in the time-domain between 10 μs and 1 ms after laser irridiation), charge carrier concentrations are approximately constant for the sample at pH = 12. Lower pH values lead to increased decay rates for charge-carrier concentration in this time-domain. In the experiments with the lowest time resolution applied (i.e., between 1 ms and 80ms after photoinjection as shown in Figure 4c, bottom), the decays of charge carrier concentration are significantly slower for the systems at pH = 12.0 compared to pH = 9.5 or 7.0. Higher pH of the aqueous solutions surrounding the ZnO particles leads to reduced decay rates of the semiconductor charge carriers. This effect is related to a change in the surface speciation of the ZnO particle with changing pH.

The surface of ZnO is amphoteric ($pH_{zpc} = 9.0 \pm 0.3$)[11] and can be described by the following protonation equilibria:

$$>Zn\text{-}OH_2^+ \leftrightarrow >Zn\text{-}OH + H^+ \qquad (17)$$

and

$$>Zn\text{-}OH \leftrightarrow >Zn\text{-}O^- + H^+ \qquad (18)$$

with $pK_a(17) = 7.6$ and $pK_a(18) = 11.0$.[11] The symbol ">" denotes a surficial group. At pH = 7.0, the principal surface species is $Zn\text{-}OH_2^+$, while at pH = 9.5 and pH = 12.0, Zn-OH and $Zn\text{-}O^-$ become the principal surface species, respectively.

The main charge-carrier recombination mechanism, which is proposed based on the data of Figure 3, may be described as follows:

$$>\mathrm{Zn\text{-}OH_2}^{+} + h_{VB}^{+} \rightarrow >\mathrm{Zn\text{-}OH_2}^{2+} \quad (19)$$

$$>\mathrm{Zn\text{-}OH} + h_{VB}^{+} \rightarrow >\mathrm{Zn\text{-}OH}^{+} \quad (20)$$

$$>\mathrm{Zn\text{-}O}^{-} + h_{VB}^{+} \rightarrow \mathrm{Zn\text{-}O} \quad (21)$$

Valence-band holes (h_{VB}^{+}) generated by the photoinjection process are trapped within a timescale of about 100 ns after photoinjection[20-21] by surface hydroxyl groups. Recombination of the charge carriers results from the reaction of conduction-band electrons with the hole traps of eqs 19-21 as follows:

pH = 7.0: $$>\mathrm{Zn\text{-}OH_2}^{2+} + e_{CB}^{-} \rightarrow >\mathrm{Zn\text{-}OH_2}^{+} \quad (22)$$

pH = 9.5: $$>\mathrm{Zn\text{-}OH}^{+} + e_{CB}^{-} \rightarrow >\mathrm{Zn\text{-}OH} \quad (23)$$

pH = 12.0: $$>\mathrm{Zn\text{-}O} + e_{CB}^{-} \rightarrow >\mathrm{Zn\text{-}O}^{-} \quad (24)$$

Reactions 22-24 represent the rate-limiting steps in the surface-mediated recombination process. The above mechanism is consistent with experimental findings from recent time-resolved microwave conductivity (TRMC) investigations of TiO_2 photoreactivity.[8,9]

The observed time-dependent decay of the charge-carrier concentration may be characterized kinetically based on the assumption of the above surface-mediated recombination mechanism. We quantify the initial recombination half-lives (Figure 4c) of the orders of magnitude of $\tau(\mathrm{pH} = 7.0) \approx 10 \mu s$, $\tau(\mathrm{pH} = 9.5) \approx 100\ \mu s$ and of $\tau(\mathrm{pH} = 12.0) \approx 10$ ms were determined. From these results it appears that the surface speciation of ZnO affects the efficiency of surface-mediated charge carrier recombination. Reactions 20-22 suggest that electrostatic interactions between the surface hole traps and the migrating electrons govern the efficiency of surface mediated recombination of charge carriers. Electron capture by a doubly charged $>Zn\text{-}OH_2{}^{2+}$ surface group (pH = 7.0) is accelerated by Coulombic interactions more than the corresponding reaction of a single positively charged (pH = 9.5) or a neutral surface hole trap group at pH = 12.0. Cross-sections for electron capture in semiconductors appear to be correlated with Coulombic repulsion but no quantitative data are presently available for the three species that characterize the acid-base chemistry of metal-oxide surfaces.

Effect of isopropanol. In order to study the effect of added hole scavengers on charge-carrier dynamics, 1 g/L ZnO particles were dispersed in isopropanol. The resulting TRRFC signal is shown in Figure 5 together with a reference trace obtained in 1 g/l ZnO aqueous suspension without any pH-adjustment (pH = 8.5). Figure 5 shows that the charge-carrier concentrations are significantly reduced and the temporal decay pattern is changed substantially in the presence of isopropanol. While the TRRFC signal decays in the aqueous system by about 40% in 8 μs, the signal stays nearly constant in the isopropanol system at a signal level which corresponds to about 20% of the maximum signal in the aqueous suspension. The Q-value of the TRRFC apparatus has been found to be constant so that signal strength and temporal behaviour of the signals in Figure 5 can be directly compared. The signal obtained in isopropanol is consistent with a mechanism involving a fast surface reaction of the trapped holes with the solvent (presumably within the electrical double layer surrounding the particles or actually sorbed to the particle surface):

$$>Zn\text{-}OH_2^{2+} + (CH_3)_2CHOH \rightarrow >Zn\text{-}OH^{+} + (CH_3)_2\overset{\bullet}{C}OH + H^{+} \quad (25)$$

The electron transfer of eq 25 is most likely completed within the response time of the TRRFC apparatus and thus the rise in signal observed in the isopropanol experiment at short times is due to the limited time resolution.

As shown above (eqs 20-22), the charge carriers should recombine predominantly via the reaction of surface hole traps with electrons. The relatively slow kinetics of this process in H_2O correspond to the TRRFC signal in Figure 5. From these results we conclude the TRRFC signal, which is detected on the microsecond timescale, arises from the presence of conduction-band electrons because valence-band holes are either trapped at the surface (aqueous system) or have reacted with the organic solvent (isopropanol system). The invariance of the TRRFC signal with time in the microsecond regime may be due to a back-injection of electrons from the isopropyl radical to the conduction band of ZnO:[22]

$$>\text{Zn-OH}_2^+ + (\text{CH}_3)_2\overset{\bullet}{\text{C}}\text{OH} \rightarrow >\text{Zn-OH}_2^+ + e^- (\text{c.b.}) + (\text{CH}_3)_2\text{CO} + \text{H}^+ \quad (26)$$

The smaller TRRFC signal, which is obtained in the isopropanol experiments, corresponds to a smaller residual concentration of electrons in ZnO. Efficient hole scavenging (e.g., by isopropanol) yields the accumulation of conduction-band electrons and thus a negative shift in the reduction potential due to charge repulsion.[23] This effect should accelerate the rate of interfacial charge-transfer of conduction-band electrons.[8,24-26] On longer timescales, the TRRFC signals fall to zero in both systems. When the oxidizing capacity of the holes is transferred away from the ZnO particles, electrons are likely to migrate to the ZnO surface, first, and then react with molecular oxygen, which leads to the formation of HO_2/O_2^- and subsequently hydrogen peroxide:[4,11]

$$>Zn\text{-}OH_2^+ + e^- (c.b.) \rightarrow >Zn\text{-}OH_2 \overset{O_2}{\rightarrow} >Zn\text{-}OH_2^+ + O_2^- \qquad (27)$$

followed by

$$O_2^- + H^+ \Leftrightarrow HO_2 \qquad (28)$$

and finally

$$2\,HO_2 \rightarrow H_2O_2 + O_2 \qquad (29)$$

Conclusions

The present study establishes the feasibility and potential application of TRRFC to investigate aqueous semiconductor suspensions. High pH conditions lead to extended lifetimes of charge carriers in aqueous ZnO dispersions. However, when isopropanol is used as a solvent, the charge-carrier dynamics in ZnO appear to be altered completely by the surface reactions of holes with isopropanol and the back injection of charge carriers into the ZnO conduction band from the isopropyl radical. In this system, electrons react with dissolved oxygen rather than undergoing surface-mediated recombination with trapped holes as in the case of the aqueous system. The TRRFC method provides a valuable tool for the study of semiconductor conductivity in aqueous semiconductor systems. Future work will concentrate on optimization of sensitivity as well as time-resolution of the technique along with investigations with a phase-sensitive detector which may then allow deconvolution of the absorptive and dispersive components leading to the observed TRRFC signals.

Acknowledgement

The authors are grateful for the loan of radiofrequency components from Prof. N.S. Lewis, the help of Prof D. P. Weitekamp's group (especially John Marohn) with radiofrequency components, and the use of the excimer laser by Prof. G. A. Blake. Financial support for this project is provided by the Advanced Research Project Agency (ARPA) and the Office of Naval Research (ONR) {NAV 5 HFMNN0001492J1901}. We are grateful to Drs. Ira Skurnick and Harold Guard for their generous support and encouragement. S. T. Martin is supported by a National Defense Science and Engineering Graduate Fellowship. Hartmut Herrmann wishes to thank NATO and Deutscher Akademischer Austauschdienst (DAAD) for support. We would like to thank the reviewers of this paper for their stimulating comments.

References

(1) Hoffmann, M. R., Martin, S. T., Choi, W. Y. and Bahnemann, D. W., *Chem. Rev.* **1995** , *95*, 69.

(2) *Photocatalytic Purification of Water and Air*; Ollis, D .F.; Al-Ekabi, H. Eds.; Elsevier: Amsterdam 1993.

(3) Kamat, P.V., *Chem. Rev.* **1993**, *93*, 267.

(4) Hoffman, A. J.; Carraway, E. R.; Hoffmann, M. R., *Environ. Sci. Technol*. **1994**, *28*, 776.

(5) Forbes, M. D. E.; Lewis, N. S., *J. Am. Chem. Soc* **1990**, *112*, 3682.

(6) Kunst, M.; Beck, G., *J. Appl. Phys*. **1986**, *60*, 3558.

(7) Warman, J. M.; deHaas, M. P. *Pulse Radiolysis*, 2nd ed; CRC Press: Boca Raton, 1991; Chapter 6.

(8) Martin, S. T.; Herrmann, H.; Choi, W.; Hoffmann, M. R., *J. Chem. Soc. Faraday Trans*. **1994**, *90*, 3315.

(9) Martin, S. T.; Herrmann, H.; Hoffmann, M. R., *J. Chem. Soc. Faraday Trans*. **1994**, *90*, 3323.

(10) Lantz, J.M.; Corn, R.M, *J. Phys. Chem*. **1994**, *98*, 9387.

(11) Bahnemann, D.W.; Kormann, C.; Hoffmann, M.R., *J. Phys. Chem.* **1987**, *91*, 3789.

(12) Miller, G. L.; Robinson, D. A. H.; Wiley, J.D., *Rev. Sci. Intrum*. **1976**, *47*, 799.

(13) Yablonowitch, E.; Swanson, R. M.; Eades, W.D.; Weinberger, B.R., *Appl. Phys. Lett.* **1986**, *48*, 245.

(14) Yablonowitch, E.; Allara, D.L.; Chang, C.C.; Gmitter, T.; Bright, T. B. *Phys. Rev. Lett.* **1986**, *57*, 249.

(15) M/A-COM Control Components Division Catalog, 147, Merrimack, NH, USA 1991.

(16) Warman, J.M. ,Schuddeboom, W., Jonker, S.A., DeHaas, M.P., Paddonrow, M.N., Zachariasse, K.A. and Launav, J.P., Chem. Phys. Lett. **1993**, *210*, 397.

(17) Pender, H.; Warren, S.R. *Electric Circuits and Fields*, 1st ed.; McGraw-Hill: New York, 1943; pp. 340 ff.

(18) Fukushima, E.; Roeder, S.B.W. *Experimental Pulse NMR: A Nuts and Bolts Approach*, 3rd ed.; Addison-Wesley: London, 1980, p. 379, p. 414.

(19) Thompson, H.A. *Alternating -Current and Transient Circuit Analysis*, 2nd ed.;McGraw-Hill: New York, 1955; pp. 143-151.

(20) Rothenberger, G.; Moser, J.; Graetzel, M.; Serpone, N.; Sharmaa, D. K. J., *J. Am. Chem. Soc.*. **1985**, *107*, 8054.

(21) Henglein, A., *Ber. Bunsenges. Phys. Chem.* **1982**, *86*, 241.

(22) Hauffe, K., in *Electrochemistry: The Past Thirty and the Next Thirty Years*, Eds. Bloom, H. and Gutmann, F.; Plenum Press: New York, 1977.

(23) Brus, L. E., *J. Chem. Phys.* **1984**, *80*, 4403.

(24) Marcus, R.A. and Sutin, N., Biochim. Biophys. Acta, **1985**, *811*, 265.

(25) Marcus, R.A., J. Phys. Chem. **1990**, *94*, 1050.

(26) Lewis, N.S., Annu. Rev. Phys. **1991**, *42* 543.

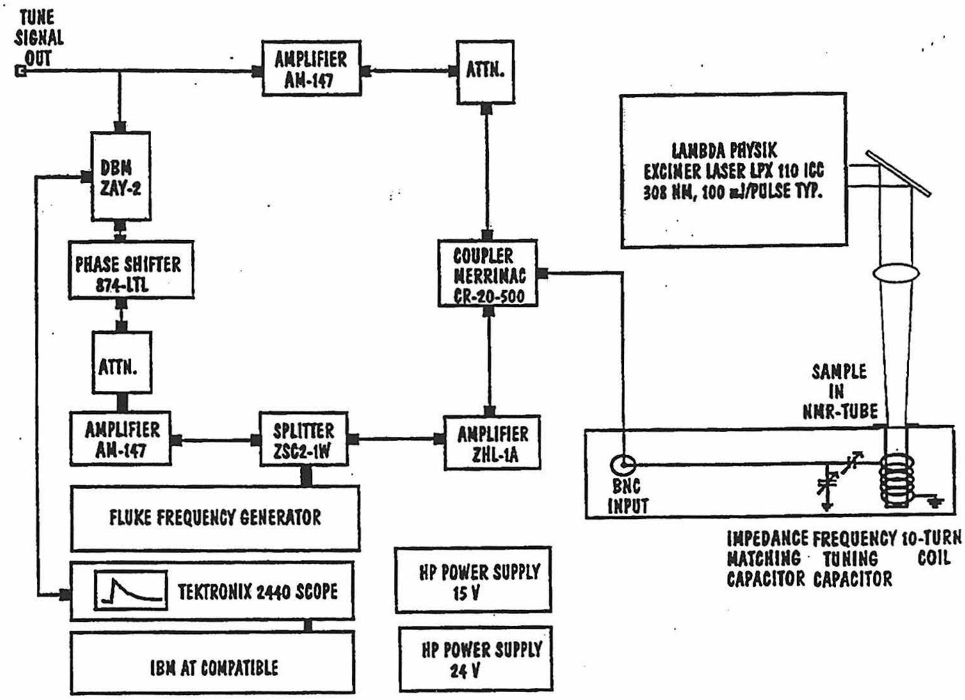

Figure 1: Schematic representation of time-resolved radio-frequency conductivity (TRRFC) apparatus.

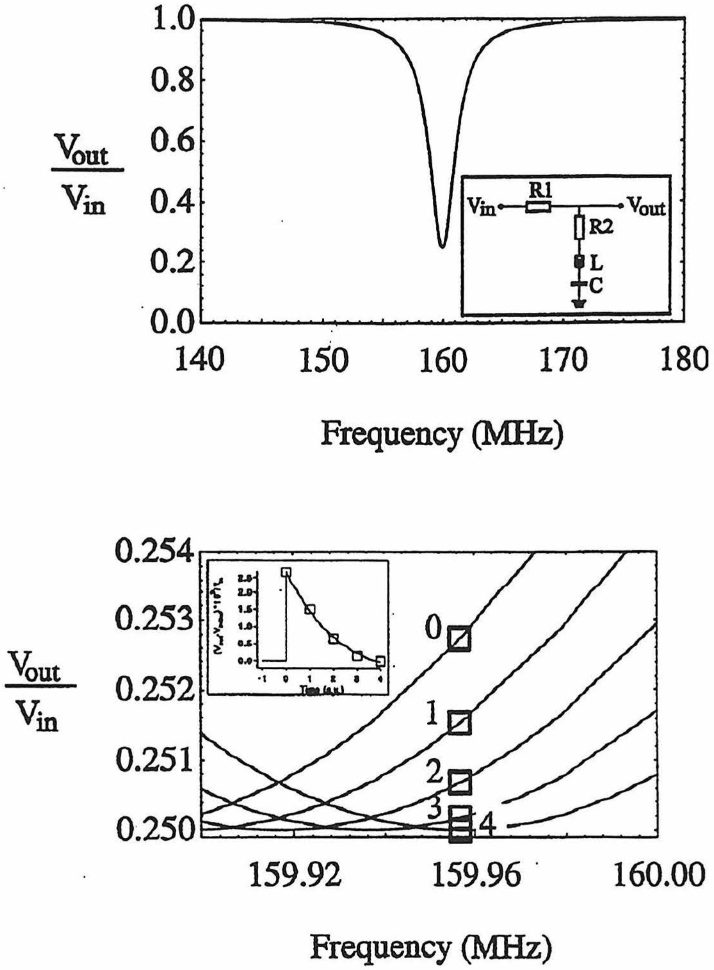

Figure 2: a, top: Q-well calculated from eq 1 for the circuit shown in the inset. $R_1 = R_2 = 2\ \Omega$, L = 240 nH, C = 4.125 pF. b, bottom: Change of Q-well due to variation of L and the resulting time-depending TRRFC signal (inset).

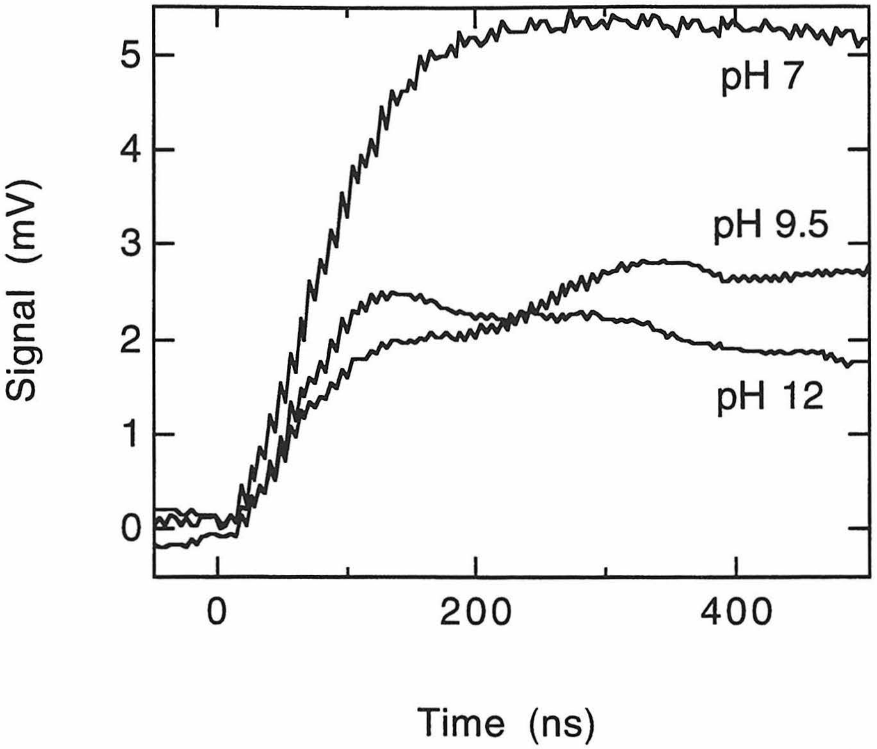

Figure 3: Time-resolution and sensitivity of the TRRFC experiment (1 g/L ZnO aqueous suspensions) for pH = 7.0, 9.5, and 12.0. 200 ns/div timebase. Overlay of original traces.

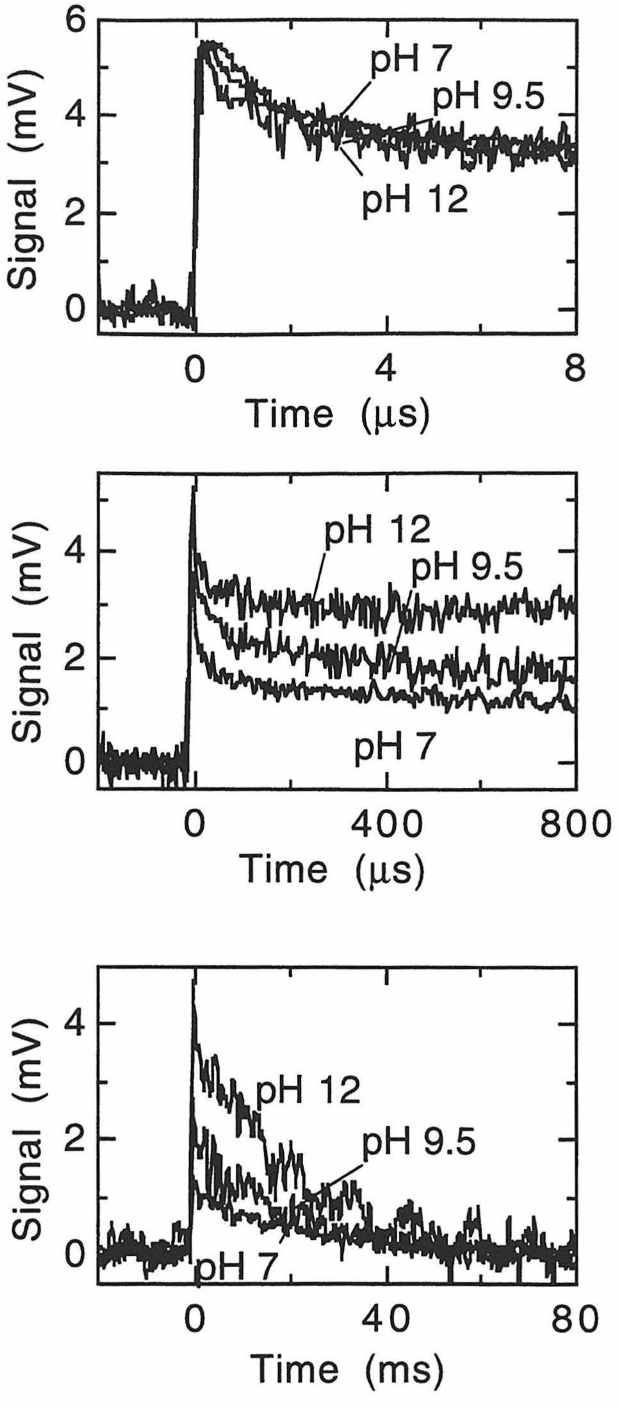

Figure 4: Effect of pH on charge carrier recombination dynamics in 1 g/L ZnO aqueous suspensions. (a, top) 2 μs/div timebase. (b, middle) 200 μs/div timebase. (c, bottom) 10 ms/div timebase, normalized traces (see text).

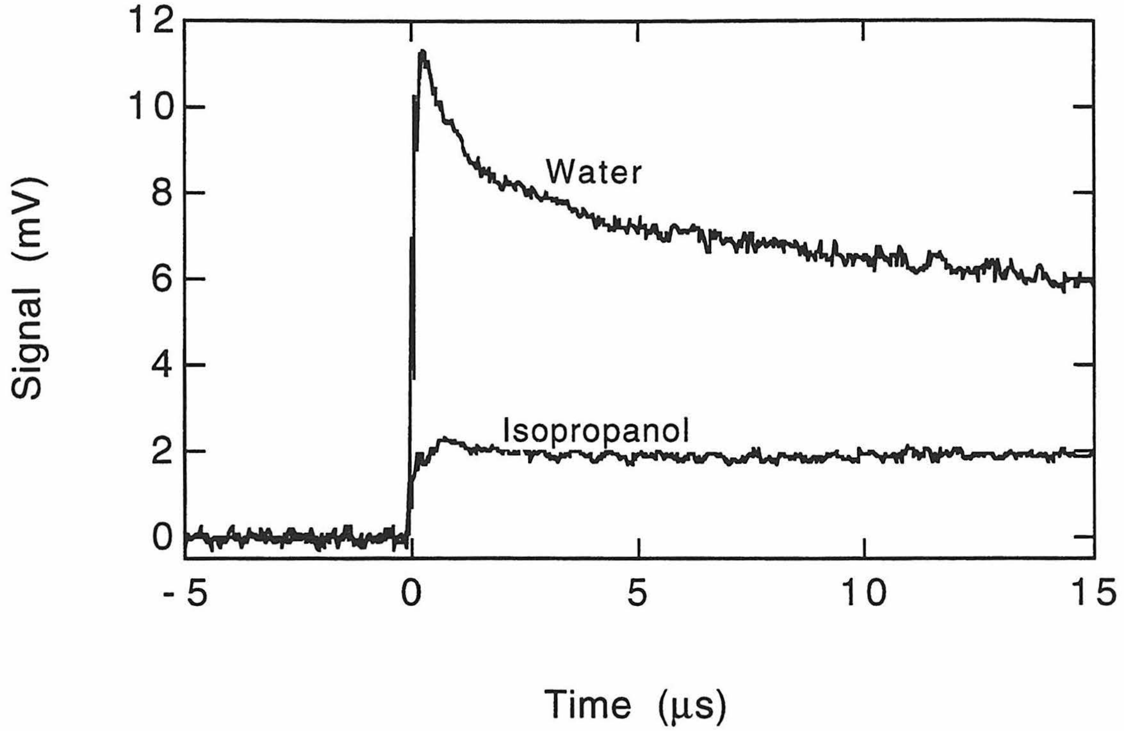

Figure 5: TRRFC signal from 1 g/l ZnO in isopropanol in comparison to the aqueous suspension at unadjusted pH, i.e., pH = 8.5.

Chapter 5

Photochemical Mechanism of Size-Quantized Vanadium-Doped TiO_2 Particles

[The text of this chapter appeared in Martin, S.T., Morrison, C., and Hoffmann, M.R., *Journal of Physical Chemistry*, **1994**, *98*, 13695.]

Abstract

Transition metal ions doped into TiO_2 can increase the quantum efficiency of the heterogeneous photo-oxidation of chlorinated hydrocarbons. In this regard, a single dopant (vanadium) has been selected for a detailed investigation to elucidate the mechanism of the dopant action on the photoreactivity of TiO_2. Large polycrystalline (1-4 nm) TiO_2 particles (50 µm) that show size-quantization effects due to the individual crystallites are synthesized. Doping (1 atomic %) of the TiO_2 crystals with vanadium reduces the photo-oxidation rates of 4-chlorophenol (4-CP) compared to the undoped aggregates. Under ambient conditions (25 °C), vanadium is found to be present primarily on TiO_2 surfaces as $>VO_2^+$ (~90%) (">" denotes a surficial moiety) and secondarily as interstitial V^{4+} (~10%). Sintering at higher temperatures (200-400 °C) results in the formation of surficial islands of V_2O_5 on TiO_2 while sintering at 600 and 800 °C produces non-stoichiometric solid solutions of $V_xTi_{1-x}O_2$. Vanadium appears to reduce the photoreactivity of TiO_2-25 by promoting charge-carrier recombination with electron-trapping at $>VO_2^+$ whereas V(IV) impurities in surficial V_2O_5 islands on TiO_2-200/400 promote charge-carrier recombination by hole-trapping. Substitutional V(IV) in the lattice of TiO_2-600/800 appears to act primarily as a charge-carrier recombination center that shunts charge-carriers away from the solid-solution interface with a net reduction in photoreactivity. The complexities of the physical and electronic effects of vanadium-doping are expected to be present in the mechanisms of other transition metal ions doped into TiO_2.

Introduction

Transition metal ions doped into TiO_2 can increase the quantum efficiency of the heterogeneous photo-oxidation of chlorinated hydrocarbons.[1,2] They are known to influence the charge-carrier recombination and interfacial charge-transfer rates of photogenerated carriers.[1-8] Under normal conditions, undoped TiO_2 catalyzes the oxidation of chlorinated hydrocarbons in the presence of UV radiation more than or equal to the band-gap energy of 3.2 eV or 385 nm according to the following stoichiometry:[9-14]

$$C_xH_yCl_z + \left(x + \frac{y-z}{4}\right)O_2 \xrightarrow[h\nu,\ TiO_2]{} x\,CO_2 + z\,H^+ + z\,Cl^- + \left(\frac{y-z}{2}\right)H_2O \qquad (1)$$

However, for semiconductor particles in the size range of 1 to 10 nm, band-gap energies larger than their bulk-phase counterparts are observed.[15-20] In this region, the size-quantized semiconductor exhibits a larger band-gap energy than its bulk-phase counterpart. In general, a larger band-gap energy should result in larger thermodynamic driving forces and faster charge-carrier transfer rates in the normal Marcus region.[21,22] However, faster charge-carrier recombination rates tend to limit the relative photoefficiencies obtained with quantum-sized ("Q") TiO_2 photocatalysts.[21,22] In principle, selectively-doped Q-sized particles may minimize the recombination channel and thus yield higher quantum efficiencies.[1,2]

The photophysical mechanisms of doped-TiO_2 are not well understood. Key questions include the following: (1) Are the transition metal ions located primarily on the surface or in the lattice? (2) Is the surficial binding of substrates affected by doping? (3) Do transition metal ions influence charge-pair recombination? (4) Do altered interfacial transfer rate constants associated with surficial transition metal ion complexes play a primary role in altered photochemical kinetics?[5,6,23,24]

In order to address these questions, we have selected a single dopant (vanadium) for a detailed investigation to elucidate the mechanism of the dopant action on the photoreactivity of TiO_2. Vanadium was chosen for its reported positive effects on photoreactivity[1,2] as well as the large body of literature available on the the mechanism of thermal transformations catalyzed by V_2O_5 supported on TiO_2.[25] In this regard, we have characterized vanadium-doped and undoped TiO_2 in both the Q-sized and bulk-sized domain with TEM, SEM, Raman, ICP-MS, and UV/Vis reflectance spectra. We have investigated the photoeffects of the dopant on quantum efficiencies, EPR spectra, and time-resolved microwave conductivity (TRMC) decays. Our working hypothesis is that the effects on quantum efficiencies due to size-quantization and surface morphologies (i.e., heat treatment) can be uncoupled from the effects of vanadium-doping by comparing vanadium-doped TiO_2 to undoped TiO_2 prepared in an identical manner except for the doping.

Experimental Section

Preparation. Vanadium-doped TiO_2 was prepared in the size-quantized regime by standard co-precipitation methods.[3,21,25] 5 mL (17.9 mmol) titanium (IV) tetraisopropoxide (Aldrich, 97%) was added to 8 mL 50% (v/v) $HClO_4$ at 0 °C. The preparation was diluted to 100 mL with H_2O and evaporated (35 °C) using a Rotavapor (model R110). The resulting film was dissolved in 200 mL H_2O and then dialyzed (Spectra/Por membrane, MW cutoff 12,000-14,000) to pH 3.1. Following dialysis, the colloids were freeze-dried. Five fractions (300 mg each) of the collected white powder were heat-treated in quartz boats for 4 hours at 25, 200, 400, 600, and 800 °C and labelled TiO_2-25 through TiO_2-800, respectively.

Vanadium doped samples were prepared by including VCl_3 (21.44 mM) in the $HClO_4$ solution. After aging one week, a clear blue solution indicated preparation of a V(IV) stock solution (21.44 μmol/mL). The added volumes resulted in a nominal atomic doping level of 0.96%. The powders obtained after heat-treatment gradually darkened from light beige at 25 °C to brown at 800 °C (Figure 5).

Characterization. Details of the TEM procedure and the TRMC experiment have been reported previously.[21,22] Secondary-electron images of gold-coated samples prepared on carbon tape were obtained with a Camscan Series II scanning electron microscope. The X-ray images (Tracor Northern 5500 Energy Dispersive X-ray Analyzer) were used for automatic particle-sizing. Raman powder spectra were recorded on a Nicolet 800 FT-IR Spectrometer equipped with a FT Raman Accessory. UV/Vis reflectance spectra were recorded on a Shimadzu UV-2101 PC UV-Vis Scanning Spectrophotometer equipped with an ISR-260 Integrating Sphere Assembly. Reflectance spectra were referenced to $BaSO_4$.

Vanadium concentrations were determined by analysis with ICP-MS (Perkin Elmer Sciex Elan 5000). Samples were prepared by acid-extraction in 10% (v/v) concetrated H_2SO_4 by stirring for 48 hours followed by filtration through 0.45 μm nylon filters. Base-extracted samples were prepared at pH 11 with NH_4OH by stirring for 48 hours during which time the pH did not change. The samples were then centrifuged at 11,000 rpm for 30 min, and the supernatant was filtered through 0.45 μm filters. Fully dissolved samples were prepared by stirring in a 50% (v/v) HF (48%) solution. The rutile samples were heated to 100 °C for 1 hour to achieve complete dissolution.

An E-line Century X-band Spectrometer (Varian, Palo Alto, CA) equipped with a V-4531 Multi-purpose Cavity was used to record the first-derivative EPR spectra at 77 K. $CuSO_4$ was used as a calibration standard. In situ illumination was carried out at 20 min. intervals with an 450 W Hg arc lamp (Oriel Corp.) and wavelengths were selected ($310 < \lambda < 380$) with a Kopp 7-60-1 bandpass filter, a 10-cm water filter, and two infra-red filters (Oriel Corp.) in-line.

Photoreactivity Studies. Reagent grade 4-chlorophenol, 1,4-benzoquinone, and hydroquinone were obtained from Aldrich. Aqueous slurries (22 mL) of TiO_2 (1.0 g/L) and 4-chlorophenol (150 μM) were prepared. Irradiations were performed with a 1000 W Xe arc lamp (Oriel Corp.). The infrared component of the incident light was removed by a 10-cm water filter. Wavelengths were selected with an interference filter (Oriel #59620, $\lambda = 324 \pm 5$ nm FWHM). The chemical actinometer Aberchrome 540 ((E)-α-(2,5-dimethyl-3-furyl)ethylidene)-3-isopropylidenesuccinic anhydride) was used to determine the incident light intensity, which was found to be 200 μM min^{-1}.[26] The aqueous slurries were stirred and bubbled with humid oxygen (10 mL min^{-1}) for 60 min prior to and during the irradiation. At 60 minute intervals, samples (100 μL) were extracted through 0.45 μm Nalgene nylon filters (part no. 176-0045) for analysis by HPLC (Hewlett Packard Series II 1090 Liquid Chromatograph). Compounds were separated on a reverse-phase column (Hewlett-Packard 5 μm ODS Hypersil) using a gradient elution program (100%

H_3PO_4 buffer (pH 3.0) to 80:20 H_3PO_4:CH_3CN). Diode array detection at 224 nm and 280 nm was used for quantification.

Results

Photoreactivity. The disappearance of 4-chlorophenol (CP) and the appearance of hydroquinone (HQ) and 1,4-benzoquinone (BQ) in an illuminated TiO_2 slurry are shown as a function of irradiation time in Figure 1. Little degradation takes place in the absence of TiO_2, which indicates that direct photolysis is a minor degradation pathway. Furthermore, no degradation occurs in the absence of light when TiO_2 is present. The apparent increase in concentration (Figure 1, line b) is due to a reduction in volume by evaporation.

The quantum efficiency is defined as

$$\Phi = \frac{\frac{d[CP]}{dt}}{I_{incident}} \qquad (2)$$

where $\frac{d[CP]}{dt}$ is the rate of disappearance of 4-CP and $I_{incident}$ is the incident light intensity determined by chemical actinometry. The relative effects of vanadium-doping and heat-treatment on the observed quantum efficiencies for the photo-oxidation of 4-chlorophenol on TiO_2 are given in Table 1. The undoped TiO_2 yields higher quantum efficiencies than the vanadium-doped counterparts. The drop in the quantum efficiency above 400 °C accompanies the phase transformation from anatase to rutile (Table 3). Undoped TiO_2-600, a mixture of anatase and rutile (Table 3), exhibits a higher photoreactivity than rutile TiO_2-800.

The dependence of the intermediate formed and its maximum concentration as a function of the catalyst used is shown in Table 2. Although BQ and HQ readily interconvert via the HQ-O_2/BQ-H_2O couple (E° = + 0.530), we avoided this possible interference by the rapid and uniform analysis of the samples.

Structure. The transmission electron micrographs (TEM) of vanadium-doped TiO_2-25/800 are shown in Figure 2. Representative microcrystalline particles of TiO_2-25, which are circled for clarity (Figure 2a), have crystallite sizes under 5 nm. Analysis of a wider field of view indicates that the particle-size distribution falls into the range of 1-4 nm (Table 3). The agglomeration of the crystals into porous particles is shown in Figures 4b and c. In these images, the parent particles obtained upon direct synthesis are reduced in size by grinding in order to facilitate TEM analysis. The twinning that is apparent in the TiO_2-800 samples (Figure 2c) suggests a sintering growth mechanism.

The electron diffraction pattern of TiO_2-25 is shown in Figure 3. The Miller indices for TiO_2-25 are derived from the d-spacing for anatase[27] and the reflection rules for D4h symmetry.[28] The transition from broad bands (Figure 3) to distinct spots (not shown) is seen as the crystal size grows from 1-3 nm to 100-400 nm (Table 3). The ED pattern of the quantum-sized crystals (Figure 3) shows Scherrer line broadening attributed to ultra-small crystallites.[29] The absence of diffuse bands normally present in an amorphous substance indicates that the nanometer-sized particles are crystalline. In general, no differences are observed between the TEM images and ED patterns of vanadium-doped and undoped TiO_2.

The particle-size distribution as determined from X-ray images is reported in Table 3. Agglomeration of the polycrystalline particles does not appear to occur during heat-treatment of the undoped particles (Table 3).

No difference is observed between the Raman spectra of doped and undoped TiO_2 (data not shown). Bands at 678, 519, and 403 cm^{-1} for TiO_2-25/200/400 match anatase stretches.[30,31] TiO_2-600 and TiO_2-800 have Raman bands centered at 606 cm^{-1} and 446 cm^{-1}, which agree with the bands observed for rutile.[30,31]

The UV/Vis diffuse-reflectance spectra of undoped TiO_2 are shown in Figure 4. The wavelength of 50% reflectivity is red-shifted by 6 nm and 14 nm as TiO_2-25 is calcined at 200 °C and 400 °C, respectively. The crystallite size (Table 3) grows during the heat-treatment, and the red-shifts correspond to a decrease in the band-gap energy during the transition from Q-sized to bulk-sized particles.[32] The further red-shift induced by heat-treatment at 600 °C corresponds to the rutile phase transition. The UV/Vis diffuse reflectance spectra of vanadium-doped TiO_2 are shown in Figure 5. The band-gap of TiO_2 ($\lambda < 400$ nm) is obscured by a trailing absorption region.

The physical characterization of the samples is summarized in Table 3. Total mass appears to be lost with increasing calcination temperatures. The crystal transition from anatase to rutile starts at 600 °C for the undoped TiO_2 while the vanadium-doped TiO_2 shows a similar transition at much lower temperatures. Vanadium has been shown to catalyze the phase transformation from anatase to rutile with the evolution of oxygen to form a solid solution $V_xTi_{1-x}O_2$.[33,34] Although the apparent crystal sizes increase with calcination temperature, the sizes (radius) and dispersities (σ) of the agglomerated particles do not show a similar trend for undoped TiO_2 samples. The vanadium-doped TiO_2 samples appear to follow a general trend to increased size (%N). The %N column shows the number percentage of TiO_2 particles that have a cross-sectional area greater than 500 μm^2.

Surface Chemistry. The results of the chemical analyses of the vanadium-doped TiO_2 are shown in Table 4. Base-extraction of vanadium is a common approach to determine the chemical speciation of vanadium on TiO_2.[35-37] In addition, we characterized the vanadium based upon an acid-extractable portion. The two extractions show maxima in samples calcined at 400 °C. No vanadium is found in the supernatant at pH 4. The greater portion of vanadium extracted under acidic conditions may be due to the partial dissolution of TiO_2. This explanation is suggested by the ICP-MS detection of titanium in the acid-extracted sample but not in the base-extracted sample. Though the nominal doping level is 1%, the complete dissolution of the samples indicates a vanadium concentration of ~0.4%. Vanadium may have been lost during dialysis of the colloid. The base-extraction of vanadium-doped TiO_2-25/200/400 bleaches the chromophore to yield a white slurry.

Electron Paramagnetic Resonance. The EPR spectra of vanadium-doped TiO_2 are shown in Figure 6. The assignment of anisotropic g-factors and hyperfine splitting constants for TiO_2-800 is shown in Figure 6a. The distinct EPR spectra observed for the groups TiO_2-25, TiO_2-200/400, and TiO_2-600/800 are shown in Figure 6b. The EPR parameters and signal intensities of TiO_2-25-800 are reported in Table 5. Based upon the signal strength of the $CuSO_4$ standard, a 1% vanadium-doping level results in $I \sim 10^3$ if all vanadium is in the EPR active state, which is believed to be exclusively V(IV).[35] The signal strengths indicate the vanadium is speciated as ~10% V(IV) for TiO_2-25, ~1% for TiO_2-200/400, and ~100% for TiO_2-600/800. Our EPR interpretation should be considered a qualitative guide to vanadium speciation because accurate quantification requires knowledge of the transition probabilities of the copper standard and the vanadium in its different electronic environments as well as compensation for the variations in linewidths.

The literature values of EPR parameters are reported in Table 6. The g-factors and hyperfine splitting constants of TiO_2-25 have been assigned previously (Table 5) as interstitial V(IV) in anatase.[3,38] The EPR spectra of TiO_2-200/400 exhibit a broad signal attributable to V(IV) in V_2O_5.[34,39] In addition, the spectrum of TiO_2-200 shows an additional species of V(IV) that exhibits hyperfine structure whereas the spectrum of TiO_2-400 shows two additional speciations of V(IV). The second signal of TiO_2-200 also appears in TiO_2-400 and the orthorhombic g-factors are reported in Table 5. g-Factors for the third signal apparent in TiO_2-400 are not reported due to the low signal intensity and difficulties in deconvulting the third signal from the second. Although we do not have sufficient information to assign the additional signals present in TiO_2-200/400, V(IV) is present at a level of ~1% based upon the signal intensity and, hence, the majority of vanadium is present as V(V). The EPR parameters of TiO_2-600/800 match those of substitutional V(IV) in rutile.

The effects of irradiation of the vanadium-doped TiO_2 on the EPR spectra are shown in Figure 7. The difference spectra are the result of the subtraction of the dark spectra from the irradiated spectra. Although no change is observed for TiO_2-800, new EPR absorptions are apparent for TiO_2-25 and TiO_2-400. The changes in the spectrum of TiO_2-25 show no loss of original signal and the appearance of a new signal with vanadium hyperfine splitting. The original signal did not return after storage in the dark. The weak signal intensity due to the irradiation of only a small portion of the sample precludes assignment of g-factors. The changes in the spectra of TiO_2-400 are due to the partial loss of one vanadium absorption and the appearance of an absorption exhibiting no hyperfine splitting. The original spectrum is recovered upon storage of the sample in the dark. The g-factors of superoxide (2.002), interstitial anatase Ti(III) ($g_x = 1.988$, $g_z = 1.957$), and $Ti(III)(H_2O)_6$ ($g_z = 1.988$) are shown and appear to be present in the EPR spectrum of TiO_2-400. These systems are not degassed and no hole scavengers are added.

Time-Resolved Microwave Conductivity. The TRMC transients of vanadium-doped TiO_2 are shown in Figure 8. Due to the weak signal of the vanadium-doped TiO_2, a laser pulse energy of 38 mJ is used instead of 4.5 mJ typically used for undoped TiO_2.[21,22] The initial signal decays on the ms timescale in all cases. The decay of TiO_2-25 is successfully fit with a single exponential decay ($I = 0.50 \pm 0.01$ mV, $k = 0.052 \pm 0.001$ ms^{-1}) whereas TiO_2-400 ($I_1 = 0.31 \pm 0.02$ mV, $k_1 = 0.07 \pm 0.01$ ms^{-1}, $I_2 = 0.18 \pm 0.02$ mV, $k_2 = 1.4 \pm 0.4$ ms^{-1}) and TiO_2-800 ($I_1 = 1.03 \pm 0.01$ mV, $k_1 = 0.094 \pm 0.002$ ms^{-1}, $I_2 = 0.42 \pm 0.03$ mV, $k_2 = 3.7 \pm 0.4$ ms^{-1}) are fit to a double exponential decay.

Discussion

Structure of the Photocatalyst. The Q-sized TiO_2 particles are composed of 1-4 nm crystallites agglomerated into 50 μm particles (Figures 4 and 6 and Table 3). Q-sized crystallites increase in size from 1 to 500 nm due to sintering during heat-treatment. The macroparticles have nanometer-sized porous channels (Figure 2c) which lead to high reactive surface areas. The bleaching of vanadium chromophores by base-extraction suggests that the entire reactive surface is chemically available. The ready accessibility of the internal surface area implies limited surficial contact among the crystals. Thus, each crystallite can be considered to be electronically isolated. The isolated nature of the crystallites is shown by the observed size-quantization effect (Figure 4) in which the onset of absorption (i.e., bandgap) correlates with the crystallite size (Table 3).

Comparison of the g-factors and the signal intensities from the EPR measurements of TiO_2-25 (Tables V and VI) indicates that ~10% of the vanadium is present as interstitial V(IV) in the TiO_2 lattice. The remaining vanadium may be present on the surface as V(V) (i.e., VO_2^+) through the formation of surface structures not susceptible to EPR detection:[25]

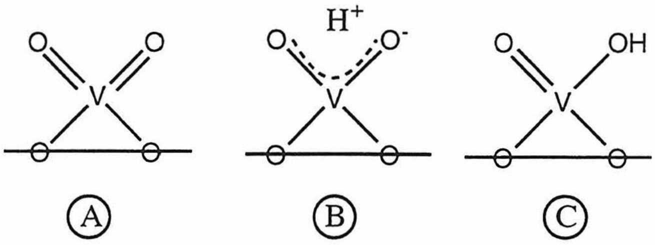

The low signal intensities and the broad EPR signals at $g = 1.975$ (Figure 6) of TiO_2-200/400 indicate that the vanadium is speciated as low-levels of V(IV) impurities in V_2O_5.[34,39] Some V(IV) may also be present in the lattice or on the surface and may give rise to the fine structure shown in Figure 6; however, the low signal intensity suggests that 99% of the vanadium is present as V_2O_5. The V_2O_5 is believed to be present as vanadia islands on the TiO_2 surface because a monolayer coverage requires at least 1% (atomic) vanadium loading.[40] The g-factors and the signal intensities of TiO_2-600/800 show that most vanadium is present as substitutional V(IV) in the rutile modifications in the form of a solid solution with a non-stoichiometric formula of $V_xTi_{1-x}O_2$.[37,41,42] The stabilizing effect of vanadium in the rutile lattice[37,41,42] is shown by the complete transformation of vanadium-doped TiO_2 to rutile by heat-treatment at 600 °C (Table 3) whereas only partial conversion is obtained for the undoped sample treated in an identical manner. Based upon the EPR measurements, vanadium appears to be fractionated as interstitial sites in TiO_2-25 (~10% of the total vanadium), as surficial V_2O_5 (~99%) and an unidentified location in TiO_2-200/400, and as substitutional V(IV) (~100%) in TiO_2-600/800. The effects of base-extraction (*vide infra*) suggest the missing vanadium (~90%) in TiO_2-25 is present as $>VO_2^+$, which would not be susceptible to EPR detection.

The resultant oxidation states of vanadium in TiO_2 may be explained by the following overall redox and thermal reactions starting with the precursor VCl_3 (V(V) = VO_2^+ and V(IV) = VO^{2+}):[43]

$$2\ \mathrm{V(III)}\ (\text{green}) + \frac{1}{2} O_2 + H_2O \rightarrow 2\ VO^{2+}\ (\text{blue}) + 2H^+ \qquad E° = +\ 0.89\ \mathrm{V} \qquad (3)$$

$$2\ VO^{2+}\ (\text{blue}) + \frac{1}{2} O_2 + H_2O \rightarrow 2\ VO_2^+\ (\text{yellow}) + 2\ H^+ \qquad E° = +\ 0.229\ \mathrm{V} \qquad (4)$$

$$2\ VO_2^+ + H_2O \rightarrow V_2O_5 + 2\ H^+ \qquad \Delta G° = -\ 10.5\ \mathrm{kJ/mol} \qquad (5)$$

$$V_2O_5 + \text{heat} \rightarrow V_2O_4 + \frac{1}{2} O_2 \qquad (6)$$

VCl_3 is transformed into VO^{2+} (eq 3) prior to addition of the titanium-alkoxide. During the synthesis, a portion of the VO^{2+} undergoes further oxidation to VO_2^+ (eq 4) to form surface complexes. The remaining VO^{2+} diffuses into the anatase lattice as interstitial V(IV). Upon firing at 200-400 °C, at least 90% (based upon EPR signal strengths) of the interstitial V(IV) migrates to the surface and is oxidized by O_2 (eq 4) to yield V_2O_5 islands (eq 5) on the surface. Heat-treatment at 600-800 °C causes the decomposition of the V_2O_5 islands and the evolution of O_2 (eq 6). The V(IV) product, V_2O_4, then redissolves into the rutile lattice.[34,44]

The chemical nature of the surficial groups is indicated by the bleaching of the vanadium chromophores with base-extraction, which selectively dissolves away surficial vanadium.[39] Base-extracTable 5anadium in samples prepared by the co-precipitation method is in the +5 oxidation state and is due to weakly interacting surficial species such as V_2O_5 or $>VO_2^+$.[36,37] The maxima in acid and base-extractions for TiO_2-200/400 (Table 4) agree with the minima observed in the EPR measurements (Table 5) and support the conclusion that weakly interacting surficial V_2O_5 islands are present. No chromophoric bleaching of TiO_2-600/800 occurs. This result suggests that much of the vanadium is not extractable and is consistent with a solid solution of $V_xTi_{1-x}O_2$.

Mechanism of Photocatalysis. In the absence of vanadium, we have proposed the following mechanism for photochemical catalysis on TiO_2 based on laser flash-photolysis measurements:[21,22]

Primary Process	Characteristic Timescale	
Charge-carrier generation		
$TiO_2 + h\nu \rightarrow e^- + h^+$	(fs)	(7)
Charge-carrier trapping		
$h^+ + >OH \rightarrow >OH^{\cdot +}$	fast (10 ns)	(8)
$e^- + Ti(IV) \leftrightarrow Ti(III)$	dynamic equilibrium (100 ps)	(9)

Charge-carrier recombination

$e^- + {>}OH^{\cdot+} \rightarrow TiO_2$ slow (100 ns) (10)

$h^+ + Ti(III) \rightarrow TiO_2$ fast (10 ns) (11)

Interfacial charge transfer

${>}OH^{\cdot+} + Red \rightarrow TiO_2 + Red^{\cdot+}$ slow (100 ns) (12)

$e^- + Ox \rightarrow TiO_2 + Ox^{\cdot-}$ very slow (ms) (13)

We assume that the substrate does not undergo direct hole transfer.

Using this mechanism, the quantum efficiency of a charge-pair generated by an incident photon (eq 7) towards the oxidation of a substrate (eq 12) is given by:

$$\phi_{12} = \frac{k_{12}[> OH^{+\cdot}][\mathrm{Re}\,d]}{I} \qquad (14)$$

where the light intensity, I, is a constant flux. During continuous illumination, $[h^+]$, $[e^-]$, [Ti(III)], $[>OH^{\cdot+}]$, [Red], and [Ox] may be considered constant because changes due to the mineralization of [Red] occur much more slowly (minutes) than the time period of the transition from transient conditions to steady-state conditions (ms).

Under perturbations such as enhanced charge-carrier trapping (eqs 8 & 9) or recombination (eqs 10 & 11) that may be introduced by vanadium-dopants, k_{12}, [Red], and I are constant. However, $[>OH^{+\cdot}]$ is a function of charge-carrier dynamics through the rates of eqs 8, 10, and 12. These rates in turn affect $[h^+]$ and $[e^-]$, which depend on the rates of eqs 7, 8, and 11 and 7,9, 10, and 13, respectively.

Although the interdependencies preclude an analytical solution, several of the equations may be uncoupled because they describe processes occurring with different characteristic times. In this case, the qualitative behavior of the system can be deduced. For instance, the photogenerated hole of eq 7, which results in substrate (Red) oxidation (eq 12), must first survive an initial branching event (eqs 8 & 11, $\tau \approx 10$ ns) before it is sequestered as a surficial hydroxyl group (eq 8). The trapped-hole (i.e., $>\mathrm{TiOH}^{\bullet +}$) then undergoes a second branching sequence (eqs 10 & 12, $\tau \approx 100$ ns) resulting in the elimination of the hole from the particle. The quantum efficiencies of the initial branching event are:

$$\phi_8 = \frac{k_8[h^+][>OH]}{I} \tag{15}$$

$$\phi_{11} = \frac{k_{11}[h^+][Ti(III)]}{I} \tag{16}$$

$$\phi_8 + \phi_{11} = 1 \tag{17}$$

The product of eq 8 is $>\mathrm{OH}^{+\cdot}$, which is the source term for the second competition (eqs 10 & 12), for which the quantum efficiencies are:

$$\phi_{10} = \frac{k_{10}[e^-][>OH^{+\cdot}]}{I} \tag{18}$$

$$\phi_{10} + \phi_{12} = \phi_8 \tag{19}$$

ϕ_{12} is given in eq 14.

Under steady-state conditions, electrons and holes undergo interfacial charge transfer at the same rate:

$$\phi_{13} = \frac{k_{13}[e^-][Ox]}{I} \tag{20}$$

$$\phi_{12} = \phi_{13} \tag{21}$$

An increase of k_8 would yield an increase of ϕ_8 (eq 15) from which increases of $[>\mathrm{OH}^{\cdot+}]$ and ϕ_{12} follow. In addition to these processes that are favorable with respect to increased rates of substrate oxidation, a feedback cycle from a decrease of ϕ_{11} due to an increase of ϕ_8 (eq 17) is also operative. The consequent increases of [Ti(III)] (eq 11) and $[e^-]$ (backward reaction of eq 9) and decreases of $[>\mathrm{OH}^{+\cdot}]$ (eq 10) and ϕ_{12} (eq 12) are considered secondary in this analysis (iterative computer calculations of these equations is hindered by the lack of accurate numbers for many of the concentrations and rate constants). By a similar analysis, we conclude that increases of ϕ_{12} correlate with increases of ϕ_8 (eq 15) or ϕ_{13} (eqs 20 & 21) and decreases of ϕ_{10} (eqs 18 & 19) or ϕ_{11} (eqs 16 & 17).

The net effects of vanadium-doping on photoreactivity include the following processes:

(1) mediation of interfacial charge transfer by surficial complexes as follows:

(a) $h^+ + >\mathrm{VO_x} \rightarrow >\mathrm{VO_x}^+$

followed by $>\mathrm{VO_x}^+ + \mathrm{Red} \rightarrow >\mathrm{VO_x} + \mathrm{Red}^+$ (22)

or (b) $e^- + >\mathrm{VO_x} \rightarrow >\mathrm{VO_x}^-$

followed by $$>VO_x^- + Ox \rightarrow >VO_x + Ox^-, \qquad (23)$$

(2) changes in the surficial concentrations of the reactants and, hence, the rates of eqs 12 and 13 by the binding of the substrate to surficial vanadium complexes

(3) mediation of charge-carrier recombination by surficial or bulk dopants

$$V(x) + e^- \rightarrow V(x\text{-}1) \quad \text{followed by} \quad V(x\text{-}1) + h^+ \rightarrow TiO_2$$

$$\text{or} \quad V(x\text{-}1) + >OH^{\cdot} \rightarrow TiO_2 \qquad (24)$$

$$V(x) + h^+ \rightarrow V(x+1) \quad \text{followed by} \quad V(x+1) + e^- \rightarrow TiO_2. \qquad (25)$$

Based upon our present results, (2) would not appear to play a major role in the solid solutions of $V_xTi_{1-x}O_2$ obtained for TiO_2-600/800.

The effects of light on the EPR signals (Figure 7) and TRMC experiments (Figure 8) provide further insight into the possibilities of the various mechanisms. The change in EPR signal of TiO_2-400 due to irradiation results in the loss of the V(IV) signal and the appearance of discrete signals assignable to O_2^-, interstitial $Ti(III)_{anatase}$, and $Ti(III)(H_2O)_6$. These changes are consistent with the following sequence:

Hole-trapping

$$V(IV) + h^+ \rightarrow V(V) \qquad (26)$$

Electron-trapping

$$Ti(IV) + e^- \rightarrow Ti(III) \qquad (27)$$

Oxygen reduction

$$O_2 + e^- \rightarrow O_2^- \qquad (28)$$

Photodissolution

$$\text{Ti(IV)} + e^- \rightarrow \text{Ti(III)}(H_2O)_6 \qquad (29)$$

The apparent reversibility of the photoeffect on the EPR signal of TiO_2-400 is consistent with charge-carrier recombination processes (eqs 26-28). The observed reversibility in conjunction with the resistance of TiO_2 to photocorrosion would appear to rule out photodissolution (eq 29) as a major pathway. In this case, the signal at 1.988 is assigned exclusively to interstitial Ti(III) anatase formed by electron-trapping (eq 27). The formation of reduced species suggests the vanadium acts as a hole trap (eq 26) in TiO_2-400 . The possibility that the hole traps may be V(IV) impurities in surficial V_2O_5 islands would suggest the formation of $>OH^{+\cdot}$ would not occur (eq 8). Thus, even though hole-trapping may reduce a channel for charge-carrier recombination (eq 10), the overall photoreactivity may be reduced if $>OH^{+\cdot}$ radical does not form because interfacial charge transfer (eq 12) may not take place. In this case, the fate of trapped-hole is recombination mediated by the vanadium-dopant (eq 25).

Upon illumination of TiO_2-25 a new V(IV) signal appears in the EPR spectrum (Figure 7). The overall hyperfine signature of vanadium is apparent, though the tensor assignment is not possible due to the weakness of the signal. The irreversible nature of the photoeffect upon storage in the dark suggests that a permanent chemical change due to interfacial charge transfer occurs because charge-carrier trapping is expected to be reversible. The apparent reduction of $>V(V)O_x$ is consistent with the photoeffects on the EPR spectrum, the dark EPR spectrum (Figure 6), and the effects of base-extraction:

$$>\mathrm{VOO\ (V)} + e^- + H^+ \rightarrow\ >\mathrm{VOOH\ (IV)} \tag{30}$$

Thus, hole-trapping via eq 26 appears to be absent in TiO_2-25.

TiO_2-800 does not exhibit a photoeffect on the EPR spectra (Figure 7). Grätzel et al.[3] report a similar result under ambient conditions; however, the authors further report that the EPR signal intensity decreases upon irradiation in the absence of O_2. In fact, the presence of either O_2 or H_2 prevents the loss of signal upon irradiation and the authors propose the following processes in addition to hole-trapping (eq 26):

Electron trapping

$$\mathrm{V(IV)} + e^- \rightarrow \mathrm{V(III)} \tag{31}$$

Recombination

$$\mathrm{V(III)} + \mathrm{V(V)} \rightarrow 2\ \mathrm{V(IV)} \tag{32}$$

Charge-carriers may undergo interfacial charge transfer to oxygen and hydrogen (eqs 12 & 13), which prevents recombination (eq 32) and reduces the the EPR signal due to V(IV). Vanadium located at substitutional sites in the rutile lattice thus acts principally to promote charge-carrier recombination.

The TRMC measurements of undoped TiO_2 yield a relative lifetime for Ti(III).[21,22] Although hole-trapping and electron-trapping at V(IV) in the TiO_2 lattice result in V(V) and V(III) species, respectively, these traps are believed to be deep[45,46] and thus not susceptible to detection by TRMC. The 8-

fold reduction of the TRMC signal of the vanadium-doped TiO_2 relative to the undoped TiO_2 suggests that vanadium-dopants may facilitate nanosecond charge-carrier recombination (eqs 24-25), trap charge-carriers (eqs 26 & 31), or reduce charge-carrier mobility. A decrease in charge-carrier mobility reduces the conductivity while nanosecond charge-carrier recombination reduces the initial conductivity. In addition to reducing the initial conductivity, trapping also affects the time-resolved charge-carrier recombination. The independence of the conductivity with respect to the surficial content of the vanadium and the magnitude of the effect suggest a reduction in carrier mobility is an insufficient explanation for the reduced conductivity. An explanation that enhanced charge-carrier recombination alone results in the reduced conductivity would also appear to be insufficient because an 8-fold increase in charge-carrier recombination is not consistent with the 2-5 fold drop in quantum efficiency relative to undoped TiO_2-25/200/400 (Table 1). However, this explanation may be valid for TiO_2-600/800, which show no photoreactivity. To explain the reduced signal strengths of TiO_2-25/400, we suggest charge-carrier trapping also takes place. Furthermore, the necessity of double exponential fits to reproduce the TRMC conductivity decays suggests charge-carrier trapping because single exponential fits are sufficient for the decays of undoped TiO_2. We thus propose direct evidence that electron-trapping at V(x) (eq 24) competes with trapping at Ti(IV) (eq 9).

Activity of the Photocatalyst. The effect of vanadium-doping on the photoreactivity of TiO_2 is evaluated by studying the photo-oxidation of 4-CP.[47-53] The principal intermediates and reaction stoichiometry are:

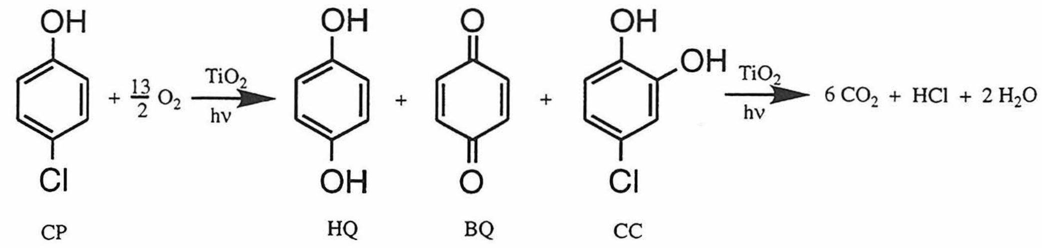

4-CP adsorbs to the surface of TiO_2 via a phenolate bridge (A), and $>VO_x$ may also complex 4-CP (B):[5,6,54-56]

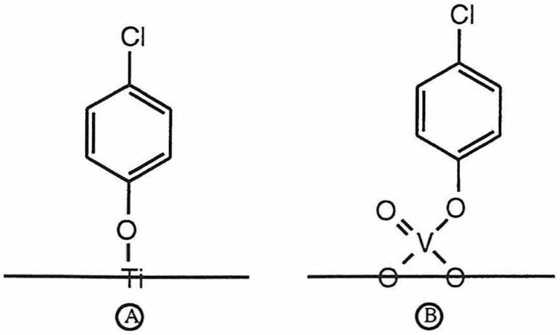

The binding constant of 4-CP at $>VO_x$ relative to $>TiOH$ suggests the expected effect on the the surface concentration of the substrate and, hence, on the photoreactivity exclusive of any electronic effects. This consideration is important for TiO_2-200/400 in which most of the vanadium is located as V_2O_5 islands on the surface. In addition, non-specifically physisorbed 4-CP (e.g., through van der Waals attractions) may react. Different surface geometries are at least partially implicated by the sets of intermediates (Table 2) observed for anatase and rutile. The absence of BQ in the vanadium-doped anatase system may suggest that the geometry of the $>VO_x$-(4-CP) complex favors the HQ pathway. Alternatively, electron-trapping at V(IV) forms V(III), which may reduce BQ to HQ:

$$2\,V(III) + BQ + 2\,H_2O \rightarrow 2\,VO^{2+} + HQ + 2\,H^+ \quad E° = +\,0.363\ V \qquad (33)$$

The alternative possibility of reduction from the V(V)/V(IV) couple does not seem plausible since $E° < 0$:

$$2\,VO^{2+} + BQ + 2\,H_2O \rightarrow 2\,VO_2^{+} + HQ + 2\,H^{+} \quad E° = -\,0.300\ V \qquad (34)$$

However, the reduction potentials in our system may be expected to be different from the standard reduction potentials. Mizushima et al. assigned values of V(IV)/V(III) as $E°_{1/2} = +\,0.6$ V and V(V)/V(IV) as $E°_{1/2} = +\,2.1$ V for substitional vanadium in rutile.[46] Using these values, we obtain $E° = +\,0.100$ for eq 33 and $E° = -\,1.400$ for eq 34.

In the undoped anatase TiO_2-25/200/400 (Table 1), the apparent increase in observed quantum efficiency correlates with increasing crystal size in the size-quantized regime. The correlation may be explained by an increase in the charge-carrier recombination rate due to the mixing of electronic states in the size-quantized regime.[22] The reduced photoreactivity of the vanadium-doped TiO_2-25/200/400 relative to the undoped TiO_2 may be attributed partially to an increase for the charge-carrier recombination pathway mediated by the vanadium-dopants and partially to surficial $>VO_x$ complexes that impede the approach of 4-CP to the reactive sites on the surface (e.g., $>TiOH^{\cdot}$). The reduced photoreactivity of undoped TiO_2-600/800 may be explained by the phase transformation to rutile. The lack of photoreactivity in the case of vanadium-doped TiO_2-600/800 seems to be explained by the enhanced charge-carrier recombination mediated by the vanadium dopant as observed by EPR and TRMC.

Vanadium-doped TiO_2 has previously been reported to result in higher quantum efficiencies than its undoped counterpart.[2] In order to investigate the discrepancy between those results and our present findings (Table 1), we carried out photo-oxidation experiments on 4-CP (150 μM) at pH 2.7 using the same transparent colloidal particles used in our previous study, in which we measured the photodechlorination rate of 3 mM $HCCl_3$ at pH 2.7. We find quantum efficiencies of 0.60% and 0.27% for the vanadium-doped and undoped TiO_2, respectively, towards photodechlorination of 4-CP. The ratio of the quantum efficiencies obtained with vanadium-doped and undoped transparent colloidal TiO_2 is 2.2 for the photodechlorination reaction of 4-CP whereas the ratio is 0.44 (Table 1) in a slurry suspension of TiO_2-25. These results seem to preclude the possibility of substrate-specific activity and suggest differences in the photocatalysts. The preparation methods of the transparent colloidal TiO_2 and the agglomerated TiO_2 particles differ in the final drying stage. The former is prepared by rotary evaporation and quickly redisperses to form a transparent aqueous colloid while the latter undergoes freeze-drying and forms slurries upon re-suspension. The photoreactivity of the powders appears to be substantially altered by the preparation procedures that may result in differences in the formation of surface defects or vanadium speciation.

Conclusions

Large polycrystalline TiO_2 particles (50 μm) that exhibit size-quantization effects due to the individual crystallites are synthesized. In a slurry suspensions, these particles scatter light and are easily filtered. For use with a fixed-bed reactor, the particles could be readily immobilized by adhesives. The physical cohesion of the crystallites to form a nanoporous agglomerated particle that exhibits electronic isolation of the crystallites and the ready chemical availability of the reactive surface may contribute to the understanding of nanoporous electrodes.[57-61]

Vanadium-doping of the crystals is found to reduce the photo-oxidation rates of 4-CP relative to undoped TiO_2. Vanadium is present on TiO_2-25 primarily as $>VO_2^+$ (~90%) and secondarily as interstitial V^{4+} (~10%). The deposition of vanadium as surficial islands of V_2O_5 occurs on TiO_2-200/400. A small fraction of the total vanadium (~1%) in TiO_2-200/400 is also present as V(IV). Vanadium-dopants in TiO_2-600/800 are found to be present primarily as a solid solution of $V_xTi_{1-x}O_2$.

Vanadium appears to reduce the photoreactivity of TiO_2-25 by promoting charge-carrier recombination with electron-trapping at $>VO_2^+$ (eq 24) whereas V(IV) impurities in surficial V_2O_5 islands on TiO_2-200/400 promote charge-carrier recombination by hole-trapping (eq 25). Substitutional V(IV) in the lattice of TiO_2-600/800 appears to act primarily as a charge-carrier recombination center that shunts charge-carriers away from the solid-solution interface with a net reduction in photoreactivity (eq 32). Figure 9 represents a pictorial view of the important electronic processes believed to be operative due to the vanadium-doping. The energy levels of the vanadium groups are approximated based upon VO_2^+/VO^{2+} ($E^\circ_{1/2}$ = + 1.00 V), $VO^{2+}/V(III)$ ($E^\circ_{1/2}$ = + 0.337 V), and bulk V_2O_5 (E_{cb} = + 0.9 V, E_{vb} = + 3.7).[62] Furthermore, vanadium-doping affects the crystallite and particle sizes, the crystal form, and the surface structure (e.g., density of surficial hydroxyl ions); these modifications may be important factors governing the differences in the photoreactivities of doped and undoped TiO_2. The particular array of intermediates, the phenolate linkage present with 4-CP, and the presence of surficial vanadium suggest further work on the binding and approach of 4-CP would add further important information to our understanding of the effects of vanadium-doping. The complexities of the physical and electronic effects of vanadium-doping may be expected to be present in the mechanisms of other transition metal ions doped into TiO_2.[1,2]

Acknowledgment. We are grateful to ARPA and ONR {NAV 5 HFMN N0001492J1901} for financial support. S. Martin is supported by a National Defense Science and Engineering Graduate Fellowship. C. Morrison thanks the Bobst foundation for an American University of Beirut Faculty development grant. Wonyong Choi, Peter Green, Nicole Peill, Ronald Siefert, and Dr. Andreas Termin provided valuable support and stimulating discussion.

References

(1) Choi, W.; Termin, A.; Hoffmann, M. R. *Angew. Chem.* **1994**, *106*, 1148.

(2) Choi, W.; Termin, A.; Hoffmann, M. R. *J. Phys. Chem.* **1994**, submitted.

(3) Grätzel, M.; Howe, R. F. *J. Phys. Chem.* **1990**, *94*, 2566.

(4) Finklea, H. O. In *Semiconductor Electrodes*; H. O. Finklea, Ed.; Elsevier: New York, 1988; ; pp 52.

(5) Hong, A. P.; Bahnemann, D. W.; Hoffmann, M. R. *J. Phys. Chem.* **1987**, *91*, 6245.

(6) Hong, A. P.; Bahnemann, D. W.; Hoffmann, M. R. *J. Phys. Chem.* **1987**, *91*, 2109.

(7) Kölle, U.; Moser, J.; Grätzel, M. *Inorg. Chem.* **1985**, *24*, 2253.

(8) Humphry-Baker, R.; Lilie, J.; Grätzel, M. *J. Am. Chem. Soc.* **1982**, *104*, 422.

(9) Bahnemann, D. W.; Bockelmann, D.; Goslich, R. In *Solar Energy Materials* Elsevier Science Publishers B.V.: North-Holland, 1991; ; pp 564.

(10) Fox, M. A.; Dulay, M. T. *Chem. Rev.* **1993**, *93*, 341.

(11) Pelizzetti, E.; Serpone, N., Eds. *Homogeneous and Heterogeneous Photocatalysis*; D. Reidel Publishing Company: Dordrecht, 1986.

(12) Schiavello, M., Ed. *Photoelectrochemistry, Photocatalysis and Photoreactors*; D. Reidel Publishing Company: Dordrecht, 1985.

(13) Schiavello, M., Ed. *Photocatalysis and Environment: Trends and Applications*; Kluwer Academica Publishers: Dordrecht, 1988.

(14) Serpone, N.; Pelizzetti, E., Eds. *Photocatalysis: Fundamentals and Applications*; John Wiley & Sons: New York, 1989.

(15) Brus, L. *Appl. Phys. A.* **1991**, *53*, 465.

(16) Weller, H. *Adv. Mater.* **1993**, *5*, 88.

(17) Grätzel, M. *Nature* **1991**, *349*, 740.

(18) Weller, H. *Angew. Chem.* **1993**, *32*, 41.

(19) Henglein, A. *T. Curr. Chem.* **1988**, *143*, 113.

(20) Kamat, P. V. *Chem. Rev.* **1993**, *93*, 267.

(21) Martin, S. T.; Herrmann, H.; Choi, W.; Hoffmann, M. R. *Trans. Far. Soc.* **1994**, *in press*,

(22) Martin, S. T.; Herrmann, H.; Hoffmann, M. R. *Trans. Far. Soc.* **1994**, *in press*,

(23) Lewis, N. S. *Annu. Rev. Phys.* **1991**, *42*, 543.

(24) Gerischer, H. In *Physical Chemistry: An Advanced Treatise*; H. Eyring, Ed.; Academic Press: London, 1970; ch. 5; Vol. IXA/Electrochemistry; pp 463.

(25) Bond, G. C.; Tahir, S. F. *Applied Catalysis* **1991**, *71*, 1.

(26) Heller, H. G.; Langan, J. R. *J. Chem. Soc. Perkin Trans.* **1981**, *2*, 341.

(27) *Powder Diffraction File, Sets 21-22*; JCPDS: Swarthmore, 1980; Vol. PD1S-22iRB, pp 21-1272.

(28) *International Tables for Crystallography: Space-Group Symmetry*; Second ed.; Hahn, T., Ed.; D. Reidel Publishing Company: Dordrecht, 1987; Vol. A.

(29) Cullity, B. D. *Elements of X-Ray Diffraction;* 2nd ed.; Addison-Wesley: Reading, 1978, pp 102.

(30) Beattie, I. R.; Gilson, T. R. *J. Chem Soc. (A)* **1969**, 2322.

(31) Deo, G.; Turek, A. M.; Wachs, I. E.; Machej, T.; Haber, J.; Das, N.; Eckert, H.; Hirt, A. M. *Applied Catalysis A: General* **1992**, *91*, 27.

(32) Kormann, C.; Bahnemann, D. W.; Hoffmann, M. R. *J.Phys.Chem.* **1988**, *92*, 5196.

(33) Bond, G. C.; Sarkany, A. J.; Parfitt, G. D. *J. Catalysis* **1979**, *57*, 476.

(34) Inomata, M.; Mori, K.; Miyamoto, A.; Ui, t.; Murakami, Y. *J. Phys. Chem.* **1983**, *87*, 754.

(35) Busca, G.; Centi, G.; Marchetti, L.; Trifiro, F. *Langmuir* **1986**, *2*, 568.

(36) Cavani, F.; Centi, G.; Parrinello, F.; Trifiro, F. In *Preparation of Catalysts IV*; B. Delmon, P. Grange, P. A. Jacobs and G. Poncelet, Ed.; Elsevier Science Publishers B.V.: Amsterdam, 1987; ; pp 227.

(37) Cavani, F.; Centi, G.; Foresti, E.; Trifiro, F.; Busca, G. *J. Chem. Soc. Faraday Trans. 1* **1988**, *84*, 237.

(38) Gallay, R.; van der Klink, J. J.; Moser, J. *Phys. Rev. B* **1986**, *34*, 3060.

(39) Rusiecka, M.; Grzybowska, B.; Gasior, M. *Applied Cat.* **1984**, *10*, 101.

(40) Wachs, I. E.; Saleh, R. Y.; Chan, S. S.; Cherisch, C. C. *Applied Catalysis* **1985**, *15*, 339.

(41) Gasior, I.; Gasior, M.; Grzybowska, B.; Kozlowski, R.; Sloczynski, J. *Bull. Acad. Pol. Sci., Ser. Sci. Chim.* **1979**, *27*, 829.

(42) Wachs, I. E.; Jehng, J. M.; Hardcastle, F. D. *Solid State Ionics* **1989**, *32/33*, 904.

(43) Latimer, W. M. *Oxidation Potentials*; Prentice-Hall, Inc.: Englewood Cliffs, 1952.

(44) Saleh, R. Y.; Wachs, I. E.; Chan, S. S.; Chersich, C. C. *J. Catalysis* **1986**, *98*, 102.

(45) Mizushima, K.; Tanaka, M.; Asai, K.; Iida, K. *AIP conf. Proc.* **1973**, *18*, 1044.

(46) Mizushima, K.; Tanaka, M.; Asai, A.; Iida, S.; Goodenough, J. B. *J. Phys. Chem. Solids.* **1979**, *40*, 1129.

(47) Barbeni, M.; Pramauro, E.; Pelizzetti, E.; Brogarello, E.; Grätzel, M.; Serpone, N. *Nouv. J. Chemie* **1984**, *8*, 547.

(48) Matthews, R. W. *Wat. Res.* **1986**, *20*, 569.

(49) Matthews, R. W. *J. Catalysis* **1988**, *111*, 264.

(50) Al-Sayyed, G.; D'Oliveira, J. C.; Pichat, P. *J. Photochem. Photobiol. A: Chem.* **1991**, *58*, 99.

(51) Mills, A.; Morris, S.; Davies, R. *J. Photochem. Photobiol. A: Chem.* **1993**, *70*, 183.

(52) Mills, A.; Morris, S. *J. Photochem. Photobiol. A: Chem* **1993**, *71*, 75.

(53) Mills, A.; Morris, S. *J. Photochem. Photobiol. A: Chem* **1993**, *71*, 285.

(54) Stafford, U.; Gray, K.; Kamat, P.; Varma, A. *Chem. Phys. Lett.* **1993**, *205*, 55.

(55) Frei, H.; Fitzmaurice, D. J.; Grätzel, M. *Langmuir* **1990**, *6*, 198.

(56) Tunesi, S.; Anderson, M. A. *Langmuir* **1992**, *8*, 487.

(57) Södergren, S.; Hagfeldt, A.; Olsson, J.; Lindquist, S. *J. Phys. Chem.* **1994**, *98*, 5552.

(58) Vogel, R.; Hoyer, P.; Weller, H. *J. Phys. Chem.* **1994**, *98*, 3183.

(59) Vinodgopal, K.; Hotchandani, S.; Kamat, P. V. *J. Phys. Chem.* **1993**, *97*, 9040.

(60) Redmond, G.; Fitzmaurice, D.; Grätzel, M. *J. Phys. Chem.* **1993**, *97*, 6951.

(61) Haque, I. U.; Rusling, J. F. *Chemosphere* **1993**, *26*, 1301.

(62) Morrison, S. R. *Electrochemistry at Semiconductor and Oxidized Metal Electrodes*; Plenum Press: New York, 1980.

(63) Mériaudeau, P.; Vedrine, J. C. *Nouv. J. Chim.* **1977**, *2*, 133.

(64) Davidson, A.; Che, M. *J. Phys. Chem.* **1992**, *96*, 9909.

(65) Micic, O. I.; Zhang, Y.; Cromack, K. R.; Trifunac, A. D.; Thurnauer, M. C. *J. Phys. Chem.* **1993**, *97*, 7277.

(66) Howe, R. F.; Grätzel, M. *J. Phys. Chem.* **1985**, *89*, 4495.

(67) Howe, R. F.; Grätzel, M. *J. Phys. Chem.* **1987**, *91*, 3906.

	Quantum Efficiency (%)		
Calcination Temp (°C)	TiO_2	1% V-doped TiO_2	Crystal Size (nm)
25	0.09	0.04	1 to 4
200	0.14	0.04	2 to 6
400	0.23	0.05	4 to 17
600	0.11	0.00	n/a
800	0.03	0.00	n/a

Table 1: Quantum efficiencies for the degradation of 4-chlorophenol. (Irradiation conditions reported in Figure 1.)

	Intermediates Formed Maximum Concentration (μM)					
	TiO_2			1% V-doped TiO_2		
Calcination Temperature (°C)	HQ	BQ	CC	HQ	BQ	CC
25	1.5	4.0	0.0	2.5	0.0	0.0
200	2.0	8.0	0.0	3.0	0.0	0.0
400	9.0	3.0	0.0	4.0	0.0	0.0
600	7.0	0.0	0.6	0.0	0.0	0.0
800	3.0	0.0	0.2	0.0	0.0	0.0

Table 2: Intermediates formed during the photo-degradation of 4-chlorophenol in the presence of TiO_2. (HQ = hydroquinone, BQ = 1,4-benzoquinone, and CC = 4-chlorocatechol.)

Calcination Temp., °C	Lattice Doping	Mass Loss (%)	Crystal Size (nm)		Phase	Reflectivity Onset (nm)	Particle Size (µm)		
			Minimum	Maximum		[1]	Mean	σ	%N [2]
25	none	0	1.0 ± 0.5	4.0 ± 0.5	anatase [3]	382	58	19	31
200	none	14	2.0 ± 0.5	6.0 ± 0.5	anatase	387	43	15	35
400	none	20	4.0 ± 0.5	17.0 ± 0.5	anatase	397	46	18	31
600	none	22	2.5 ± 1.0	11.0 ± 1.0	anatase [4]	412	45	17	36
			18 ± 2	200 ± 2	rutile [4]				
800	none	23	26 ± 2	268 ± 2	rutile	412	n/a	n/a	n/a
25	1% V	0	1.0 ± 0.5	3.0 ± 0.5	anatase	n/a	46	10	35
200	1% V	14	2.0 ± 0.5	4.0 ± 0.5	anatase	n/a	42	13	51
400	1% V	19	3.0 ± 0.5	22.0 ± 0.5	anatase	n/a	47	16	56
600	1% V	21	14 ± 1	155 ± 1	rutile	n/a	50	17	60
800	1% V	23	85 ± 3	374 ± 3	rutile	n/a	43	11	64

[1] $\lambda_{r.o.} \equiv \lambda_{\%R = 0.5(\%R_{max} - \%R_{min})}$

[2] $\%N = \dfrac{N_{A>500\mu m^2}}{N_{Total}} \times 100$

[3] ED analysis shows no amorphous phase.

[4] Bimodal distribution.

Table 3: Physical characterization of TiO$_2$ particles.

	Vanadium Concentration		
	Atomic Percent of Vanadium Released		
Calcination Temperature (°C)	Acid Extraction	Base Extraction	Complete Dissolution
25	0.16	0.08	0.43
200	0.26	0.10	0.39
400	0.32	0.23	0.39
600	0.11	0.09	0.47
800	0.07	0.04	0.43

Table 4: Vanadium speciation in doped TiO_2.

Calcination Temp. (°C)	g_1	g_2	g_3	A_1	A_2	A_3	Signal Intensity
25	1.922	1.956		182	55		40
200	1.923	1.967	1.940	159	54	44	4
400	1.923	1.967	1.940	159	54	44	8
600	1.941	1.906	1.899	152	31	51	625
800	1.941	1.906	1.899	152	31	51	770

Table 5: g-Factors and hyperfine splitting constants (G) derived for vanadium-doped TiO_2 spectra (cf. Figure 6).

g_z	g_x	g_y	A_z	A_x	A_y	Assignment	ref
1.880	1.925					Ti(III)$_{surf}$ aq colloid	3
1.911	1.983		154	55		V(IV) in V_2O_5	63
1.923	1.986		168	62		V(IV) in V_2O_5	64
1.932	1.960		175	53		V(IV)$_{inter}$ anatase	3
1.940	1.986	1.993	123	49	64	V(IV)$_{inter}$ rutile	64
1.956	1.914	1.912	156	35	49	V(IV)$_{sub}$ rutile	3
1.956	1.913	1.915	153	48	35	V(IV)$_{sub}$ rutile	64
1.957	1.988					Ti(III)$_{inter}$ aq colloid	66
1.988	1.892					Ti(III)$_{aq}$	3
2.007	2.014	2.024				trapped hole in TiO_2	65
2.021	2.009	2.001				$O_2^{\cdot -}$ on anatase	67

Table 6: g-Factors and hyperfine splitting constants (G) reported for various paramagnetic species.

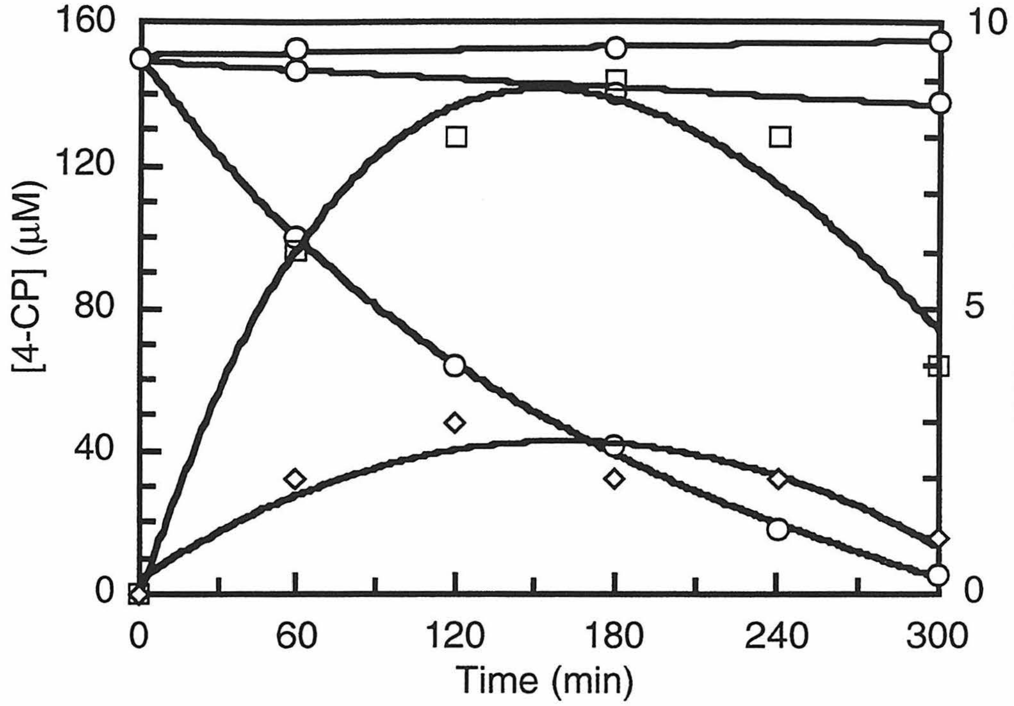

Figure 1: (a) Disappearance of 4-chlorophenol (O) and the appearance of hydroquinone (□) and benzoquinone (◇) as a function of irradiation time in the presence of undoped TiO_2 calcined at 400 °C. (b) No light. (c) No TiO_2. ($I = 200$ μM min^{-1}, pH = 3.9, O_2 saturated, $[TiO_2] = 1.0$ g/L, $\lambda = 324 \pm 5$ nm.)

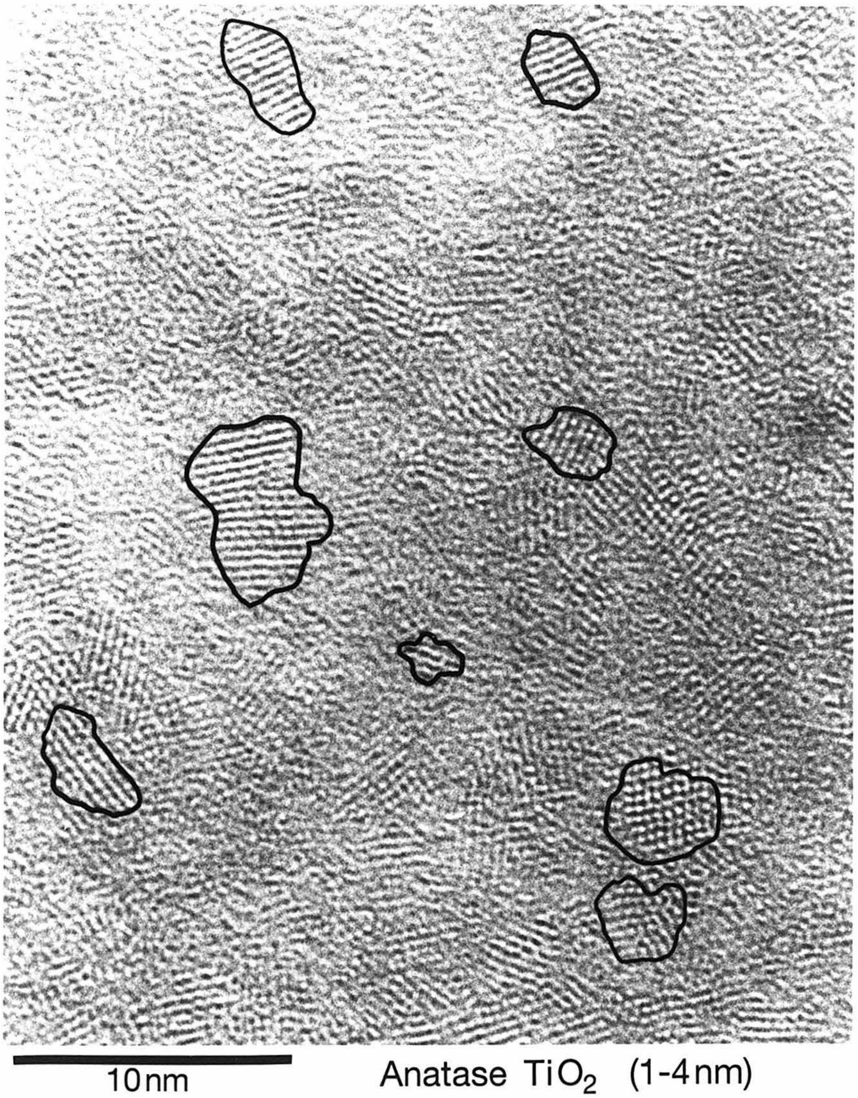

Figure 2a: Transmission electron micrographs of vanadium-doped TiO_2 calcined at 25 °C (a, b) and 800 °C (c).

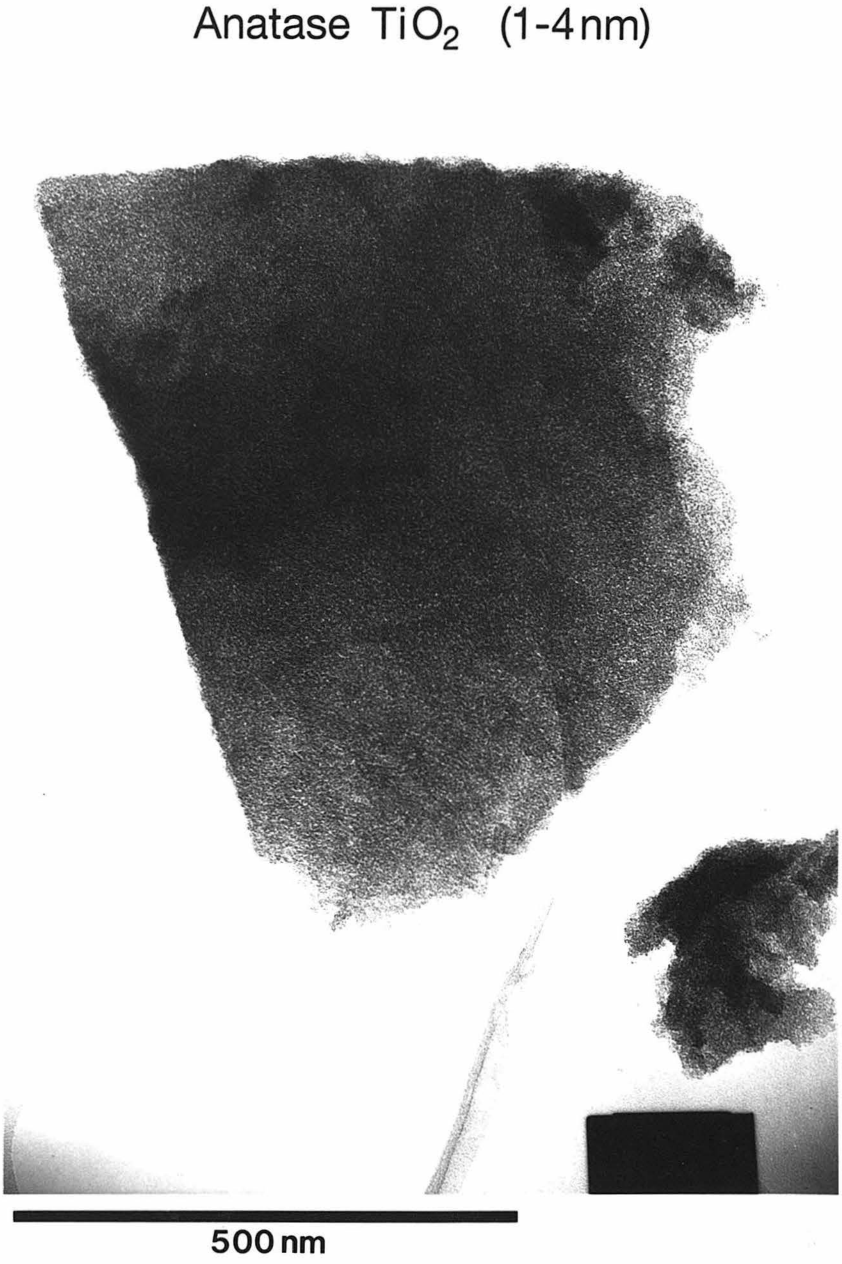

Figure 2b: Transmission electron micrographs of vanadium-doped TiO_2 calcined at 25 °C (a, b) and 800 °C (c).

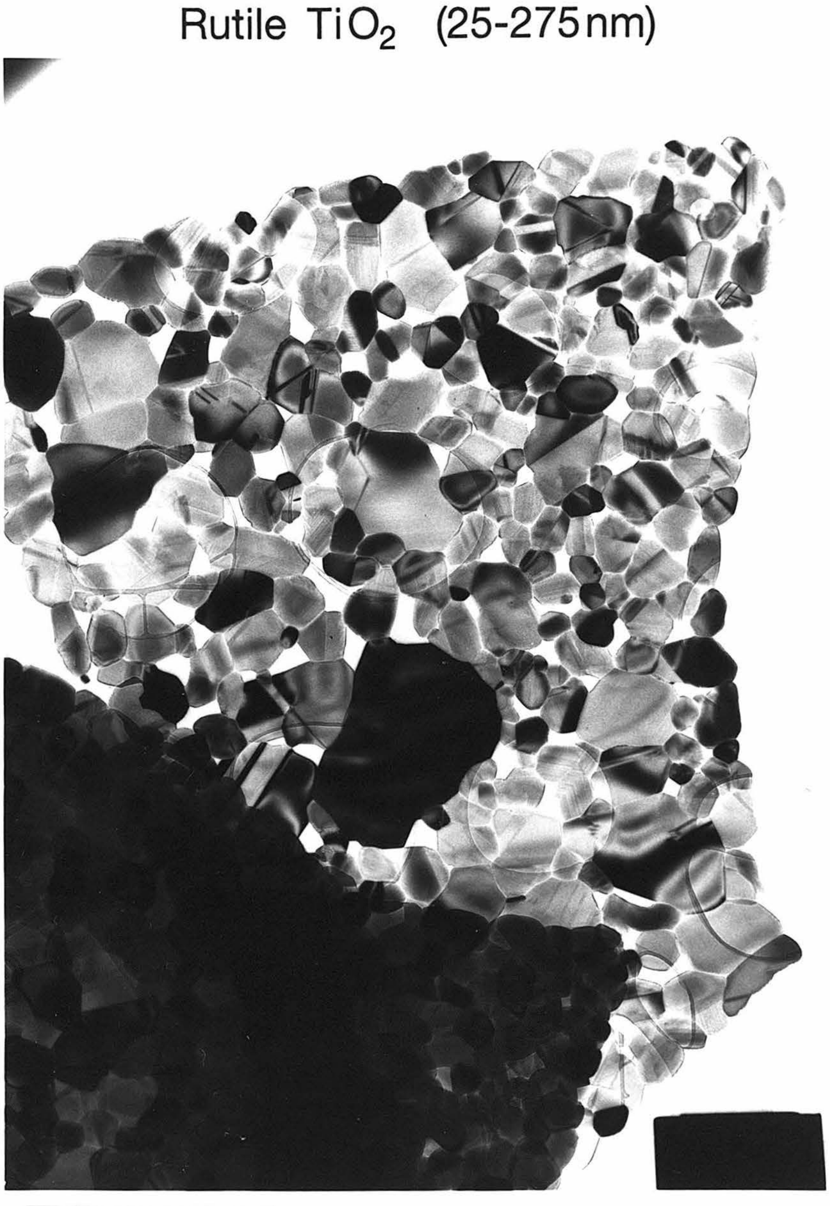

Figure 2c: Transmission electron micrographs of vanadium-doped TiO_2 calcined at 25 °C (a, b) and 800 °C (c).

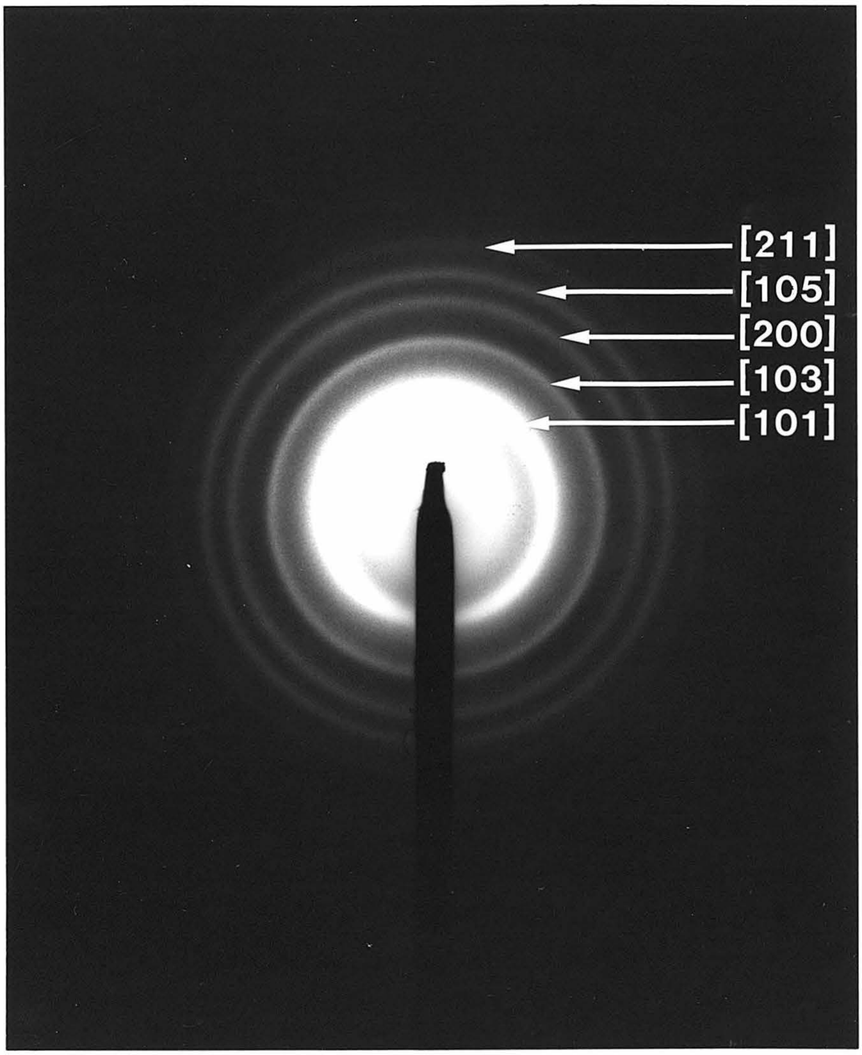

1% V-doped Anatase TiO_2 (1-3 nm)

Figure 3: Electron diffraction patterns of vanadium-doped TiO_2 calcined at 25 °C.

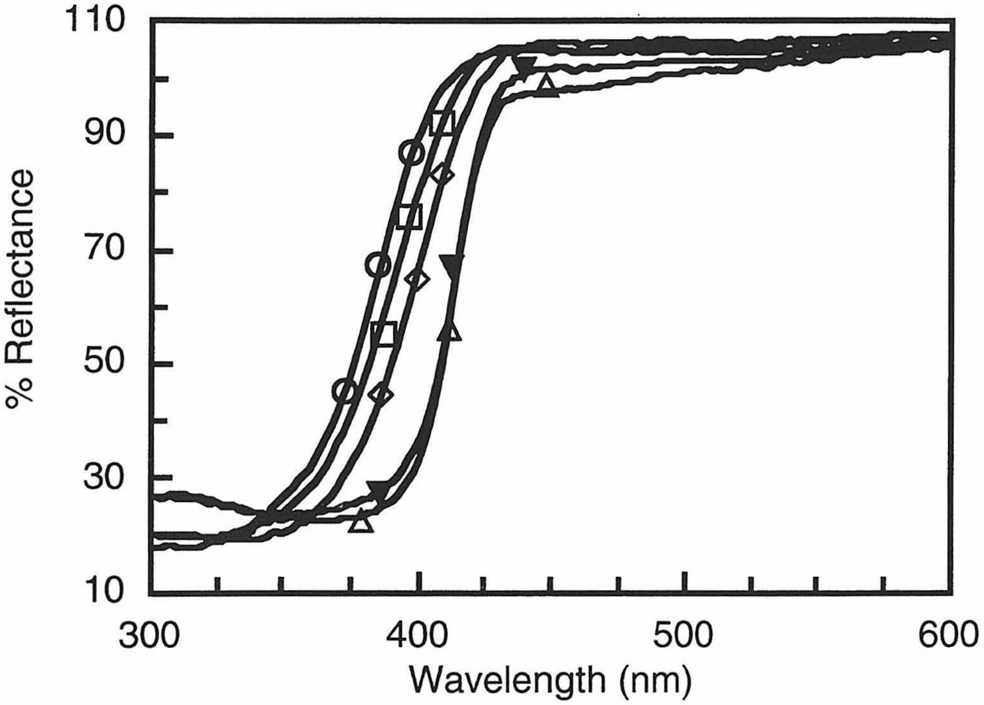

Figure 4: UV/Vis reflection spectra of undoped TiO_2 calcined at 25 °C (○), 200 °C (□), 400 °C (◇), 600 °C (▽), and 800 °C (△).

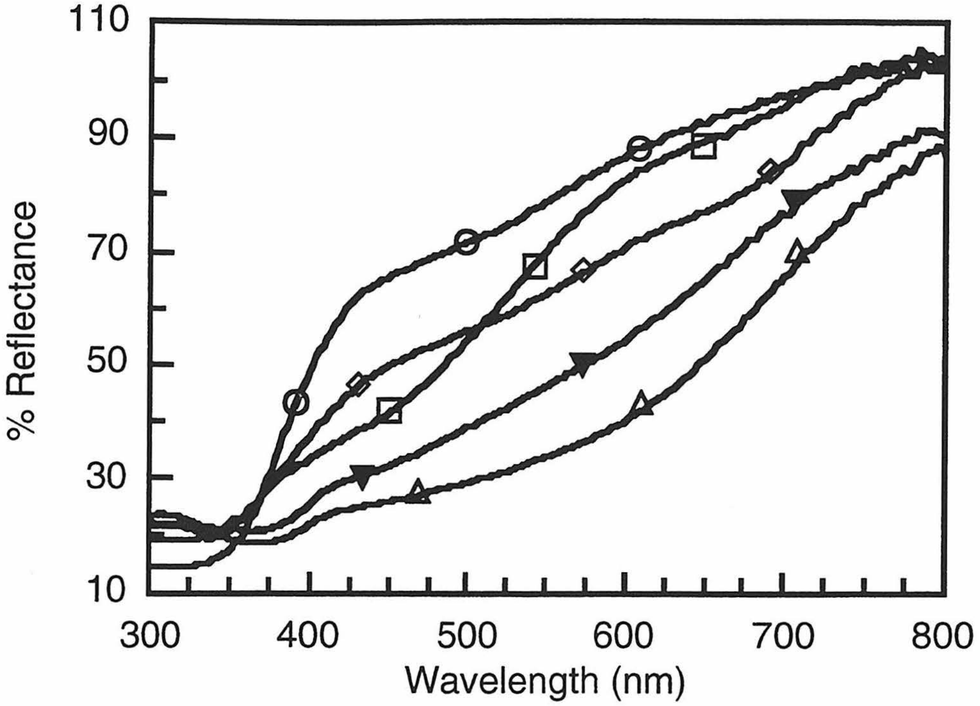

Figure 5: UV/Vis reflection spectra of vanadium-doped TiO_2 calcined at 25 °C (O), 200 °C (□), 400 °C (◇), 600 °C (▽), and 800 °C (△).

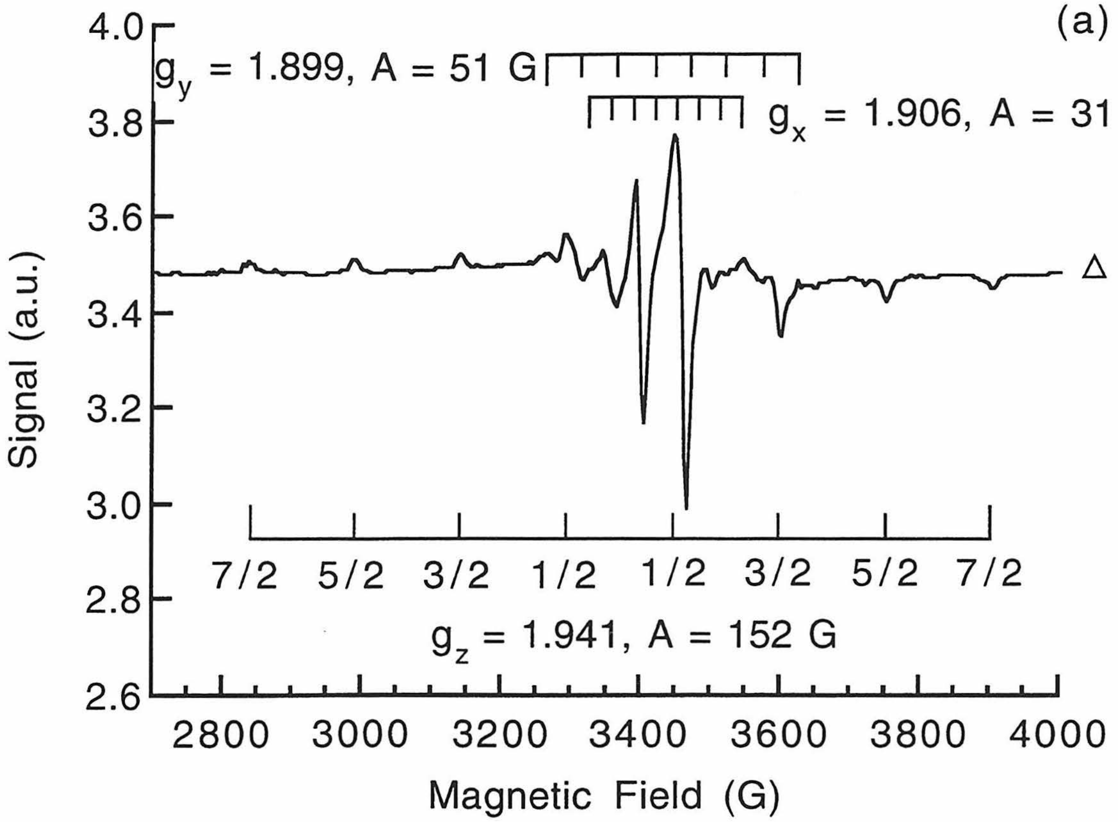

Figure 6a: EPR spectra recorded at 77 K of vanadium-doped TiO_2. (a) g-Factor and hyperfine splitting constant assignments for sample heat-treated at 800 °C. (b) Effect of calcination temperature at 25 °C (O), 200 °C (□), 400 °C (◇), 600 °C (▽), and 800 °C (△). The signal intensities are shown as $I = (\text{gain})^{-1} \times 10^4$.

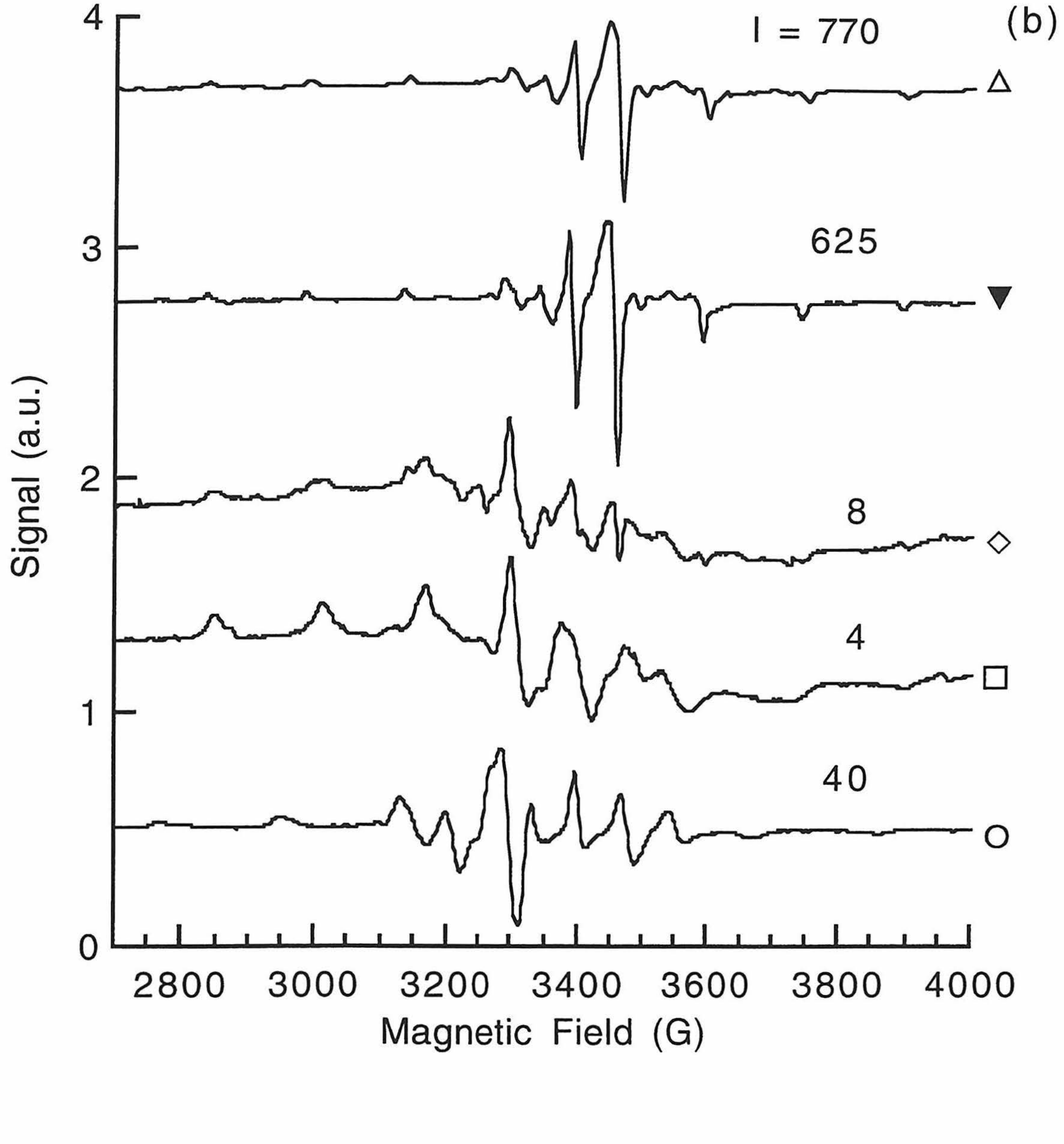

Figure 6b: EPR spectra recorded at 77 K of vanadium-doped TiO_2. (a) g-Factor and hyperfine splitting constant assignments for sample heat-treated at 800 °C. (b) Effect of calcination temperature at 25 °C (○), 200 °C (□), 400 °C (◇), 600 °C (▽), and 800 °C (△). The signal intensities are shown as $I = (\text{gain})^{-1} \times 10^4$.

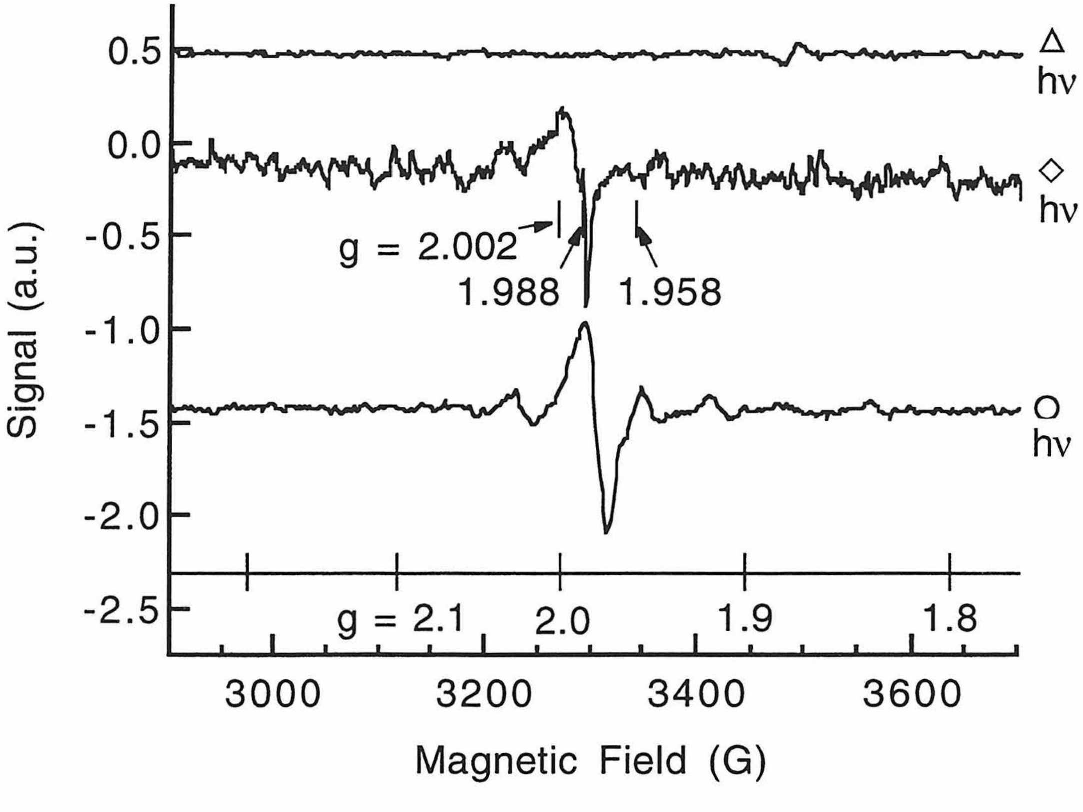

Figure 7: EPR difference spectra due to CW irradiation of vanadium-doped TiO_2 calcined at 25 °C (O), 400 °C (◇), and 800 °C (Δ) (77 K, 450 W Hg lamp, $310 < \lambda < 380$ nm using 7-60-1 Kopp bandpass filter).

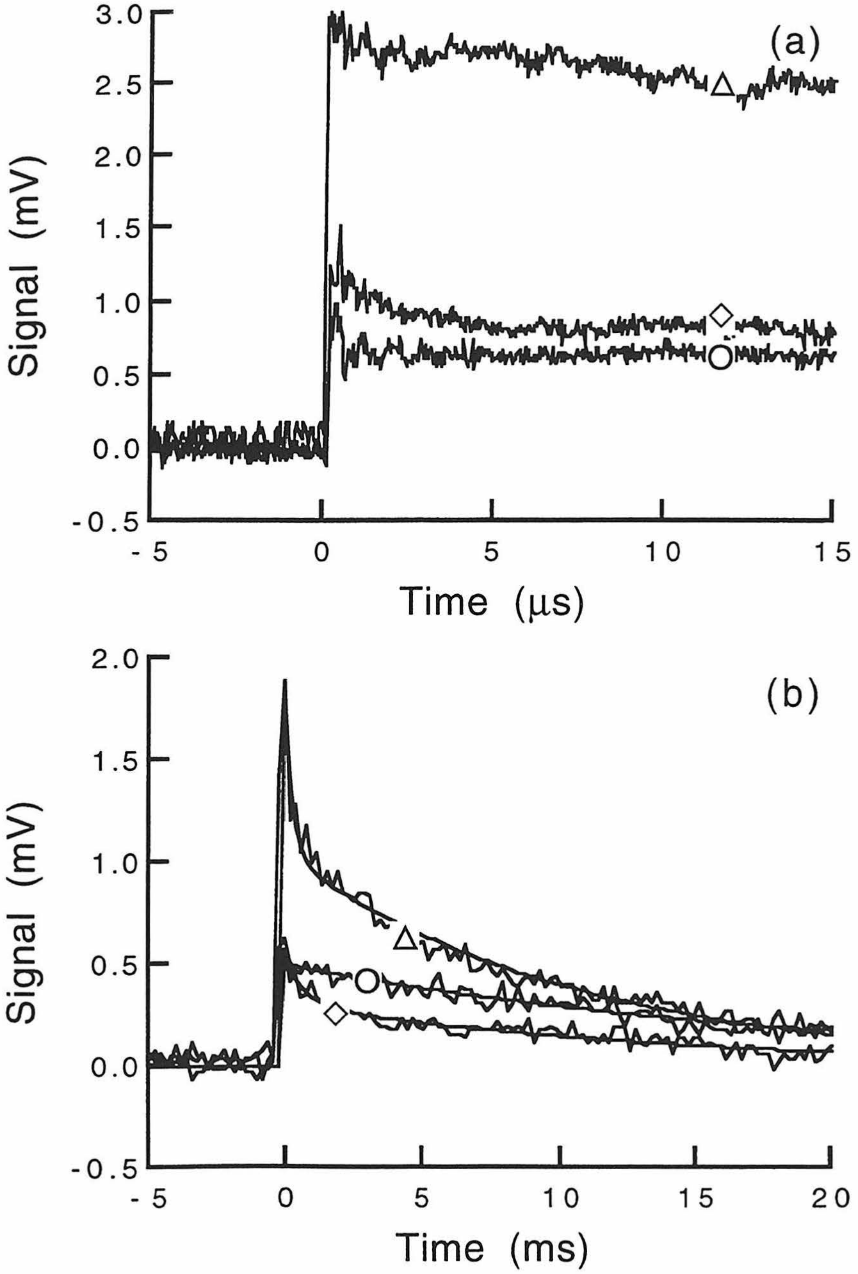

Figure 8: Time-resolved microwave conductivity of vanadium-doped TiO$_2$ calcined at 25 °C (○), 400 °C (◇), and 800 °C (△).

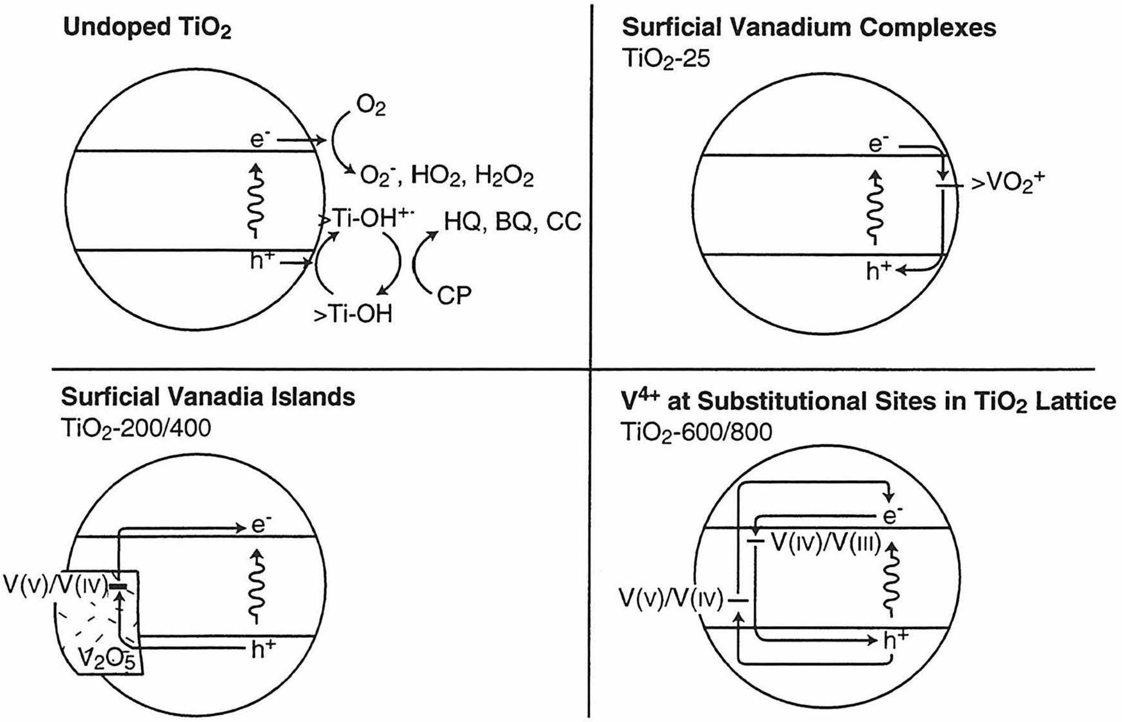

Figure 9: Charge-carrier dynamics of vanadium-doped TiO_2.

Chapter 6

Chemical Mechanism of Inorganic Oxidants in the TiO_2/UV Process: Increased Rates of Degradation of Chlorinated Hydrocarbons

[The text of this chapter has been accepted for publication as Martin, S.T., Lee, A.T., and Hoffmann, M.R., *Environmental Science and Technology*, 1995.]

Abstract

Particulate suspensions of TiO_2 irradiated with UV light at wavelengths shorter than 385 nm catalyze the autooxidation of chlorinated hydrocarbons such as 4-chlorophenol (4-CP). The addition of oxyanion oxidants such as ClO_2^-, ClO_3^-, IO_4^-, $S_2O_8^{2-}$, and BrO_3^- increases the rate of photodegradation of 4-CP in the following order: $ClO_2^- > IO_4^- > BrO_3^- > ClO_3^-$. In the absence of TiO_2, ClO_3^- shows no photoreactivity towards 4-CP, while HSO_5^- and MnO_4^- exhibit rapid thermal reactivity with 4-CP. BrO_3^- appears to increase photoreactivity by scavenging conduction-band electrons and reducing charge-carrier recombination. With ClO_3^- as an oxidant, the degradation of 4-CP appears to follow three concurrent pathways. Kinetic equations for the rate of degradation of 4-CP as a function of [4-CP], [ClO_3^-], [O_2], and the light intensity are derived from a proposed mechanism.

Introduction

Under normal conditions, TiO_2 catalyzes the oxidation of chlorinated hydrocarbons in the presence of UV radiation at photon energies equal to or greater than the band-gap energy of 3.2 eV (λ = 385 nm) according to the following stoichiometry:[1]

$$C_xH_yCl_z + \left(x + \frac{y-z}{4}\right)O_2 \xrightarrow[h\nu,\ TiO_2]{} x\,CO_2 + z\,H^+ + z\,Cl^- + \left(\frac{y-z}{2}\right)H_2O \qquad (1)$$

The addition of inorganic oxidants such as HSO_5^-, ClO_3^-, IO_4^-, and BrO_3^- increases the rate of degradation of chlorinated hydrocarbons in slurries of TiO_2 irradiated with ultraviolet light.[2-5] The oxidants are proposed to increase quantum efficiencies partially by inhibiting electron-hole pair recombination through scavenging conduction-band electrons at the surface of TiO_2 and partially by augmenting the TiO_2/UV process through thermal and photochemical oxidations in the bulk solution. However, mechanistic studies on the role of the oxyanions in the TiO_2/UV process have not previously been carried out.

In this paper we attempt to elucidate the detailed mechanism by which oxyanion oxidants serve as efficient electron acceptors in TiO_2/UV oxidations. In this regard, we have studied the photo-oxidation of 4-chlorophenol (4-CP) in suspensions of Degussa P25. The choice of electron-donating substrate and photocatalyst was made because they have been widely studied previously[6-8] and are considered a standard reaction system for the evaluation of the TiO_2/UV process.[9-11]

Experimental Section

Photoreactivity Studies. Irradiations were performed with a 1000 W Xe arc lamp (Oriel Corp.) at 25 °C according to previously described procedures.[12-14] Neutral density filters (Oriel) were used to adjust the light intensity, which was found to be 2.1 mEin min^{-1} without attenuation. A bandpass filter (Corning 7-60-1, $320 < \lambda < 380$ nm) was used during the actinometry to avoid bleaching of Aberchrome 540.

Aqueous slurries (24 mL) of TiO_2 (1.0 g/L), 4-chlorophenol (100 μM) or KI (1 mM), and a particular oxidant (typically 100 mM) were prepared. The stirred aqueous slurries were bubbled with humid O_2 or N_2 (10 ml min^{-1}) for 90 min prior to and (for 4-CP only) during the irradiation to maintain oxygenated or deoxygenated conditions, as appropriate. The sparging of the KI slurry was followed by the introduction of a static Ar atmosphere under positive pressure, which prevented the volatilization of I_2 during the irradiation and excluded O_2 from the system. At periodic time intervals, aliquots (100 μL) of the slurry were extracted through 0.45 μm syringe filters. Nylon filters (Nalgene) were used for organic analysis and Teflon filters (Gelman) were used for I_3^- analysis.

Analysis. Separation and quantification of organic intermediates was accomplished by HPLC (Hewlett Packard Series II 1090 Liquid Chromatograph). Compounds were separated on a reverse-phase column (Hewlett-Packard 5 μm ODS Hypersil) using a gradient elution program (100% H_3PO_4 buffer (pH 3.0) to 80:20 H_3PO_4:CH_3CN). Diode array detection at 224 nm and 280 nm was used for quantification. Production of I_3^- was quantified spectrophotometrically (HP 8452A) using $\varepsilon(352\text{ nm}) = 26{,}400\ M^{-1}\ cm^{-1}$.[15]

Results

The time series data of the photooxidation experiments (i.e., 4-CP concentration versus irradiation time) typically consist of five data points and are reduced by calculating apparent quantum efficiencies, Φ, as follows: $\Phi = \frac{|d[4CP]/dt|}{I_{incident}}$ where d[4CP]/dt is the initial rate of disappearance of 4-CP and $I_{incident}$ is the incident light intensity determined by chemical actinometry. The apparent quantum efficiencies for the TiO_2/UV photooxidation of 4-CP in the presence of several oxidants are shown in Table 1. For irradiation in the absence of TiO_2, Φ decreases in the order $ClO_2^- > IO_4^- > BrO_3^- > ClO_3^-$. Of these, only ClO_3^- shows no direct photoreactivity with respect to 4-CP oxidation. ClO_2^-, IO_4^-, BrO_3^-, and ClO_3^- exhibit negligible dark reactivity at these concentrations whereas 0.1 M HSO_5^- and MnO_4^- are highly reactive in the absence of irradiation. In the presence of TiO_2, Φ increases and follows the same relative order of $ClO_2^- \sim IO_4^- > BrO_3^- > ClO_3^-$ over a pH range of 3 to 6.

Increasing the concentration of ClO_3^- from 10^{-3} to 1 M yields higher Φ values in deoxygenated slurries (Figure 1a, ○). No saturation effect is observed up to 1 M ClO_3^-. However, a minimum concentration of 10 mM ClO_3^- is necessary for a noticeable increase in Φ. The Φ values in the presence of ≤1 mM ClO_3^-, N_2 alone (i.e., 0 mM ClO_3^-), 0.1 M Cl^-, and 0.1 M ClO_4^- are essentially the same within experimental error (i.e., $\Phi(\times 10^4) = 2.6$). Hydroquinone and benzoquinone are the principal intermediates detected by HPLC. Ion chromatographic measurements indicate ClO_3^- is reduced to Cl^-

stoichiometrically with the loss of 4-CP; steady-state intermediates such as $HClO_2$ ($pK_a = 2$) or HOCl ($pK_a = 7.5$) are not detected.

In contrast to the deoxygenated slurries, increasing concentrations of ClO_3^- in the presence of oxygen yield lower Φ values (Figure 1a, □). However, Φ_{min} in the presence of oxygen (i.e., $\Phi(\times 10^4) = 15$ for 0.5 M ClO_3^-) is 2.0 times greater than Φ_{max} in the absence of oxygen (i.e., $\Phi(\times 10^4) = 7.5$ for 1 M ClO_3^-).

In the absence of TiO_2 and dioxygen, a homogeneous photoreaction occurs between BrO_3^- and 4-CP (data not shown). The Φ values increase steadily with $[BrO_3^-]$ from 1 to 250 mM. The addition of O_2 has no apparent effect. The maximum Φ value due to homogeneous photoreactions, Φ_{homo}, is 0.13×10^{-2} for the range of concentrations studied. In the presence of TiO_2, both heterogeneous and homogeneous photoreactions occur (Figure 1b, ◇). The smallest Φ value, Φ_{hetero}, is 1.0×10^{-2}. Because $\Phi_{hetero} \gg \Phi_{homo}$ under our experimental conditions, we conclude that homogeneous photoreactions are negligible to a first approximation in the discussion of the mechanism of BrO_3^- in heterogeneous photo-oxidations. The addition of O_2 to the TiO_2/BrO_3^- suspension has no apparent effect under our experimental conditions.

Higher quantum efficiencies are often observed at lower incident light intensities due to decreased charge-carrier recombination rates.[12-13] The effect of light intensity on Φ follows this trend (Figure 2). The slope $|\partial\Phi/\partial I|$ follows the order: {no ClO_3^-, O_2} > {0.1 M ClO_3^-, no O_2} > {no ClO_3^-, no O_2} where I is the light intensity.

The heterogeneous oxidation of I^- to I_3^- catalyzed by TiO_2 has been studied previously.[15-19] In this study, we also investigated the formation of I_3^- by TiO_2/UV in the presence of ClO_3^- and/or O_2 as shown in Figure 3. In the absence of TiO_2, no I_3^- is formed. In the presence of TiO_2, an initial rapid formation of I_3^- from the oxidation of I^- is followed by a continuous slow formation according to the order: {no ClO_3^-, O_2} > {0.1 M ClO_3^-, O_2} > {no ClO_3^-, no O_2} ~ {0.1 M ClO_3^-, no O_2}. In addition, the yield of I_3^- in the oxygenated slurry is decreased by the addition of ClO_3^- as was seen in the case of 4-CP. However, unlike the 4-CP experiments, the initial rate of I_3^- formation in deoxygenated slurries is independent of the presence of ClO_3^-.

Discussion

The quantum efficiencies obtained for the degradation of 4-CP under a set of consistent experimental conditions ($I = 2.1$ mEin min^{-1}, $\lambda > 340$ nm, deoxygenated, $[TiO_2] = 1$ g/L, pH unadjusted, T = 25 °C, $[4\text{-CP}]_0 = 100$ μM) are given in Table 1. UV-absorption by BrO_3^-, IO_4^-, and ClO_2^- results in direct photochemistry. Dark oxidation proceeds rapidly at 25 °C only for HSO_5^- and MnO_4^-, though all of the oxidants are thermodynamically capable of degrading 4-CP (E° = 0.80 V vs. NHE).[6,20] The absence of photochemistry and dark chemistry in a solution of ClO_3^- and 4-CP suggested that ClO_3^- was the appropriate inorganic oxidant for initial mechanistic studies. Although ClO_3^- degrades 4-CP more slowly (Table 1) than the other oxyanions, complications in the interpretation of our results were avoided because parallel reaction pathways are not available (cf. IO_4^-/4-CP/hn and IO_4^-/4-CP/hn/TiO_2). In addition, the mechanism of BrO_3^- is also studied because the quantum efficiency (Table 1) is relatively high and the ratio between the heterogeneous and homogeneous photoreactivities ($\Phi_{hetero}:\Phi_{homo}$ » 1) is large enough that the effects of the latter may be assumed to be negligible.

Conduction-Band Electron Scavengers. The positive monotonic relationship seen in Figures 1a (O) and 1b (◇) between the Φ values and the concentrations of ClO_3^- and BrO_3^- in deoxygenated TiO_2 suspensions supports the hypothesis that the oxyanions scavenge conduction-band electrons, reduce charge-pair recombination, and promote the oxidation of 4-CP by valence-band holes. The relevant reduction potentials are as follows:[21-22]

$$ClO_3^- + 2\,H^+ + e^- \rightarrow ClO_2 + H_2O \qquad E° = 1.15\text{ V} \qquad (2)$$

$$ClO_3^- + 6\,H^+ + 6\,e^- \rightarrow [ClO_2^-, HOCl] \rightarrow Cl^- + 3\,H_2O \qquad E° = 1.44\text{ V} \qquad (3)$$

$$BrO_3^- + 2\,H^+ + e^- \rightarrow BrO_2 + H_2O \qquad E° = 1.15\text{ V} \qquad (4)$$

$$BrO_3^- + 6\,H^+ + 6\,e^- \rightarrow [BrO_2^-, HOBr] \rightarrow Br^- + 3\,H_2O \qquad E° = 1.44\text{ V} \qquad (5)$$

According to this hypothesis, an additional electron scavenger such as O_2 should further reduce charge-pair recombination and thus increase the rate of 4-CP degradation. In fact, even at the lowest BrO_3^- concentrations (1 mM), O_2 has no apparent effect on the observed rates of degradation (Figure 1b). The negligible effect of O_2 suggests BrO_3^- scavenges conduction-band electrons more efficiently than O_2.

ClO_3^-, on the other hand, reduces photoreactivity in the presence of O_2 (Figure 1a, □). Further experimental evidence is also inconsistent with the scavenging of conduction-band electrons by ClO_3^-: continuous production of Cl^- ions should occur in conjunction with the valence-band hole oxidation of water.[23-27] In fact, Cl^- ions are produced in an approximate stoichiometric relationship to the 4-CP degraded (corrected for Cl^- liberated from 4-CP).

Radical Scavengers. The negative correlation between [ClO_3^-] and the Φ values (Figure 1a, □) suggests ClO_3^- may scavenge active radical species that are generated in oxygenated slurries. The initial reductive event on TiO_2 is believed to be the formation of superoxide ion followed by the subsequent formation of active oxygen species, which contribute to the oxidation of 4-CP:[2,28]

$$O_2 + e^-_{c.b.} \rightarrow O_2^- \rightarrow\rightarrow\rightarrow O_2^-, HOO, HOOH, HOO^-, HO \qquad (6)$$

Scavenging of the active oxygen species by ClO_3^- should have the net effect of reducing photoreactivty. However, this possibility does not appear plausible due to apparent kinetic limitations[29-30] in the known generation pathways of ClO_3 ($E°(ClO_3/ClO_3^-) \approx 2.1$ V):[31]

$$\cdot OH + ClO_3^- \rightarrow OH^- + ClO_3\cdot \qquad k < 1 \times 10^6\ M^{-1}\ s^{-1} \qquad (7)$$

$$O_2^- + ClO_3^- \rightarrow \text{pdts} \qquad k < 0.003\ M^{-1}\ s^{-1} \qquad (8)$$

Mills et al.[10] determined that the photo-oxidation of 4-CP is best described by three parallel reaction pathways. One reaction pathway leads to an unstable intermediate that undergoes ring cleavage and subsequent rapid decarboxylation and dechlorination. The other two reaction pathways result in stable intermediates, including hydroquinone (HQ) and 4-chlorocatechol (4-CC). Consistent with this explanation and other previous mechanistic studies,[4,32-35] we propose the reactions in Table 2 and Figure 4 to explain the effects of ClO_3^- and the formation of the observed reaction intermediates.

The apparent reaction order for [ClO_3^-] is between 0.1 and 0.4, as calculated by the method of initial rates for the data in Figure 1. A fractional reaction order is consistent with the concurrent free-radical pathways.[36]

Reaction Mechanism. In the mechanism shown in Figure 4, 4-CP reacts with ·OH to form the 4-chlorodihydroxycyclodienyl radical (4-CD). After this initial hydroxylation, three parallel reaction pathways appear to be open. One pathway involves the reduction of 4-CD by a conduction-band electron to yield HQ and Cl^-. In the second pathway, 4-CD reacts with dioxygen to form the molecule 4-CDO. In the third pathway, the abstraction of an electron from 4-CD to yield 4-CD^+ is facilitated by ClO_3^-. 4-CD^+ is stabilized by a resonance interaction and by the strong electron-releasing capability of the -OH substituent at the 1-position.[37] The reactive intermediates 4-CDO and 4-CD^+ undergo further photo- and thermal reactions subsequent to their formation. Based on this mechanism, the reaction intermediates should be different depending upon the pathway which is dominant under a given set of experimental conditions. Previous work has shown that ClO_3^- affects the product mix obtained from the photooxidation of atrazine by the TiO_2/UV process.[2]

Kinetic Description. Our goal is to express Φ as a function of [O_2], [ClO_3^-], and [4CP] based upon the chemical reactions and kinetic equations shown in Table 2. The notation is as follows: ≡ indicates a surficial group, [≡X] is the surface concentration of species X (mol l^{-1}), e^- is a conduction-band electron, $\equiv e^-$ is a surficial electron (e.g., ≡Ti(III)), h^+ is a valence-band hole, $\equiv h^+$ is a surficial hole (e.g., $\equiv TiOH^{\cdot +}$), $\equiv O_2$ is adsorbed dioxygen (e.g., $\equiv Ti(IV)O_2$), $\equiv ClO_3^-$ is adsorbed chlorate (e.g., $\equiv Ti(IV)OClO_2^-$), 4-CP is 4-chlorophenol, 4-CD is the 4-

chlorodihydroxycyclodienyl radical, 4-CD$^+$ is the 4-chlorodihydroxycyclodienyl cation, [≡Ti(IV)]$_0$ is the concentration of ≡Ti(IV) without adsorption.

We make several assumptions as follows:

1. The reactions are not mass-transfer limited.
2. Adsorption and desorption of all species is fast with respect to reaction rates and the surface coverage may be described by a Langmuir-Hinshelwood adsorption isotherm.[38-41]
3. Double layer and surface charge effects are negligible with respect to the kinetic analysis.
4. 4-CP, O_2, and ClO_3^- compete for surficial Ti(IV) sites.
5. Reactions take place between surface-adsorbed species (Table 2).
6. The hydroquinone pathway (Figure 4) is not relevant to the kinetic description of the effets of O_2 and ClO_3^- on the oxidation of 4-CP.

The derivation begins by invoking charge-neutrality (eq T2.23) and the steady-state approximation (eq T2.22) to write eqs T2.20-21 as follows:

$$[\equiv e^-] - [\equiv h^+] = k_5\left(\frac{1}{k_6} - \frac{1}{k_7}\right) \tag{9}$$

Eq 9 simplifies to eq 10 when holes and electrons are localized at the same rate (i.e., $k_6 = k_7$):

$$[\equiv e^-] = [\equiv h^+] \tag{10}$$

The chemical reactions (eqs T2.5-8) shown in Table 2 and the approximation that $k_6 = k_7$ are not a complete representation of the charge-carrier dynamics; however, the essential elements are included.[12-13]

Applying the steady-state approximation (eq T2.22) to eq T2.19 and substituting eq 10 into the resulting expression, we can write:

$$0 = -k_4[\equiv h^+]^2 - k_1[\equiv h^+][\equiv 4\text{-CP}] + k_5 \tag{11}$$

Solving eq 11 for $[\equiv h^+]$ at low quantum efficiencies (i.e., $k_1[\equiv h^+][\equiv 4\text{-CP}] \ll k_4[\equiv h^+]^2$) yields the following equation:

$$[\equiv h^+] = \sqrt{k_5/k_4} \tag{12}$$

Application of the steady-state approximation to eq T2.17 yields:

$$[\equiv 4\text{-CD}] = \left(\frac{k_1[\equiv h^+][\equiv 4CP]}{k_{-1}[\equiv e^-] + k_2[\equiv ClO_3^-] + k_3[\equiv O_2]} \right) \tag{13}$$

Substituting eqs 10, 12, 13, Γ_1, Γ_2, and Γ_3 into eq T2.16 yields the following general equation for Φ the presence of both O_2 and ClO_3^-:

$$\Phi = \frac{|d[4CP]/dt|}{k_5} = \frac{k_1 K_3[\equiv Ti(IV)]^2[4CP](k_2K_2[ClO_3^-] + k_3K_1[O_2])}{k_{-1}k_5(1 + K_1[O_2] + K_2[ClO_3^-] + K_3[4CP])^2 + \sqrt{k_4k_5}[\equiv Ti(IV)](1 + K_1[O_2] + K_2[ClO_3^-] + K_3[4CP])(k_2K_2[ClO_3^-] + k_3K_1[O_2])} \tag{14}$$

Under our experimental conditions, KC(4-CP) = 0.013 (C = 100 μM and K = 1.3×10^2 M^{-1}).[11] Two estimates of KC(O_2) based upon kinetic measurements[11,42] are 4.4 (P = 1 atm and K = 4.4 atm^{-1})[11] and 130 (C = 1 mM and K = 1.3×10^5 M^{-1}).[43] FTIR-ATR measurements in our laboratory set an upper limit of K(ClO_3^-) $\ll$ 100 M^{-1}. If K(ClO_3^-) $\approx$ 10 M^{-1}, then KC varies from 1 to 10 for 0.1 to 1 M ClO_3^-, which is consistent with the kinetic observations in Figure 1 based upon a competition between O_2 and ClO_3^- for a common surface site (i.e., eq 14).

Special Cases. 1. Chlorate. When $[ClO_3^-] \gg [O_2]$ and [4-CP] is low, eq 14 is written as follows:

$$\Phi = \frac{k_1 k_2 K_2 K_3 [\equiv \mathrm{Ti(IV)}]^2 [4CP][ClO_3^-]}{k_{-1} k_5 \left(1 + K_2 [ClO_3^-]\right)^2 + \sqrt{k_4 k_5}\, k_2 K_2 [\equiv \mathrm{Ti(IV)}][ClO_3^-]\left(1 + K_2 [ClO_3^-]\right)} \qquad (15)$$

To evaluate the effect of $\Delta[ClO_3^-]$, we consider $\frac{\partial \Phi}{\partial [ClO_3^-]}$ as follows:

$$\frac{\partial \Phi}{\partial [ClO_3^-]} = \frac{k_1 k_{-1} k_2 k_5 K_2 K_3 [\equiv \mathrm{Ti(IV)}]^2 [4CP]\left(1 - \left(k_{-1} k_5 + \sqrt{k_4 k_5}\, k_2 [\equiv \mathrm{Ti(IV)}]\right) K_2^2 [ClO_3^-]^2 / k_{-1} k_5\right)}{\left[k_{-1} k_5 \left(1 + K_2 [ClO_3^-]\right)^2 + \sqrt{k_4 k_5}\, k_2 K_2 [\equiv \mathrm{Ti(IV)}][ClO_3^-]\left(1 + K_2 [ClO_3^-]\right)\right]^2} \qquad (16)$$

Thus, under high light intensity, $\frac{\partial \Phi}{\partial [ClO_3^-]} > 0$ when $[ClO_3^-] < K_2^{-1}$ as shown in eq 17:

$$[ClO_3^-] < \left[k_{-1} k_5 \big/ K_2^2 \left(k_{-1} k_5 + \sqrt{k_4 k_5}\, k_2 [\equiv \mathrm{Ti(IV)}]\right)\right]^{1/2} \approx \frac{1}{K_2} \qquad (17)$$

Hence, increasing $[ClO_3^-]$ at high light intensities increases Φ when [4-CP] is low and $[ClO_3^-] \gg [O_2]$. This behavior is shown in Figure 1. In addition, eq 17 predicts that at a sufficiently high $[ClO_3^-]$ (i.e., $[ClO_3^-] = K_2^{-1}$), $\Delta[ClO_3^-]$ should yield a decrease in Φ. The chemical interpretation is as follows: increasing $[ClO_3^-]$ favors the degradation pathway shown in Figure 4 (eq T2.3) but disfavors the pre-equilibria step (eq T2.15) by saturating the surface.

2. ***Light Intensity***. In consideration of light intensity, there are three regions included in our model. At high light intensities (i.e., k_5 is large), the second term in the denominator of eq 14 is negligible. In this case, Φ depends on the light intensity, I, as $\phi \propto I^{-1}$ and falls as the inverse of light intensity. At intermediate light intensities, the first term in the denominator is negligible and Φ falls as $I^{-1/2}$. We have previously reported the functional form of $\Phi(I)$.[12,43-44] The linear relation between quantum efficiency and light intensity shown in Figure 3 indicates that our experiments were conducted in the region of high light intensity approaching the limit $\Phi \propto I^{-1}$. At low light intensities, eq 12 fails because high quantum efficiencies are obtained.

3. ***Oxygen***. When $[O_2] \gg [ClO_3^-]$ and [4-CP] is low, analogues to eqs 15-17 result due to the symmetry of eq 16 with respect to O_2 and ClO_3^-. Hence, at high light intensities, increased $[O_2]$ yields increases in Φ when [4-CP] is low and $[O_2] \gg [ClO_3^-]$. This behavior has been observed previously.[11]

4. ***4-Chlorophenol***. When $[O_2] \gg [ClO_3^-]$ and [4-CP] is high, eq 14 is written as follows:

$$\Phi = \frac{k_1 k_3 K_1 K_3 [\equiv \mathrm{Ti(IV)}]^2 [4CP][O_2]}{k_{-1} k_5 \left(1 + 2K_3[4CP] + (K_3[4CP])^2\right) + \sqrt{k_4 k_5} k_3 K_1 [\equiv \mathrm{Ti(IV)}](1 + K_3[4CP])[O_2]} \tag{18}$$

The saturation effect of [4-CP] has been investigated previously and obeys a Langmuir-Hinshelwood isotherm.[11] Eq 18 reduces to the L-H form when $k_0 = k_1[\equiv \mathrm{Ti(IV)}]\sqrt{\frac{1}{k_4 k_5}}$ and $K = K_3$ at a fixed intermediate light intensity (i.e., the second term in the denominator of eq 18 dominates).

5. ***Chlorate and oxygen.*** To understand the effects when both ClO_3^- and O_2 are present, we consider $\frac{\partial \Phi}{\partial [ClO_3^-]}$ of eq 14 at high $[O_2]$, low [4-CP], and high light intensity:

$$\frac{\partial \Phi}{\partial [ClO_3^-]} = \frac{k_1 K_2 K_3 [\equiv \mathrm{Ti(IV)}]^2 [4CP]\left(-k_2 K_2 [ClO_3^-] + (k_2 - 2k_3) K_1 [O_2]\right)}{k_5 k_{-1} \left(K_1[O_2] + K_2[ClO_3^-]\right)^3} \tag{19}$$

The sign of eq 19 is thus determined by the following expression:

$$-k_2 K_2 [ClO_3^-] + (k_2 - 2k_3) K_1 [O_2] \tag{20}$$

This expression is negative since $k_3 > k_2$ (eq T5.9). Hence, an increase in $[ClO_3^-]$ yields a decrease in Φ. The behavior is shown in Figure 1a for low [4-CP], high $[O_2]$, and high light intensity.

The result embodied in eq 20 may seem initially counterintuitive. Figure 4 shows parallel pathways (eqs T2.3-4) so that increases in $[ClO_3^-]$ and $[O_2]$ would be expected to both yield enhanced degradation rates. However, the surface of TiO_2 is saturated with respect to O_2 under our experimental conditions. As a result, ClO_3^- displaces O_2. The loss of O_2, which has a higher reactivity than ClO_3^-, decreases Φ.

Iodide Oxidation. In order to test our proposed mechanism, several experiments were carried out with I^- as the primary electron donor. The oxidation pathway of I^- does not provide a reaction pathway with ClO_3^- (*vide infra*). Hence, the equivalent of eq T2.3 has a reaction rate constant $k_2 = 0$. The validity of the proposed mechanism is thus tested by the effect of $[ClO_3^-]$ on the oxidation rate of I^-, as discussed below.

The overall oxidation of I^- is a two-electron process as follows[22,29,45-47]:

$$2\,I^- \leftrightarrow I_2 + 2\,e^- \qquad E^\circ = -\,0.620\text{ V} \tag{21}$$

However, under normal experimental conditions, I_2 is rapidly complexed by I^- to form I_3^-:

$$I^- + I_2 \leftrightarrow I_3^- \qquad K = 770\text{ M}^{-1},\ k_f = 5.6 \times 10^9\text{ M}^{-1}\text{ s}^{-1} \tag{22}$$

A likely reaction pathway initiated by valence-band hole oxidation is as follows:

$$I^- \leftrightarrow I\cdot + e^- \qquad E^\circ = -\,1.3\text{ V} \tag{23}$$

$$I\cdot + I^- \rightarrow I_2^-\cdot \qquad K = 1.1 \times 10^5\text{ M}^{-1},\ k = 1 \times 10^{10}\text{ M}^{-1}\text{ s}^{-1} \tag{24}$$

$$I_2^-\cdot \leftrightarrow I_2 + e^- \qquad E^\circ = -\,0.2\text{ V} \tag{25}$$

Pathways due to oxidation by a surficial hydroxyl radical are also possible:

$$I^- + \cdot OH_s \rightarrow I\cdot + OH_s^- \qquad k = 1.2 \times 10^{10}\ M^{-1}\ s^{-1} \tag{26}$$

$$\cdot OH_s + I_2 \rightarrow HOI + I\cdot \qquad k = 1.1 \times 10^{10}\ M^{-1}\ s^{-1} \tag{27}$$

$$I\cdot + I^- \rightarrow I_2^-\cdot \qquad K = 1.1 \times 10^5\ M^{-1},\ k = 1 \times 10^{10}\ M^{-1}\ s^{-1} \tag{28}$$

The important iodine radicals believed to be present in the $KI/TiO_2/h\nu$ system are thus $I\cdot$ and $I_2^-\cdot$. Although $I\cdot$ is a potential oxidant (eq 23), its reaction with ClO_3^- is thermodynamically unfavorable ($E°(ClO_3/ClO_3^-) \approx 2.1$ V).[31] The reduction of ClO_3^- by $I_2^-\cdot$ is considered to be of minor importance due to electrostatic repulsion of the reactants. Hence, in a heterogeneous $KI/TiO_2/h\nu/ClO_3^-$ system, no indirect oxidation pathway similar to the ClO_3^- pathway for 4-CP (Figure 4 and eq T2.3) is available.

Iodide - Kinetic Equations. The oxidation of I^- is described by equations similar to those in Table 2 with the following changes: $[\equiv I^-]$ is substituted for $[\equiv$4-CP$]$, $[\equiv I\cdot]$ for $[\equiv$4-CD$]$, and $k_2 = k_3 = 0$. Employing eq 10, we write the quantum efficiency for the oxidation of iodide, Φ', as follows:

$$\Phi' = -(1/k_5)\left(d[I^-]/dt\right) = +\,k_1\sqrt{1/k_5k_4}\,[\equiv I^-] - k_{-1}\sqrt{1/k_5k_4}\,[\equiv I\cdot] \tag{29}$$

We assume the time-constant for steady-state concentrations of $I\cdot$ and I_3^- is 10 min based upon the negative feedback with respect to I^- oxidation (Figure 3). An expression for the initial quantum efficiency for the oxidation (i.e., $t < 10$

min) of I^- is obtained by substituting $[\equiv I\cdot] = 0$, Γ_1, Γ_2, and Γ_3 into eq 29 as follows:

$$\Phi' = k_1\sqrt{\frac{1}{k_5 k_4}}\left(\frac{K_3[\equiv \mathrm{Ti(IV)}][I^-]}{1+K_1[O_2]+K_2[ClO_3^-]+K_3[I^-]}\right) \tag{30}$$

The initial quantum efficiency, Φ_i, for the formation of I_3^- (i.e., the oxidation product of I^-) is thus written as follows:

$$\Phi_i = \Phi' \tag{31}$$

The value of $KC(I^-)$ is 0.32 for $C = 1$ mM and $K = 3.2 \times 10^2$ M^{-1}.[18] We would thus predict that Φ_i should decrease 10-fold upon the addition of either 1 mM O_2 or 0.1 M ClO_3^- because $KC(O_2) \approx 10$ and $KC(ClO_3^-) \approx 1$ are greater than $KC(I^- \approx 0.3)$. In fact, Φ_i varies from $(4.3\text{-}7.6) \times 10^{-4}$ (Figure 3). The competitive adsorption site model given by eq 31 thus does not describe heterogeneous oxidation of iodide.

When I^- binds noncompetitively to the surface of TiO_2 (i.e., a two-site model for I^-, on the one hand, and O_2 and ClO_3^-, on the other hand), the oxidation of I^- is described by the following equation:[18]

$$\Phi_i = k_1\sqrt{\frac{1}{k_4 k_5}}\left(\frac{K_3[\equiv \mathrm{Ti(IV)}_A][I^-]}{1+K_3[I^-]}\right) \tag{32}$$

based upon eq 31 for $K_1 = K_2 = 0$. In this case, I^- adsorbs to $\equiv\mathrm{Ti(IV)}_A$ whereas O_2 and ClO_3^- adsorb to $\equiv\mathrm{Ti(IV)}_B$. The addition of ClO_3^- thus does not affect the oxidation of I^-. In oxygenated solutions, conduction-band electrons are scavenged by O_2, which reduces charge-pair recombination. This effect may be included in eq 32 by reducing k_4 and thus increasing Φ_i. Finally, the addition of ClO_3^- to an oxygenated solution reduces $[\equiv O_2]$ via competitive adsorption for $\equiv Ti(IV)_B$, increases k_4, and thus decreases Φ_i. These predictions are confirmed by the results shown in Figure 3.

Under steady-state conditions (i.e., $t > 10$ min), $[\equiv I\cdot]$ can be written as follows (cf. eq 13):

$$[\equiv I\cdot] = \left(\frac{k_1[\equiv h^+][\equiv I^-]}{k_{-1}[\equiv e^-]}\right) \tag{33}$$

Substitution of eq 10 into eq 33 and the resulting expression into eq 29 yields an expression for the steady-state oxidation of I^- as follows: $\frac{d[I^-]}{dt} = 0$. The I^-/I_3^- couple thus serves to introduce an additional charge-pair recombination pathway. However, although Φ_{ss} is less than Φ_i, Φ_{ss} is not zero (Figure 3). The cumulative oxidation of I^- may be explained by the concurrent irreversible oxidation of H_2O to produce $\cdot OH$, which subsequently oxidizes I^-.

The purpose of the experiments with I^- was to test the validity of the mechanism proposed in Figure 4 and Table 2. Indeed, the kinetic behavior (eqs 32 and 33) of the oxidation of I^- in the presence of ClO_3^- is consistent with the proposed role of ClO_3^- in the oxidation of 4-CP (Figure 3).

Conclusions

Normal approaches to enhanced photo-efficiencies of the TiO_2/UV process include reduction of the rate of charge-carrier recombination and enhancement of the rate of the primary interfacial charge transfer.[1,12-14] In line with this approach, our results suggest that BrO_3^- scavenges conduction-band electrons, reduces charge-carrier recombination, and increases photoreactivity. At similar concentrations, BrO_3^- scavenges e^-_{cb} more efficiently than O_2. The reduced brominated products (e.g., BrO_2) may directly oxidize 4-CP and its products and may further scavenge e^-_{cb}. In this case, one photon yields several oxidative steps.

In contrast to BrO_3^-, ClO_3^- does not scavenge conduction-band electrons. Competitive adsorption occurs among 4-CP, ClO_3^-, and O_2 for surficial Ti(IV) sites, and the degradation of 4-CP follows three concurrent pathways. The proposed mechanism is shown in Figure 4 and Table 2, and the general kinetic equation is given in eq 14. The equation conforms to the dependency of rate of degradation of 4-CP on the concentrations of 4-CP, ClO_3^-, and O_2 and on the light intensity. The kinetics of the oxidation of I^- verify the proposed role of ClO_3^- as an oxidant of 4-CD.

In addition to scavenging e^-_{cb}, the oxyanions BrO_3^-, IO_4^-, and ClO_2^- may select reaction pathways via thermal oxidation. Higher quantum efficiencies should result when these oxyanions direct oxidation along efficient pathways for which multiple thermal oxidative events occur subsequent to photoinitiation. The obvious implication for heterogeneous photochemistry is that pathway-specific electron acceptors may provide effective routes to obtain higher quantum efficiencies. Furthermore, we note that macroscopic measurements of quantum efficiencies based upon product yields alone may not be representative of the branching ratio between charge-carrier recombination and interfacial charge transfer due to thermal oxidation steps.

Acknowledgment. We are grateful to ARPA and ONR {NAV 5 HFMN N0001492J1901} for financial support. Drs. Ira Skurnick and Harold Gund provided generous support and encouragement. S. Martin is supported by a

National Defense Science and Engineering Graduate Fellowship. A. Lee is the recipient of a Summer Undergraduate Research Fellowship from Caltech. Wonyong Choi, Peter Green, Nicole Peill, and Janet Kesselman provided valuable support and stimulating discussion.

References

(1) Hoffmann, M. R.; Martin, S. T.; Choi, W.; Bahnemann, D. W. *Chem. Rev.* **1995**, *95*, 69.

(2) Pelizzetti, E.; Carlin, V.; Minero, C.; Grätzel, M. *New J. Chem.* **1991**, *15*, 351.

(3) Abdullah, M.; Low, G. K. C.; Matthews, R. W. *J. Phys. Chem.* **1990**, *94*, 6820.

(4) Grätzel, C. K.; Jirousek, M.; Grätzel, M. *J. Mol. Catal.* **1990**, *60*, 375.

(5) Al-Ekabi, H.; Butters, B.; Delany, D.; Ireland, J.; Lewis, N.; Powell, T.; Story, J. In *Photocatalytic Purification and Treatment of Water and Air:*, D. F. Ollis and H. Al-Ekabi, Ed.; Elsevier: Amsterdam, 1993, p. 321.

(6) Vinodgopal, K.; Stafford, U.; Gray, K. A.; Kamat, P. V. *J. Phys. Chem.* **1994**, *98*, 6797.

(7) Stafford, U.; Gray, K.; Kamat, P.; Varma, A. *Chem. Phys. Lett.* **1993**, *205*, 55.

(8) Hofstadler, K.; Bauer, R.; Novalic, S.; Heisler, G. *Environ. Sci. Technol.* **1994**, *28*, 670.

(9) Mills, A.; Morris, S. *J. Photochem. Photobiol. A: Chem* **1993**, *71*, 285.

(10) Mills, A.; Morris, S.; Davies, R. *J. Photochem. Photobiol. A: Chem.* **1993**, *70*, 183.

(11) Mills, A.; Morris, S. *J. Photochem. Photobiol. A: Chem* **1993**, *71*, 75.

(12) Martin, S. T.; Herrmann, H.; Choi, W.; Hoffmann, M. R. *J. Chem. Soc. Faraday Trans.* **1994**, *90*, 3315.

(13) Martin, S. T.; Herrmann, H.; Hoffmann, M. R. *J. Chem. Soc. Faraday Trans.* **1994**, *90*, 3323.

(14) Martin, S. T.; Morrison, C. L.; Hoffmann, M. R. *J. Phys. Chem.* **1994**, *98*, 13695.

(15) Kormann, C.; Bahnemann, D. W.; Hoffmann, M. R. *J.Phys.Chem.* **1988**, *92*, 5196.

(16) Lepore, G.; Langford, C. H.; Víchová, J.; Vlcek, A. *J. Photochem. Photobiol. A.: Chem.* **1993**, *75*, 67.

(17) Fitzmaurice, D. J.; Frei, H. *Langmuir* **1991**, *7*, 1129.

(18) Herrmann, J.; Pichat, P. *J. Chem. Soc. Faraday I* **1980**, *76*, 1138.

(19) Draper, R. B.; Fox, M. A. *Langmuir* **1990**, *6*, 1396.

(20) Suatoni, J. C.; Snyder, R. E.; Clark, R. O. *Analytical Chemistry* **1961**, *33*, 1894.

(21) Standbury, D. M. *Adv. Inorg. Chem.* **1989**, *33*, 69.

(22) Wardman, P. *J. Phys. Chem. Ref. Data* **1989**, *18*, 1637.

(23) Bard, A. J. *Science* **1980**, *207*, 139.

(24) Grätzel, M. *Acc. Chem. Res.* **1981**, *14*, 376.

(25) Nozik, A. J. *Nature* **1975**, *257*, 383.

(26) Fujishima, A.; Honda, K. *Bull. Chem. Soc. Jpn.* **1971**, *44*, 1148.

(27) Fujishima, A.; Honda, K. *Nature* **1972**, *238*, 37.

(28) Sawyer, D. T. *Oxygen Chemistry*; Oxford University Press: New York, 1991.

(29) Buxton, G. V.; Greenstock, C. L.; Helman, W. P.; Ross, A. B. *J. Phys. Chem. Ref.* **1988**, *17*, 513.

(30) Bielski, B. H. J.; Cabelli, D. E.; Arudi, R. L.; Ross, A. B. *J. Phys. Chem. Ref.* **1985**, *14*, 1041.

(31) Domae, M.; Katsumara, Y.; Jiang, P. Y.; Nagaishi, R.; Hasegawa, C.; Ishigure, K.; Yoshida, Y. *J. Phys. Chem.* **1994**, *98*, 190.

(32) Serpone, N.; Lawless, D.; Terzian, R.; Meisel, D. In *Electrochemistry in Colloids and Dispersions:*, R. A. Mackay and J. Texter, Ed.; VCH Publishers, Inc.: New York, 1992, p. 399-416.

(33) D'Oliveira, J. C.; Al-Sayyed, G.; Pichat, P. *Environ. Sci. Technol.* **1990**, *24*, 990.

(34) Al-Ekabi, H.; Serpone, N.; Pelizzetti, E.; Minero, C. *Langmuir* **1989**, *5*, 250.

(35) Minero, C.; Aliberti, C.; Pelizzetti, E.; Terzian, R.; Serpone, N. *Langmuir* **1991**, *7*, 928.

(36) Laidler, K. J. *Chemical Kinetics*; 3rd; HarperCollins: New York, 1987.

(37) March, J. *Advanced Organic Chemistry*; 4th; John Wiley & Sons: New York, 1992.

(38) Wachs, I. E.; Saleh, R. Y.; Chan, S. S.; Cherisch, C. C. *Applied Catalysis* **1985**, *15*, 339.

(39) White, M. G. *Heterogeneous Catalysis*; Prentice-Hall Inc.: Englewood Cliffs, 1990.

(40) Turchi, C. S.; Ollis, D. F. *J. Catalysis* **1990**, *122*, 178.

(41) Stumm, W. *Chemistry of the Solid-Water Interface*; John Wiley & Sons, Inc.: New York, 1992.

(42) Cunningham, J.; Al-Sayyed, G. *J. Chem. Soc. Faraday Trans.* **1990**, *86*, 3935.

(43) Kormann, C.; Bahnemann, D. W.; Hoffmann, M. R. *Environ. Sci. Technol.* **1991**, *25*, 494.

(44) Hoffman, A. J.; Carraway, E. R.; Hoffmann, M. R. *Environ. Sci. Technol.* **1994**, *28*, 776.

(45) Kotronarou, A. Chemical Effects of Ultrasound in Water, California Institute of Technology, 1991

(46) Neta, P.; Huie, R. E.; Ross, A. B. *J. Phys. Chem. Ref. Data* **1988**, *17*, 1027.

(47) Elliot, A. J. *Can. J. Chem.* **1992**, *70*, 1658.

	Quantum Efficiency	
Oxyanion Oxidant	without TiO_2	with TiO_2
ClO_3^-	0.0	0.03
BrO_3^-	0.03	4.6
IO_4^-	0.9	4.8
ClO_2^-	2.2	4.8
O_2	0.0	0.3

Table 1: Apparent quantum efficiencies ($\Phi \times 10^2$) for the photooxidation of 4-CP by the TiO_2/UV process in the presence of several oxidants (0.1 M $NaClO_3$, 0.1 M $KBrO_3$, 18 mM KIO_4, 0.1 M $NaClO_2$, and 1 atm O_2). Conditions: $I = 2.1$ mEin min^{-1}, $\lambda > 340$ nm, deoxygenated, $[TiO_2] = 1$ g/L, pH unadjusted, T = 25 °C, $[4\text{-CP}]_0 = 100\ \mu M$.

Chemical Reactions

k_1	$\equiv\text{4-CP} + \equiv h^+ \rightarrow \equiv\text{4-CD}$	(T2.1)
k_{-1}:	$\equiv\text{4-CD} + \equiv e^- \rightarrow \equiv\text{4-CP}$	(T2.2)
k_2:	$\equiv\text{4-CD} + \equiv ClO_3^- \rightarrow \text{4-CD}^+$	(T2.3)
k_3:	$\equiv\text{4-CD} + \equiv O_2 \rightarrow \rightarrow \text{pdts}$	(T2.4)
k_4:	$\equiv e^- + \equiv h^+ \rightarrow TiO_2$	(T2.5)
k_5:	$TiO_2 + h\nu \rightarrow e^- + h^+$	(T2.6)
k_6:	$e^- \rightarrow \equiv e^-$	(T2.7)
k_7:	$h^+ \rightarrow \equiv h^+$	(T2.8)
k_8:	$\equiv e^- + \equiv O_2 \rightarrow \equiv O_2^-$	(T2.9)

Surface Adsorption

$$K_1 = \frac{[\equiv O_2]}{[O_2][\equiv \text{Ti(IV)}]} \tag{T2.10}$$

$$K_2 = \frac{[\equiv ClO_3^-]}{[ClO_3^-][\equiv \text{Ti(IV)}]} \tag{T2.11}$$

$$K_3 = \frac{[\equiv 4CP]}{[4CP][\equiv \text{Ti(IV)}]} \tag{T2.12}$$

Surface Coverage

$$\Gamma_1{:}[\equiv O_2] = \frac{K_1[O_2][\equiv \text{Ti(IV)}]_0}{1 + K_1[O_2] + K_2[ClO_3^-] + K_3[4CP]} \tag{T2.13}$$

$$\Gamma_2{:}[\equiv ClO_3^-] = \frac{K_2[ClO_3^-][\equiv \text{Ti(IV)}]_0}{1 + K_1[O_2] + K_2[ClO_3^-] + K_3[4CP]} \tag{T2.14}$$

$$\Gamma_3{:}[\equiv\text{4-CP}] = \frac{K_3[4CP][\equiv \text{Ti(IV)}]_0}{1 + K_1[O_2] + K_2[ClO_3^-] + K_3[4CP]} \tag{T2.15}$$

Table 2: Chemical reactions and kinetic equations of the proposed mechanism for the TiO_2/UV photooxidation of 4-CP in the presence of O_2 and ClO_3^-.

Kinetic Equations

$$\frac{d[4CP]}{dt} = -k_1[{\equiv}h^+][{\equiv}4\text{-}CP] + k_{-1}[{\equiv}e^-][{\equiv}4\text{-}CD] \qquad (T2.16)$$

$$\frac{d[4CD]}{dt} = +k_1[{\equiv}h^+][{\equiv}4\text{-}CP] - k_{-1}[{\equiv}e^-][{\equiv}4\text{-}CD]$$

$$- k_2[{\equiv}4\text{-}CD][{\equiv}ClO_3^-] - k_3[{\equiv}4\text{-}CD][{\equiv}O_2] \qquad (T2.17)$$

$$\frac{d[{\equiv}e^-]}{dt} = k_6[e^-] - k_4[{\equiv}e^-][{\equiv}h^+] - k_8[{\equiv}e^-][{\equiv}O_2] - k_{-1}[{\equiv}e^-][{\equiv}4\text{-}CD] \qquad (T2.18)$$

$$\frac{d[{\equiv}h^+]}{dt} = k_7[h^+] - k_4[{\equiv}e^-][{\equiv}h^+] - k_1[{\equiv}h^+][{\equiv}4\text{-}CP] \qquad (T2.19)$$

$$\frac{d[e^-]}{dt} = k_5 - k_6[e^-] \qquad (T2.20)$$

$$\frac{d[h^+]}{dt} = k_5 - k_7[h^+] \qquad (T2.21)$$

Steady-State Approximation

$$\frac{d[4CD]}{dt} = \frac{d[{\equiv}e^-]}{dt} = \frac{d[{\equiv}h^+]}{dt} = \frac{d[e^-]}{dt} = \frac{d[h^+]}{dt} = 0 \qquad (T2.22)$$

Charge-Neutrality

$$[{\equiv}e^-] + [e^-] - [{\equiv}h^+] - [h^+] = 0 \qquad (T2.23)$$

Relative Reaction Rates

$$k_3 > k_2 \qquad (T2.24)$$

Table 2 (continued): Chemical reactions and kinetic equations of the proposed mechanism for the TiO_2/UV photooxidation of 4-CP in the presence of O_2 and ClO_3^-.

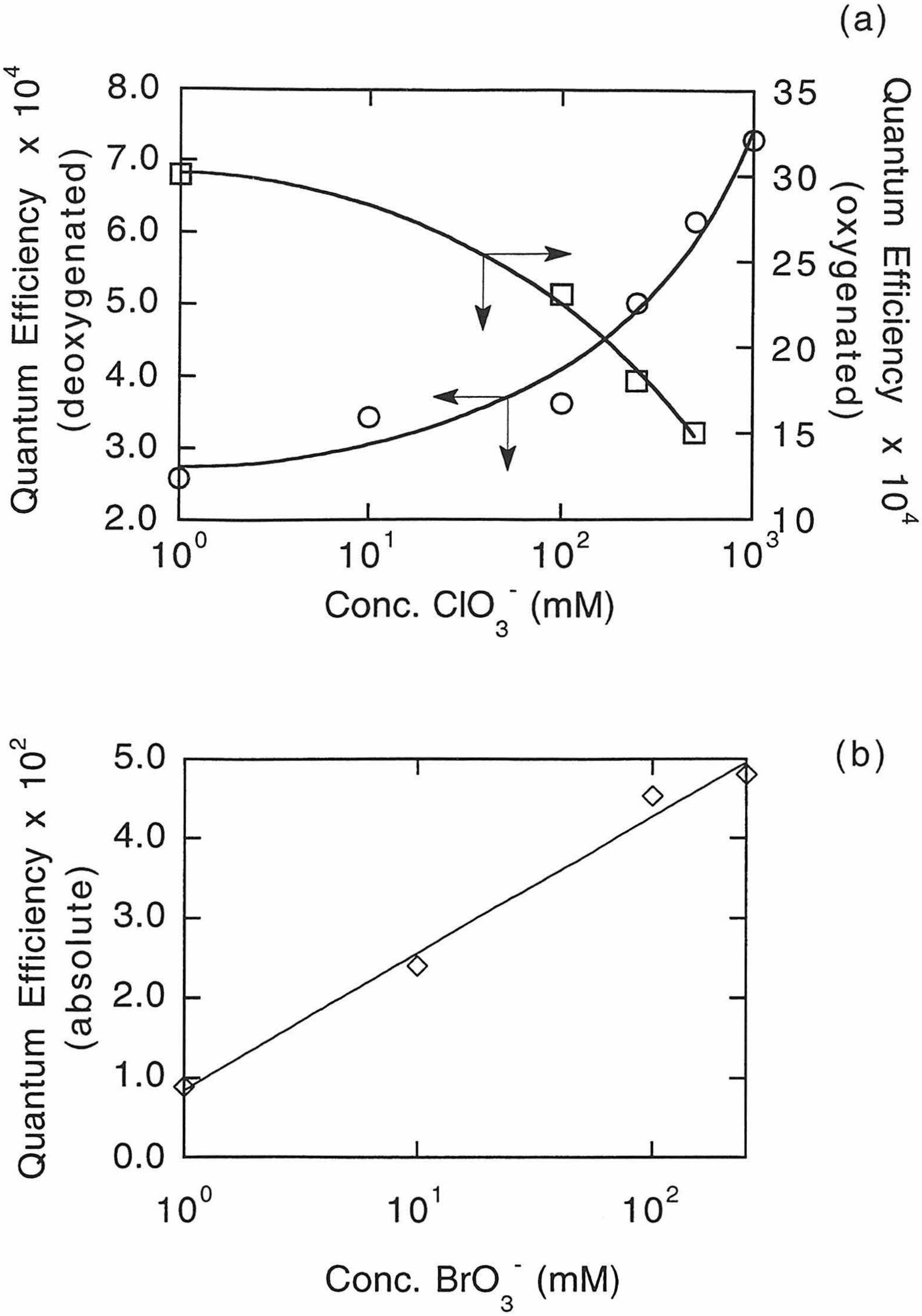

Figure 1: (a) Initial quantum efficiencies for the photooxidation of 4-CP in deoxygenated (O) and oxygenated (□) TiO_2 slurries as a function of Log[ClO_3^-]. (b) Initial quantum efficiencies for the photooxidation of 4-CP (◇) as a function of Log[BrO_3^-]. O_2 has no apparent effect. Conditions: See Table 1.

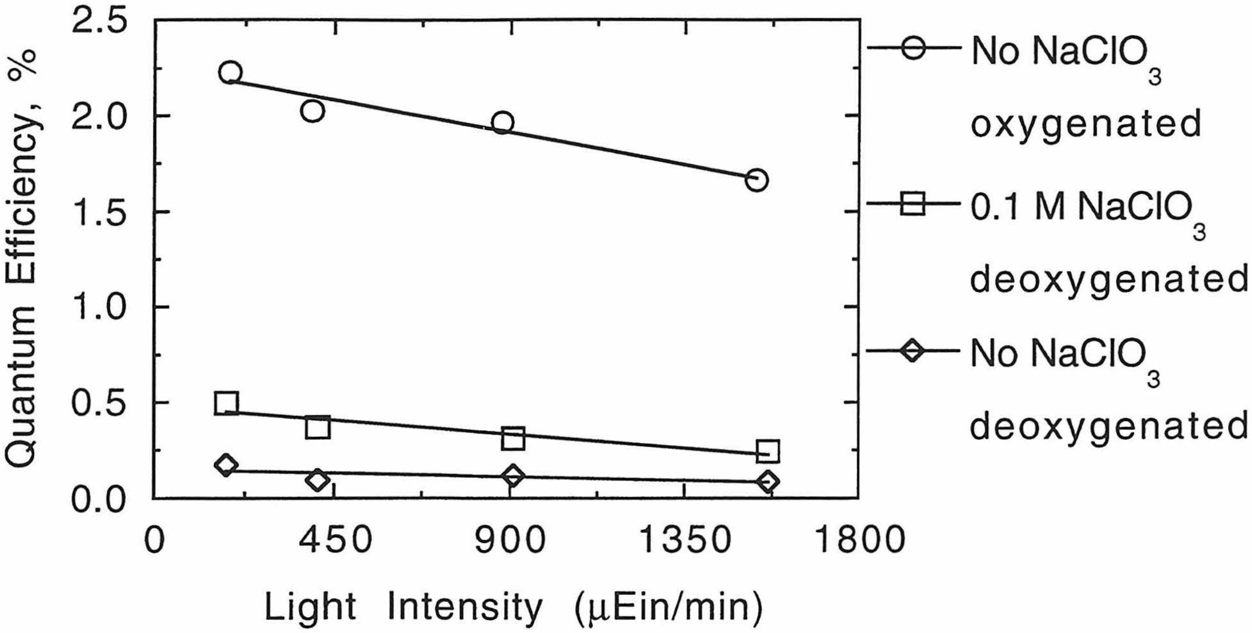

Figure 2: Quantum efficiency for the disappearance of 4-CP in a slurry of $NaClO_3$, O_2, and TiO_2 as a function of incident light intensity. Conditions: See Table 1.

	△	□	○	◇	×
Quantum efficiency	No $NaClO_3$ oxygenated	$NaClO_3$ oxygenated	No $NaClO_3$ deoxygenated	$NaClO_3$ deoxygenated	$NaClO_3$ wo/P25 deoxygenated
$\Phi_i \times 10^4$	7.6	6.3	4.3	4.3	0.0
$\Phi_{ss} \times 10^5$	1.6	1.1	1.1	0.7	0.0

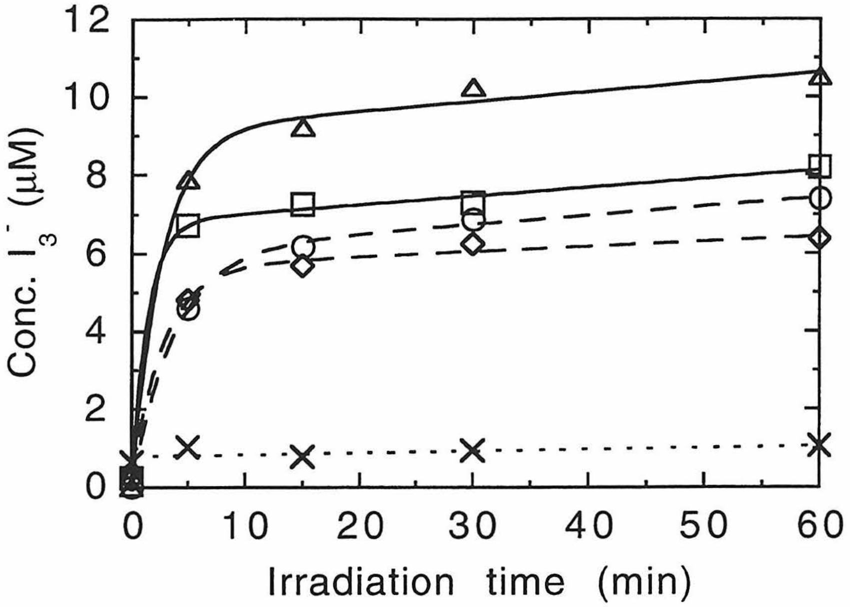

Figure 3: Formation of I_3^- in suspensions of 1 mM I^-, 0.1 M ClO_3^-, O_2, and TiO_2 irradiated with ultraviolet light. Initial (i) and steady-state (ss) quantum-efficiencies are shown in the legend. Conditions: See Table 1.

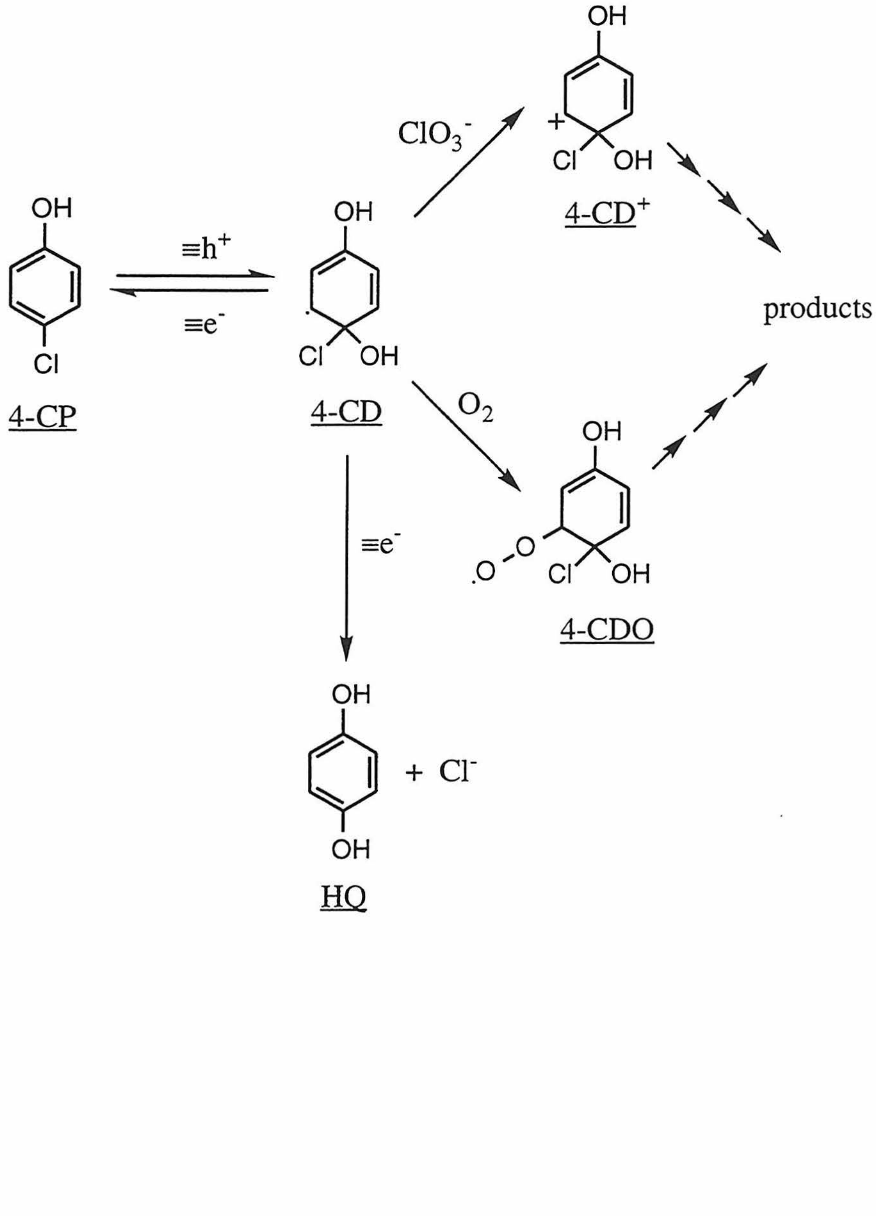

Figure 4: Reaction mechanism.

Chapter 7

Conclusions

The composite of the work of this thesis and of earlier work in Professor Hoffmann's laboratory[1-4] yields a current understanding of quantum efficiency. Following charge-pair generation, charge-carriers migrate to the surface of the TiO_2 particle. In transit to the surface, the charge-carriers may be trapped or may recombine, especially if transition-metal dopants are present.[5,6] At the surface, charge-carriers may undergo direct transfer to adsorbed substrates or they may be trapped, especially holes as surface hydroxyl radicals.[7,8] Once trapped, charge-carriers may recombine or initiate surface chemistry. At this point, the charge-carriers are removed from the particle. The processes are shown schematically in Figure 1.

The electronic processes following charge-pair formation through the primary chemical event occurring at the surface have been described. Similarly, the chemical substrates must transit from the bulk of the solution to the surface of the particle. The structure of the double-layer affects the approach of the substrates, especially if they are charged.[9] Once in the proximity of the surface, substrates are available for direct outer-sphere electron transfer. Alternatively, some substrates specifically adsorb to the surface by undergoing ligand exchange with hydroxide groups.[6,10,11] In this case, inner-sphere electron transfer is available and, in addition, new surface-states are introduced that can influence charge-carrier dynamics.[7] Finally, the primary chemical species may undergo secondary reactions.[11] Figure 2 shows the array of possible secondary reactions possible following the reduction of dioxgyen by a conduction-band electron.

In my view, the following research directions would prove particularly fruitful in furthering our understanding of the TiO_2/UV process. Although the TRMC work established the connection between charge-carrier dynamics and photoreactivity, the characterization, structure, and synthetic history of the investigated catalysts are not known. The next step is thus to establish the relationship between synthesis and charge-carrier dynamics. Connecting the steps, one would obtain predictions of photoreactivity based upon synthetic approaches. The TRMC technique should also be valuable in an industrial laboratory employing combinatorial synthesis of catalysts because it provides an efficient screening tool as a substitute for labor intensive photoreactivity experiments.

The RF work should be optimized to permit *in situ* measurements of the TiO_2/UV process. The sensitivity of the RF instrument is directly proportional to the charge-carrier mobility, and thus TRRFC experiment works well for the high mobility carriers in ZnO. The charge-carrier mobility is reduced by a factor of 10^3 when making measurements of TiO_2. A more sensitive RF instrument using a lock-in amplifier would permit the study of steady-state charge-carrier concentrations *simultaneously* with steady-state photoreactivity.[12] This apparatus would open new possibilities for basic experimental research because photoreactivity and photophysics experiments have historically been conducted under different experimental conditions (*vide supra*).

The work on oxidants (chapter 6) demonstrates 10-fold increases in quantum efficiencies. The oxidants could easily be included in existing pilot-scale TiO_2/UV treatment facilities. However, the oxidants studied in chapter six are both expensive and toxic. The success with these oxidants, nevertheless, suggests research should be initiated for less costly, nontoxic oxidizing agents. In addition to the evident motivation towards applied science, chapter 6 demonstrates the interesting and novel surface formations, catalytic cycles, and pathway selection of oxidants in the TiO_2/UV process, and further research on oxidants should be of interest to basic science.

I shall finish this thesis by providing perspective on its place in the history of research done on the TiO_2/UV process. In 1976, Carey et al.[13] reported the dechlorination of PCB's in dispersions of TiO_2 irradiated with UV light in the context of a sink in the natural environment for PCB's. The conceptual understanding of the process was as follows: "Absorption of light by metallic oxides can induce reaction at the oxide surface with molecules in solution or gas phase." In 1983, Pruden and Ollis[14] introduced the TiO_2/UV process for water treatment. In the intervening 12 years, the TiO_2/UV process has emerged as a particularly promising AOP because TiO_2 is a renewable catalyst; the underlying technologies of TiO_2 production and UV light output are well developed; diverse reaction conditions are possible (pH 1-14, broad pollutant concentrations, temperature, universal application to oxidizables and reducibles, and metals); and complete mineralization to CO_2 is achieved. Commercial TiO_2/UV systems are now available.[15] The general march forward, however, has been made in the absence of a clear understanding of the underlying electronic and chemical processes. I believe that the current research on the TiO_2/UV process is presently at the doorstep of the formation of a conceptual model at a fundamental level. It is my hope that this thesis will rest as an enduring step in our upward climb towards that understanding. Truly, then, I would expect the conceptual model to yield in the near future significant improvements in the efficacy of the TiO_2/UV process.

References

(1) Hoffmann, M. R.; Martin, S. T.; Choi, W.; Bahnemann, D. W. *Chem. Rev.* **1995**, *95*, 69.

(2) Hoffman, A. J. Thesis, California Institute of Technology, 1993.

(3) Pehkonen, S. O. Thesis, California Institute of Technology, 1995.

(4) Kormann, C. Thesis, California Institute of Technology, 1989.

(5) Choi, W.; Termin, A.; Hoffmann, M. R. *J. Phys. Chem.* **1994**, *98*, 13669.

(6) Martin, S. T., Thesis, Chapter Five.

(7) Martin, S. T., Thesis, Chapter Two.

(8) Martin, S. T., Thesis, Chapter Three.

(9) Kormann, C.; Bahnemann, D. W.; Hoffmann, M. R. *Environ. Sci. Technol.* **1991**, *25*, 494.

(10) Martin, S. T.; Kesselman, J. M.; Park, D.; Hoffmann, M. R. *Environ. Sci. Technol.* **1995** submitted.

(11) Martin, S. T., Thesis, Chapter Six.

(12) Martin, S. T. Thesis, Ph.D. Thesis Propositions, California Institute of Technology, 1995.

(13) Carey, J. H.; Lawrence, J.; Tosine, H. M. *Bull. Environ. Contam. Toxic.* **1976**, *16*, 697.

(14) Pruden, A. L.; Ollis, D. F. *J. Catalysis* **1983**, *82*, 404.

(15) Matrix, London, Ontario.

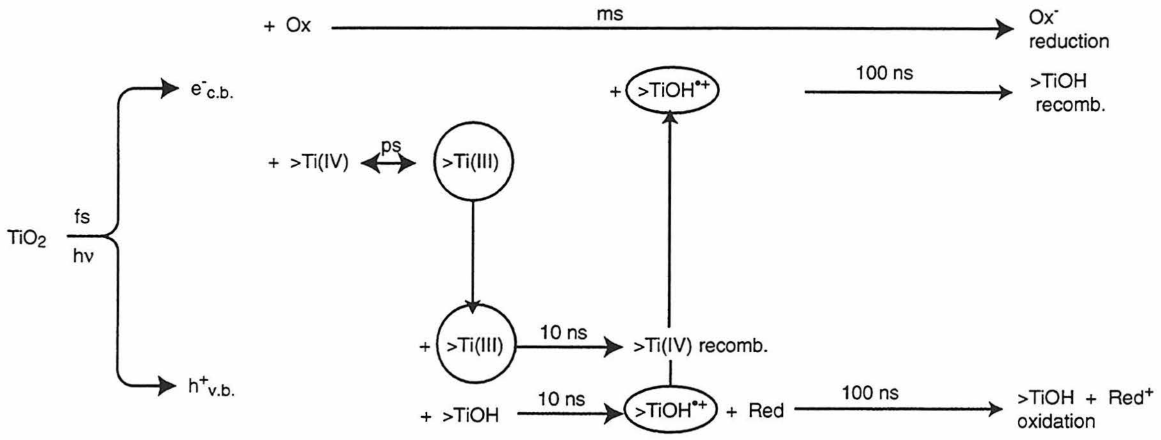

Figure 1: Kinetics of the primary steps in photoelectrochemical mechanism. Recombination is mediated primarily by >Ti(III) in the first 10 ns. Valence-band holes are sequestered as long-lived $>\mathrm{TiOH}^{\bullet+}$ after 10 ns. >TiOH is reformed by recombination with conduction-band electrons or oxidation of the substrate on the time-scale of 100 ns. The arrow lengths are representative of the respective time scales.

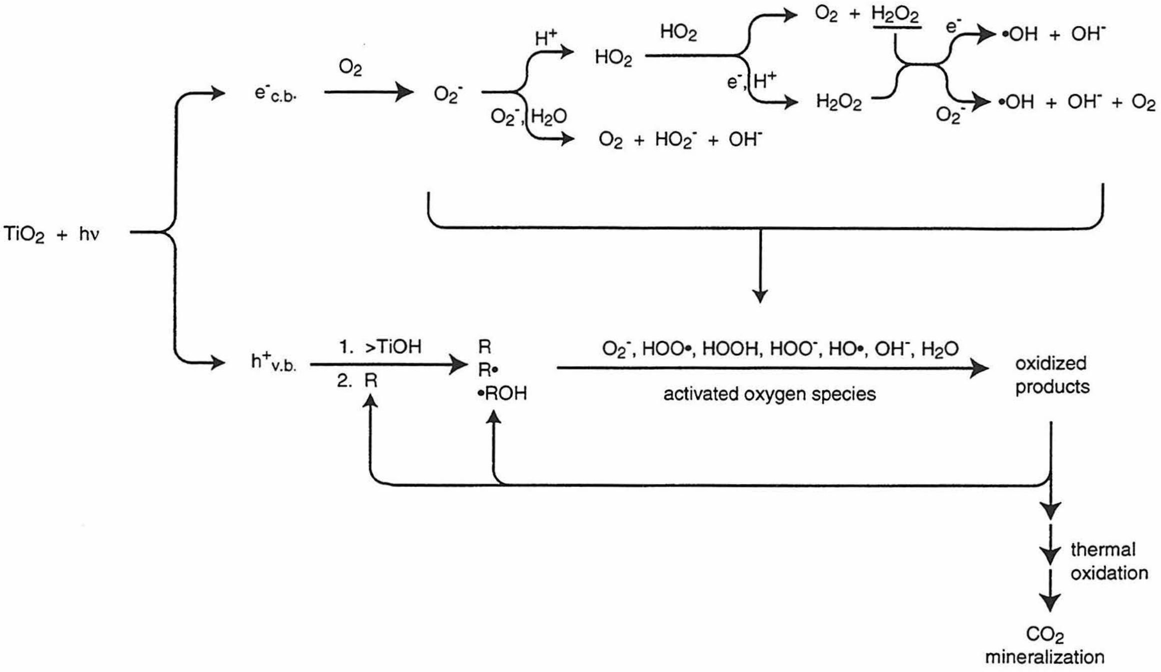

Figure 2: Secondary reactions with activated oxygen species in the photoelectrochemical mechanism.